ELECTRONIC STRUCTURE AND FERMI SURFACE PROPERTIES OF Nb_3Sn AND Nb_3Sb

A. T. van Kessel

ELECTRONIC STRUCTURE AND FERMI SURFACE PROPERTIES OF Nb_3Sn AND Nb_3Sb

PROMOTOR:
PROF. DR. F. M. MUELLER

CO-REFERENT:
DR. H. W. MYRON

ELECTRONIC STRUCTURE AND FERMI SURFACE PROPERTIES OF Nb_3Sn AND Nb_3Sb

PROEFSCHRIFT

TER VERKRIJGING VAN DE GRAAD VAN DOCTOR IN DE
WISKUNDE EN NATUURWETENSCHAPPEN
AAN DE KATHOLIEKE UNIVERSITEIT TE NIJMEGEN,
OP GEZAG VAN DE RECTOR MAGNIFICUS,
PROF DR P G A B WIJDEVELD,
VOLGENS BESLUIT VAN HET COLLEGE VAN DECANEN
IN HET OPENBAAR TE VERDEDIGEN
OP DONDERDAG 9 APRIL 1981
DES NAMIDDAGS TE 2 UUR PRECIES

door

Augustinus Thomas van Kessel

geboren te Amsterdam

krips repro meppel
1981

Dit werk is een gedeelte van het onderzoekprogramma van de Stichting voor Fundamenteel Onderzoek der Materie (FOM), welke financieel gesteund wordt door de Nederlandse Organisatie voor Zuiver Wetenschappelijk Onderzoek (ZWO).

Vele medewerkers van de Fakulteit der Wiskunde en Natuurwetenschappen hebben een bijdrage geleverd aan de totstandkoming van dit proefschrift.

In het bijzonder ben ik erkentelijk:
Typewerk : Maria van Leeuwen,
Taal-correcties : Harold Myron en Fred Mueller,
Tekeningen : afdeling Illustratie en Fotografie.

Ter herinnering aan mijn moeder
aan Marthos, Kim, René en Kevin

CONTENTS

Note: The references can be found at the end of each numbered (sub-) chapter.

CHAPTER I : THE CLASS OF A-15 COMPOUNDS

The two materials studied in this thesis belong to the class known as the β-tungsten or A-15 compounds. This crystal structure is so named because, at its discovery[1], it was thought, one had synthesized a second phase of crystalline tungsten. Since it was the 15th monotype crystal structure, denoted as A, A-15 is also used. The continuing interest in A-15 compounds (A_3B) is mainly due to the fact that several of them are high temperature superconductors. For example V_3Si (T_c=17.1°K), V_3Ga (16.8°K), Nb_3Sn (18°K), Nb_3Al (18.5°K) and Nb_3Ge (23°K) all are among the highest T_c superconductors now known after more than 70 years of research. Nb_3Sn is actually used in the construction of superconducting magnets for fields in excess of 10 Tesla, despite the difficulties involved in fabricating long continuous wires of this brittle material. Unfortunately many of the high temperature superconductors are unstable which is manifested by both their anomalous elastic constants and multitude of structural transformations[2].

Unlike Nb_3Sn, Nb_3Sb becomes superconducting only at very low temperatures (T_c<0.1°K). This property of Nb_3Sb makes several experiments much simpler since the strong Meissner effect of Nb_3Sn is easily quenched in Nb_3Sb. The electromagnetic properties of Nb_3Sn in the normal state can only be determined in magnetic fields in excess of 220 kGauss (H_{c_2}). Above T_c, Laundau level broadening is so large that quantum oscillations are damped out.

In order to understand these differences in the properties of Nb_3Sn and Nb_3Sb, which differ by only 1 electron in 173, we have undertaken the calculation of their electronic structure by *ab initio* means. Before discussing the calculations in the next chapters it is necessary to explain the crystal structure of the A-15 compounds, this is done below. A review on the status of the electronic structure of the A-15 materials also follows.

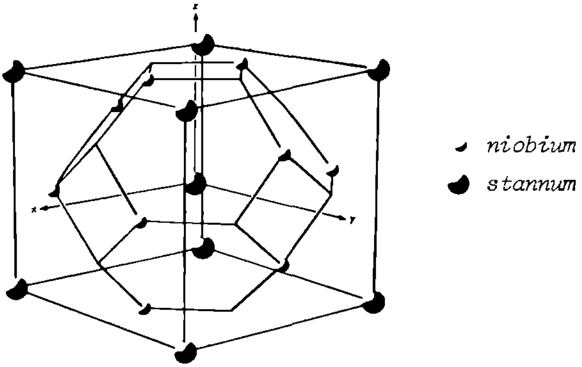

Figure 1.1 Primitive unit cell for A-15 compound Nb_3Sn

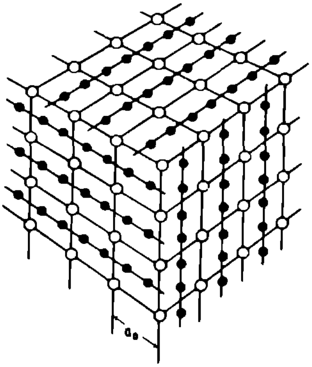

Figure 1.2 Extended arrangement of atoms in A-15 compounds

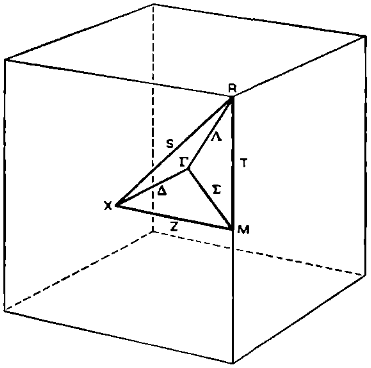

Figure 1.3 Brillouin zone for the simple cubic Bravais lattice

The simple cubic unit cell for the A-15 structure is shown in figure 1.1. The crystal, denoted as A_3B, has 2 B atoms and 6 A atoms per unit cell. The A atoms are always transition metal atoms, whereas the B atoms can be either transition metal or non-transition metal atoms. In the stoichiometric composition the B atoms form a body centered cubic lattice, while the A atoms are situated on three mutually orthogonal chains in the faces of the cubes. The interatomic separation in the chains (intrachain) is about 20% smaller than the separation between A atoms on different chains (interchain). The chain structure becomes much clearer if several unit cells are drawn (figure 1.2).

The space group for the cubic A-15 structure is O_h^3 (Pm3n), which is a non-symmorphic space group. With the origin at a B atom site, the symmetry operations for this space group are of two types. First, there are 24 space group operations of the form $\{\alpha|\vec{R}_n\}$, where α is a point group operation in T_h and $\vec{R}_n$ is a primitive translation $\vec{R}_n=a_0(n_1\hat{x}+n_2\hat{y}+n_3\hat{z})$. Here the n_i are integers and $\hat{x}$, $\hat{y}$ and $\hat{z}$ are unit vectors along the x, y and z axes, respectively. In addition, there are 24 space group operations $\{\alpha'|\vec{R}_n+\vec{\tau}\}$, where α' spans the remaining 24 point group operations on O_h and $\vec{\tau}$ is a nonprimitive translation $\vec{\tau}=\frac{1}{2}a_0(\hat{x}+\hat{y}+\hat{z})$. This latter space group operations, known as glide planes, make it more difficult to find the basis functions of the O_h^3 irreducible representations than in symmorphic cubic groups. The irreducible representations have been discussed by Gorzkowski[3] and Mattheiss[4]. The point group symmetry of the B sites is T_h(m3). The point group symmetry of the A sites is lower, D_{2h}($\overline{4}$2m).

The A-15 compounds have a simple cubic Bravais lattice. Therefore, the first Brillouin zone for them is also a cube, which is given in the figure 1.3. The notation of Bouckaert, Smoluchowski, and Wigner[5] (BSW) is to label the high symmetry points and lines. The irreducible representations for points inside the first Brillouin zone are equal to the corresponding representations inside the O_h^1 Brillouin zone. On the surface of the Brillouin zone the irreducible representations can be different[4]. The point group of the wave vector at the symmetry points X and M is D_{4h}, with sixteen operations. At X, four two-dimensional irreducible representations are found; at M, there are eight one-dimensional (M_i,i=1,8) and two two-dimensional (M_9 and M_{10}) representations. The point group of the wave vector at R is O_h, and there are three two-dimensional (R_i,i=1,3) and one six-dimensional representation (R_4). Gorzkowski[3] has pointed out that R_1 and R_2 are degenerate as a consequence of time reversal symmetry. Along the symmetry line T the point group of the wave vector is C_{4v}, there are four one-dimensional (T_i,i=1,4) and one two-dimensional (T_5) irreducible representations. The point group of the wave vector along the lines S and Z is C_{2v}, with four operations. Along S there is only one two-dimensional representation while Z has four one-dimensional representations.

The compatibility relations for points of the Brillouin zone are summarized in table 1.1. The notation used in this latter table is identical to that introduced by Mattheiss[6], except the relation between the M point and the Z line and two printing errors in the table of Mattheiss. The compatibility relations for the Γ point are given for example in reference 4.

The symmetry label of the calculated bands is determined from the wave function expressed in the plane wave basis (see APW section):

$$\phi = \sum_{j=1}^{N} C_j \psi_j = \sum_{j=1}^{N} C_j \exp[i(\vec{G}_j + \vec{k}).\vec{r}] \ . \tag{1}$$

To construct a linear combination of plane wave functions which transforms as an irreducible representation α, one must apply the projection operator

$$P_\alpha = \sum_R (\chi_R^\alpha)^* R \tag{2}$$

to an arbitrary plane wave basis vector Ψ_j[7]. R is an operator of the space group of wave vector $\vec{k}$, and χ_R^α is the character of the irreducible representation α. An extra complication arises from the complex nature of the glide plane operations. A glide plane is a product

TABLE 1.1 Compatibility relations for points of the Brillouin zone

X_1	X_2	X_3	X_4
S_1	S_1	S_1	S_1
Z_1Z_3	Z_2Z_4	Z_3Z_4	Z_1Z_2
$\Delta_1\Delta_2$	$\Delta_1'\Delta_2'$	Δ_5	Δ_5

R_1R_2	R_3	R_4
$2S_1$	S_1	$3S_1$
$2T_5$	T_5	$T_1T_2T_3T_4T_5$
$2\Lambda_3$	$\Lambda_1\Lambda_2$	$\Lambda_1\Lambda_2 2\Lambda_3$

M_1	M_2	M_3	M_4	M_5	M_6	M_7	M_8	M_9	M_{10}
Σ_4	Σ_4	Σ_2	Σ_2	Σ_1	Σ_1	Σ_3	Σ_3	$\Sigma_1\Sigma_4$	$\Sigma_2\Sigma_3$
Z_1	Z_3	Z_4	Z_2	Z_1	Z_3	Z_4	Z_2	Z_1Z_3	Z_2Z_4
T_2	T_1	T_2	T_1	T_4	T_3	T_4	T_3	T_5	T_5

of a point operation and a non-primitive translation, here $\vec{\tau}=\frac{1}{2}a_0(\hat{x}+\hat{y}+\hat{z})$. These glide planes introduce into the projector (2) an additional phase factor of the form:

$$\exp R[i\,\vec{G}.\vec{\tau}]\,.\ \exp R[i\,\vec{k}.\vec{\tau}] \qquad (3)$$

where G is a reciprocal lattice vector. The first factor can have the value ± 1 depending on the even- or oddness of the sum of the $\vec{G}$ components and the point group operator involved. The second factor is $\vec{G}$ independent and is constant in a plane wave basis at a particular $\vec{k}$ point.

In this section we summarize some of the theoretical and experimental work done on the class of A-15 compounds.

Since the discovery[9] in 1954 that V_3Si is superconducting at 17°K, most of the materials with the highest superconducting transition temperatures (T_c) have had the A-15 structure. In addition to high T_c values, a number of A-15 compounds have anomalous temperature dependences[2] of various normal state properties. The elastic constants, magnetic susceptibility and Knight shift are normally temperature independent in metals; in A-15 compounds they are T dependent, with the dependence generally being stronger for the higher T_c materials. Another fascinating property of the A-15 compounds with high T_c values is a structural transformation, actually characterized as Martensitic transformation, from cubic to tetragonal, at low temperature. The early X-ray determinations[10] indicated a Martensitic transformation at a transition temperature $T_m \simeq 21^\circ K$ for V_3Si and $T_m \simeq 45^\circ K$ for Nb_3Sn. T_m varies for different samples, this is attributed to deviations from perfect stoichiometry. Subsequently neutron diffraction studies by Shirane and Axe[11] verified a sublattice distortion of the Nb atoms in Nb_3Sn, a possibility suggested by Anderson and Blount[12] as a necessary accompaniment of a tetragonal distortion assuming that the order parameter has Γ_{12} symmetry. More recently, structural transitions have been seen in other high T_c A-15 materials. No transitions have been reported in low T_c A-15's.

Two different mechanisms have been proposed to explain the origin of these anomalous properties. The first involves an unusually sharp peak in the electronic density of states near the Fermi energy, $N(E_F)$. The detailed shape of the N(E) curve near E_F is not critical in these models, since qualitatively similar results are obtained by Clogston and Jaccarino[13] with a parabolic peak, Labbé and Friedel[14] with a square root singularity and Cohen *et al.*[15] with a step function. According to these models, $N(E_F)$ (per A atom) is typically 2 to 3 times larger than that derived by McMillan[16] for V and Nb metals from specific heat and superconductivity data. More important, these models infer that N(E) changes abruptly within a few mRy to a small fraction of its value at E_F.

The second mechanism, which has been proposed by Testardi[17], emphasizes the phononic rather than the electronic density of states. According to this model the unusually large anharmonic motion of the A atoms in the A-15 lattice at low temperatures is responsible for significant corrections to the specific heat and produces a strong temperature dependent phonon enhancement of the electronic properties of these materials.

Most simplified band models for the A-15 compounds emphasize the fact that the A atoms form three sets of mutually perpendicular chains for which the intrachain separation is about 20% smaller than the interchain separation. Weger[18] suggested that this would result in an one-dimensional band structure and Fermi surface for these compounds, provided that the second neighbor interchain interactions were negligible. This forms the basis for the Labbé-Friedel linear chain model[14] which treats the A atom *d* bands as being purely one-dimensional in character. These *d* bands are overlapped by a broad *s*-*p* band such that E_F falls within a few mRy of a square root singularity in N(E). This model could be fit to the T dependence of the normal state properties. Their model could also account, via a band Jahn-Teller mechanism which splits the degeneracy, due to the Martensitic transition, at low temperature. Gor'kov[19] has noted that the symmetry of the A-15 structure causes bands to stick together at the X point of the Brillouin zone. Placing E_F near a degenerate X level and including electron-electron interactions can account for the various T dependences. The model of Gor'kov can also explain the Martensitic transition. Recently, Lee *et al.*[20] have proposed a model based on a sixfold degenerate level at the R point in the Brillouin zone. The validity of this model is discussed in chapter IIb. Their model explains also the aforementioned anomalies. Its most notable attribute is that it does not assume any one-dimensional character of the electronic spectrum.

The disconcerting observation that distinct models (Labbé-Friedel, Gor'kov and variations on these) can describe the phenomena equally well has led Bhatt[21] to show that, despite different electron-lattice coupling mechanisms, the associated Landau models give results that are nearly identical in form. This suggests that perhaps none of the microscopic models proposed thus far are an accurate reflection of the A-15 electronic structure. Clearly, first principles approach to electronic structure would be desirable.

The field of *ab initio* band calculations for A-15 compounds was pioneered by Mattheiss[6], who carried out Augmented Plane Wave (APW) calculations on several A-15 compounds. These 1965 calculations were non self-consistent, were done only at high symmetry points in the Brillouin zone and were relatively poorly converged (∿30 mRy). These shortcomings were mostly due to computer limitations. Subsequent calculations by Mattheiss[22] in 1975 for V_3Si, V_3Ge, Nb_3Al and Nb_3Sn (all high T_c materials) had an order of magnitude better convergence. The calculations included a warped muffin-tin potential and the Linear Combination of Atomic Orbitals (LCAO) method was used as an interpolation scheme. The density of states and other related quantities were determined. Perhaps the main conclusion drawn from these studies was that there was no evidence for noticeable one-dimensional features in the electronic structure. Jarlborg and Arbman[23] have applied the Linear Muffin Tin Orbital (LMTO) method to a large number of A-15's and made comparison of the resulting density of states with experimental photoemission data. Klein *et al.*[24] have carried the APW method to self-consistency, including warping terms, but retaining a spherically averaged potential within the muffin-tin region (see chapter IIa). Lately Pickett *et al.*[25] reported A-15 band calculations for Nb_3Ge and Nb_3Al. There self-consistent pseudopotential method was applied. We[26] have also applied the APW method, but for the first time using a general form of potential across the entire crystal unit cell. Our energy bands are non self-consistent (see chapter V).

The relative sparcity of band structure results for a class of materials as important and poorly understood as the A-15's reflects the difficulty and expense of carrying through the calculations.

High precision experimental studies of the $\vec{k}$-space electronic structure of A-15 compounds are required in order to evaluate the importance of the various theoretical models. Experiments which probe the Fermi surface are essential. To date there have been a number of experimental investigations of the Fermi surface by a variety of of experimental techniques. Graebner and Kunzler[27] measured the magnetothermal oscillations of V_3Ge. Arko *et al.*[28] used the de Haas-van Alphen (dHvA) effect and studied Nb_3Sb. Arko *et al.*[29] observed dHvA oscillations in Nb_3Sn. These latter results were quite preliminary because of the inherent difficulty of the experiment[29]. High field magnetoresistance and Shubnikov-de Haas effect were studied by Sellmyer *et al.* [30]. The positron annihilation technique has also been applied to the study of the Fermi surface in V_3Si[31], which is isoelectronic to Nb_3Sn. More recently, two-dimensional angular correlation of angular radiation, preformed independently by Manuel *et al.*[32] and Farmer *et al.*[33], have yielded additional information concerning V_3Si.

Photoemission results have been compared to a variety of density of states calculations, some of which will be discussed below. NMR, specific heat and susceptibility measurements have also been untertaken, their results can also be used for density of states comparison. Numerous other measurements have been made including Knight shift and spin echo studies[34].

However our work deals mainly with the Fermi surface properties of Nb_3Sn and Nb_3Sb, thus the preceeding work will not be extensively discussed. We are mainly concerned with the relationship between theory and experiment of the Fermi surface and how it influences superconductivity.

References

1 G.Hägg,Z.Phys.Chem.,Abt.B,6,221 (1930);12,33 (1931)

2 Extensive reviews have been given by L.R.Testardi in *Physical Acoustics*,edited by W.P.Mason and R.N.Thurston (Academic Press, New York,1973) Vol.X;by M.Weger and I.B.Goldberg in *Solid State Physics*,edited by H.Ehrenreich,F.Seitz and D.Turnbull (Academic Press,New York,1973),Vol.28

3 W.Gorzkowski,Phys.Stat.Solidi 3,910 (1963)

4 L.F.Mattheiss,Solid State and Molecular Theory Group,Massachusetts Institute of Technology,Quarterly Progress Report 51,54 (1964) *(unpublished)*

5 L.P.Bouckaert,R.Smoluchowski and E.Wigner,Phys.Rev.50,58 (1936)

6 L.F.Mattheiss,Phys.Rev.138,A112 (1965)

7 T.Janssen,*Crystallographic Groups* (North Holland Publishing Company,Amsterdam,1973)

8 M.H.Boon,private communications

9 G.E.Hardy and J.K.Hulm,Phys.Rev.93,1004 (1954)

10 B.W.Batterman and C.S.Barrett,Phys.Rev.Lett.13,390 (1964); R.Mailfert,B.W.Batterman and J.J.Hanak,Phys.Lett.A24,315 (1967)

11 G.Shirane and J.D.Axe,Phys.Rev.B4,2957 (1971)

12 P.W.Anderson and E.I.Blount,Phys.Rev.Lett.14,217 (1965)

13 A.M.Clogston and V.Jaccarino,Phys.Rev.121,1357 (1961)

14 J.Labbé and J.Friedel,J.Phys.Radium 27,153 (1966)

15 R.W.Cohen,G.D.Cody and J.J.Halloran,Phys.Rev.Lett.19,840 (1967)

16 W.L.McMillan,Phys.Rev.167,331 (1968)

17 L.R.Testardi,Phys.Rev.B5,4342 (1972)

18 M.Weger,Rev.Mod.Phys.36,175 (1964)

19 L.P.Gor'kov,Zh.Eksp.Teor.Fiz.65,1658 (1973) [Sov.Phys.JETP 38,830 (1974)]

20 T-K.Lee,J.L.Birman and S.J.Williamson,Phys.Rev.Lett.39,839 (1977)

21 R.N.Bhatt,Phys.Rev.B16,1915 (1977)

22 L.F.Mattheiss,Phys.Rev.B12,2161 (1975)

23 T.Jarlborg and G.Arbman,J.Phys.F6,189 (1976);7,1635 (1977)

24 B.M.Klein,L.L.Boyer and D.A.Papaconstantopoulos,J.Phys.F8,617 (1978)

25 W.E.Pickett,K.M.Ho and M.L.Cohen,Phys.Rev.B19,1734 (1979)

26 A.T.van Kessel,H.W.Myron and F.M.Mueller,Phys.Rev.Lett.41,181 (1978)

27 J.E.Graebner and J.E. Kunzler,J. of Low Temp.Phys.1, 443 (1969)

28 A.J.Arko,Z.Fisk and F.M.Mueller,Phys.Rev.B16,1387 (1977)

29 A.J.Arko,D.H.Lowndes,F.A.Muller,L.W.Roeland,J.Wolfrat,A.T.van Kessel,H.W.Myron,F.M.Mueller and G.W.Webb,Phys.Rev.Lett.40,1590 (1978)

30 D.J.Sellmyer,D.Liebowitz,A.J.Arko and Z.Fisk, J.of Low Temp.Phys. 40, 629 (1980)

31 S.Berko and M.Weger,Phys.Rev.Lett.24,55 (1970)

32 A.A.Manuel,S.Samoilov,M.Peter and A.P.Jeavons,Helv.Phys.Acta 52, 37 (1979);A.A.Manuel,S.Samoilov,R.Sachot,P.Descouts and M.Peter, Solid State Comm.31,955 (1979)

33 W.S.Farmer,F.Sinclair,S.Berko and G.M.Beardsley,Solid State Comm. 31,481 (1979)

34 N.J.Poulis,publications and theses from co-workers

CHAPTER II : BAND STRUCTURE METHODS APPLIED TO A15 COMPOUNDS

This chapter describes the computational methods that are used to obtain the theoretical pictures of the two A-15 compounds Nb_3Sn and Nb_3Sb. Discussed here are the Augmented Plane Wave (APW) method for calculating the energy bands; the generalized $\vec{k}.\vec{p}$ method for fitting these bands and the tetrahetron method for Brillouin zone integrations.

IIa : The APW method

The first section gives the common concepts of the APW method, while the second section explains the necessary crystal potential approximations used in the APW method which are needed for performing APW calculations on non-spherical A-15 compounds. The third section lists the potential - and APW calculation details.

Concepts

The Augmented Plane Wave method was originally proposed in 1937 by J.C. Slater[1]. Of course, at that time there were no high speed computers available. The first calculation, done in 1939, had to be carried out using a desk calculator. In the 1950's there were some suggested modifications in an attempt to simplify the original scheme. In the beginning of the sixties the Solid State and Molecular Theory Group under direction of Slater at M.I.T. programmed the original form on a Whirlwind computer. From that time on a flood of calculations started to appear in the literature. In the last twenty years the 1937 form of the APW has been extended, without changing in essence. These extensions are self-consistency, corrections to non-sphericity of the crystal potential and relativistic generalizations. Here we explain the APW method as far as necessary to understand certain modifications applied here and the inherent limitations of our calculations. For a complete understanding of the method the interested reader can consult either the book by Loucks[2] or the review articles by Dimmock[3] and Mattheiss *et al.*[4]

In a perfect stoichiometric infinite crystal the electronic potential energy is completely repetitious. This periodicity can be expressed for a cubic unit cell by

$$V(\vec{r})=V(\vec{r}+\vec{R}) \tag{1}$$

where

$$\vec{R}=a_0(n_1\hat{x}+n_2\hat{y}+n_3\hat{z}) \tag{2}$$

Here a_0 is the lattice constant and the n_i are integers and $\hat{x}$, $\hat{y}$ and $\hat{z}$ are unit vectors along the main axes. Block's theorem

$$\psi_h(\vec{r}+\vec{R})=\psi_h(\vec{r}).\exp[i(\vec{k}.\vec{R})] \tag{3}$$

states that the same periodicity can be found in the electronic density $|\psi|^2$. However, the wave function ψ has different phases in different unit cells. The space of wave vector $\vec{k}$, the reciprocal space also has a periodicity. A state with wave vector $\vec{k}+\vec{G}$, where $\vec{G}$ is defined by

$$\vec{G}=\frac{2\pi}{a_0}\,(m_1\hat{k}_x+m_2\hat{k}_y+m_3\hat{k}_z) \tag{4}$$

with the m_i integers and $\hat{k}_x$, $\hat{k}_y$ and $\hat{k}_z$ the basis vectors of the reciprocal cubic lattice, satisfies the Block condition as if it had the wave vector $\vec{k}$. To describe the electronic structure of a crystal it is sufficient to consider those wave vectors contained inside the smallest region, called Brillouin zone, bounded by the planes which perpendicularly bisect the reciprocal vectors given in (4). For a cubic unit cell,

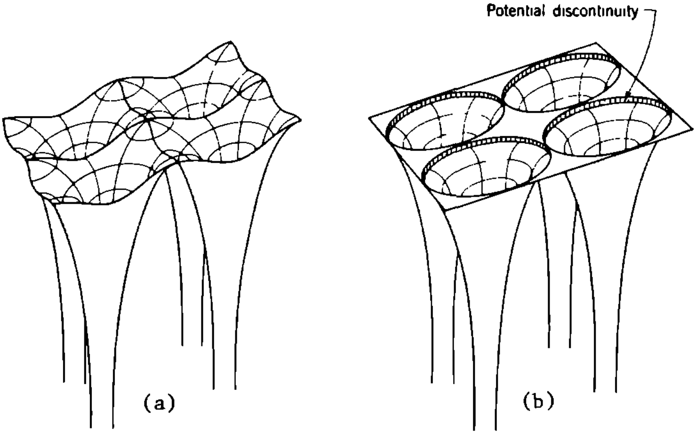

Figure 2.1 Crystal potential (a) and muffin-tin potential (b) of a spuare two-dimensional lattice (after Slater[11]*)*

as in the A15's, the Brillouin zone is also a cube, with the edge length equal $\frac{2\pi}{a_0}$. In order to represent all the different states which happen to have the same wave vector inside the Brillouin zone, a complete set must include either all of the wave vectors $\vec{k}+\vec{G}$ in a plane wave representation or all bands n.

The APW method is traditionally based on the muffin-tin or spherical approximation to the actual crystal potential, $V(\vec{r})$: inside spheres centered at each atomic site, the potential is assumed to be spherically symmetric, and outside these spheres the potential is taken to be constant. For many materials especially closed packed metals this is a good approximation. In fig. 2.1 we illustrate by a two dimensional case the nature of this potential. This simplification also yields accurate results in transition metals; in fact in these systems the non-spherical components of the potential are quite small, since the major part of the *d* electrons are localized near the nuclei. The muffin-tin approximation can also give useful results in compounds in which the site symmetry of each atom is high (e.g. cubic). In the A-15 structure a prominent feature is the relatively low site symmetry of the A transition metal atoms. In addition, the A atom nearest neighbors typically lie $\sim$8% closer in the A-15 structure than in the bcc structure for the A atoms. This leads us to expect significant deviations from spherical symmetry within the muffin-tin region in the A-15 structure.

Within the APW method, corrections can easily be made for non-constant behavior of the potential outside the spheres, but non-spherical corrections inside the spheres are much more difficult to treat. This difference comes from the different character of the assumed crystal wave function used in the APW variational method.

The crystal wave function is of the form

$$\Phi=\sum_{j=1}^{\infty} C_j \; \Psi(\vec{k}+\vec{G}_j,\vec{r}) \tag{5}$$

where C_j are the expansion parameters which determine the energy and symmetry of Φ, and the Ψ's are the APW functions. The APW functions have outside the muffin-tin spheres the form

$$\Psi_j(\vec{k},\vec{r})=\exp\left[i(\vec{k}+\vec{G}_j)\cdot\vec{r}\right] \tag{6}$$

and inside

$$\Psi(\vec{k},\vec{r})=\sum_{lm}^{\infty} A_{lm}(\vec{k}) \; Y_{lm}(\hat{r}_s) \; R_l(r_s,E) \tag{7}$$

where l and m are the angular momentum quantum numbers, r_s and $\hat{r}_s$ are length and angle of $\vec{r}_s$, respectively, where r_s is the position according to the muffin-tin centre. $A_{lm}(\vec{k})$ are the coefficients which are determined from the continuity of the wave function at the sphere boundaries, $Y_{lm}(\hat{r}_s)$ are spherical harmonics, and $R_l(r_s,E)$ are the radial solution of the Schrödinger equation for the spherical potential. The $A_{lm}(\vec{k})$ have the following expansion

$$A_{lm}(\vec{k})=4\pi \; \exp\left[i(\vec{k}.\vec{R}_s)\right] \; i^l Y^*_{lm}(\hat{k}) \; J_l(kR_s)/R_l(R_s,E) \tag{8}$$

where $\vec{R}_s$ and R_s are the position and the radius of the muffin-tin sphere respectively. $J_l(kR_s)$ is a spherical Bessel function or order l. The values of the $A_{lm}(\vec{k})$'s ensure that each of the APW basis functions is continuous at the sphere boundaries. Since in practice the number of basis functions is limited, the derivative of the crystal wave function (5) is discontinuous. As more APW functions are added to the basis, the slope discontinuity is reduced.

The values of the expansion coefficients C_j are determined variationally. The variational expression for the energy can be written as

$$E\int\Phi^*\Phi d\Omega=\int\Phi^*H\Phi d\Omega-\tfrac{1}{2}\int(\Phi^*_{IN}+\Phi^*_{MT})(\frac{\delta}{\delta r}\Phi_{IN}-\frac{\delta}{\delta r}\Phi_{MT})dS \qquad (9)$$

where the first two integrals are over the entire unit cell and the last one over the surface of the muffin-tin spheres. Φ_{IN} is the wave function written as a linear combination of APW's with the form (6) in the interstitial region and Φ_{MT} in the form (7) in the muffin-tin region. The last term in equation (9) arises from the slope discontinuity.

The next step is to determine the expansion parameters C_j in equation (5), by minimizing the energy with respect to each coefficient

$$\frac{\delta E}{\delta C_j}=0 \qquad (10)$$

This constraint gives the equations

$$\sum_j^{\infty}[H^{ij}+S^{ij}-E\,\Delta^{ij}]\,C_j=0 \qquad (11)$$

where the part within the brackets comes from equation (9) by substituting in equation (5). Non-trivial solution of C_j's will only be found if the secular determinant is zero. The matrix elements of the APW matrix can be written[2] as

$$M^{ij}=H^{ij}+S^{ij}-E\,\Delta^{ij}=\Omega_0(k_j^2-E)\,\delta_{ij}-4\pi\sum_s R_s^2\,e^{i\,\vec{k}_{ij}\cdot\vec{R}_s}\,G_s^{ij} \qquad (12)$$

where

$$G_s^{ij}=(\vec{k}_i\cdot\vec{k}_j-E)\mathcal{J}_1(k_{ij}R_s)/k_{ij}$$

$$-\sum_l^{\infty}(2l+1)P_l(\vec{k}_i\cdot\vec{k}_j)\mathcal{J}_l(k_iR_s)\mathcal{J}_l(k_jR_s)R_l'(R_s,E)/R_l(R_s,E) \qquad (13)$$

The APW matrix elements are energy dependent. Since the APW functions are not orthogonal, the energy dependence occurs explicitly in both the diagonal and off-diagonal matrix elements. Furthermore, the energy also appears implicitly in the logarithmic derivatives R_l'/R_l. Consequently, the only feasible way of solving equation (11) is to evaluate the matrix elements and secular determinant as a function of energy and use an interpolation procedure to determine the zeros.

Potential extensions

As pointed out above the muffin-tin approximation is not as good for the A-15 structure as it is for more close packed crystal structures. This problem arises from the low symmetry (D_{2h}) and expected anisotropic electronic density at the A sides. Corrections to the muffin-tin potential are necessary in an APW band calculation of an A-15 compound.

The correction for potential variations from the average in the interstitial region is not difficult to achieve. The APW functions have in this region a plane wave character, so the correction to the APW matrix elements has the form

$$\Delta H_{IN}^{ij} = \frac{1}{\Omega} \int e^{-i(\vec{k}+\vec{G}_i).\vec{r}} \, (V(\vec{r})-\bar{V}_{IN}) \, e^{i(\vec{k}+\vec{G}_j).\vec{r}} \, d\Omega \tag{14}$$

where the integration is over the interstitital region. Ω is the unit cell volume, and $\bar{V}_{IN}$ is the potential averaged over the interstitial region. It is impossible to perform the integration analytically, because the crystal potential is not known in an analytic form. So the integration is replaced by a summation

$$\Delta H_{IN}^{ij} = \frac{\Omega_{IN}}{\Omega} \sum_{n=1}^{N} (V(\vec{r}_n)-\bar{V}_{IN}) \, e^{i\,\vec{r}_n.(\vec{G}_j-\vec{G}_i)} \tag{15}$$

where Ω_{IN} is the volume of the interstitial space, and N the number of points in real space where the potential is calculated. Equation (15) is an ordinary Fourier transformation of the crystal potential. Since equation (15) is independent of $\vec{k}$ and E, it has to be evaluated only once for a particular potential and set of plane waves.

In order to avoid the difficult but necessary potential corrections inside the muffin-tins one can diminish the sphere radii, until $V(\vec{r}_s)$ is spherical. The figures 2.2 and 2.3 show the crystal potential in an [100] plane for Nb_3Sn and Nb_3Sb, respectively. The dashed lines show the maximum possible sphere radii, keeping the A and B spheres of equal size, without overlapping spheres. The A and B sphere radii are kept equal only because of computational advantages, i.e. the sum in equation (12) is easier to evaluate. Averaging the potential while using the maximum possible Nb spheres will cause severe losses in accuracy, since the potential on the spheres varies from 0.4 Ry in the chain direction to 0.8 Ry. This variation is too big to be ignored. With a shorter radius this potential correction is transferred to the interstitial region, where the potential deviations are correctable by equation (15). This leads to much smaller spheres namely the bold ones in the figures. The convergence in the energy levels becomes poor since the plane waves have to describe much more potential structure; the potential is far from free electron like. An APW calculation with interstitial corrections and with this small radius turned out to be impossible, because the bands become converged using an APW function basis of size 750! This is an impossible task with the performance time of today's computers, since the time to solve the secular matrix goes as N^3 where N is the number of APW basis functions.

Hence, non-spherical potential corrections inside the muffin-tin spheres are necessary for the A-15 band calculations. The additions to the APW matrix elements has the form

$$\Delta H^{ij}_{MT} = \langle\Psi|V(\vec{r}_s)-\bar{V}_{MT}(r_s)|\Psi\rangle \qquad (16)$$

where $\bar{V}_{MT}(r_s)$ is the spherical average at a particular radius r_s. The wave function is expressed by equation (7). The integration is over all muffin-tin space in one unit cell.

It is convenient to write the potential corrections in equation (16) in terms of spherical harmonics, because the wave functions are also expressed in spherical harmonics. The expansion of ΔV has the form

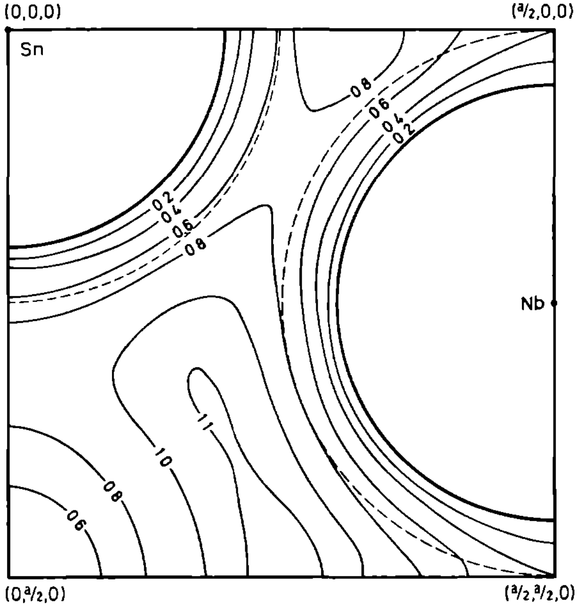

Figure 2.2 Crystal potential in the [100] *plane of* Nb_3Sn

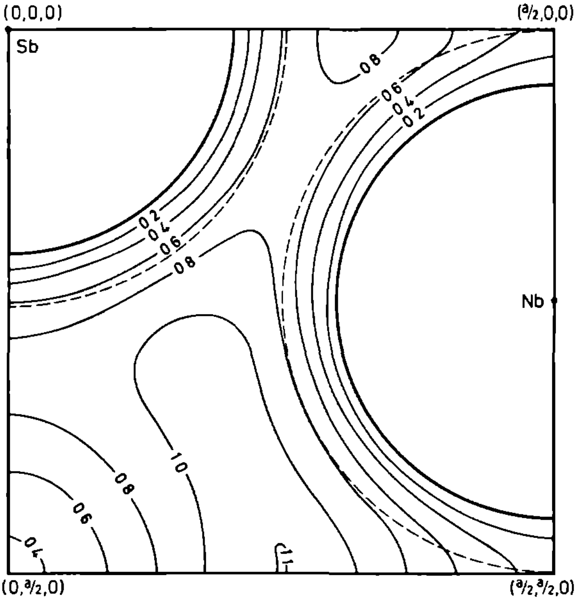

Figure 2.3 Crystal potential in the [100] *plane of* Nb_3Sb

$$V(\vec{r}_s) - \bar{V}_{MT}(r_s) = \sum_{LM} Y_{LM}(\hat{r}_s)\, V_{LM}(r_s) \tag{17}$$

for every radius of length r_s. The evaluation of this equation is discussed in the next section. Attention should be paid to equation (17): in the standard APW scheme only the value zero is allowed for the quantum numbers L and M. For each muffin-tin sphere equation (16) becomes

$$\Delta H^{ij}_{MT}(s) = \frac{1}{\Omega_0} \int d\Omega \sum_{l'm'} A^*_{l'm'}(\vec{k}_i)\, Y^*_{l'm'}(\hat{r}_s) R_{l'}(r_s,E)$$

$$\sum_{LM} Y_{LM}(\hat{r}_s) V_{LM}(r_s) \sum_{lm} A_{lm}(\vec{k}_j) Y_{lm}(\hat{r}_s) R_l(r_s,E) \tag{18}$$

Reorganizing this equation in angle and radial dependence gives

$$\Delta H^{ij}_{MT}(s) = \frac{1}{\Omega_0} \sum_{l'm'} A^*_{l'm'}(\vec{k}_i) \sum_{lm} A_{lm}(\vec{k}_j) \sum_{LM} \int_0^{R_s} r_s^2 dr_s\, R_{l'}(r_s,E) V_{LM}(r_s) R_l(r_s,E)$$

$$\int_0^{\pi} \int_0^{2\pi} \sin\theta\, d\theta\, d\phi\, Y^*_{l'm'}(\hat{r}_s)\, Y_{LM}(\hat{r}_s)\, Y_{lm}(\hat{r}_s) \tag{19}$$

The radial integration in equation (19) will be labelled $I^{LM}_{l'l}$ and is performed analogous to the standard APW scheme, see Loucks[2] pages 56 through 60. This integration results in polynomials in energy. Since the potential is no longer spherically symmetric the corrections of (19) include coupling between l and l'. In the spherically symmetric case, only diagonal terms survive. The angular integration in equation (19) is labelled $C^{LM}_{l'm'lm}$ and are just Gaunt coefficients. For the evaluation of the Gaunt coefficients the reader should consult Rotenberg[5] or Messiah[6]. Equation (19) gives the muffin-tin corrections for one sphere. To obtain the total corrections a summation over the 8 sites in the A-15 unit cell is required

$$\Delta H^{ij}_{MT} = \frac{1}{\Omega_0} \sum_{s} \sum_{l'm} \sum_{lm} A^{*}_{l'm'}(s,\vec{k}_i)\, A_{lm}(s,\vec{k}_j) \sum_{LM} C_{l'm'lm} I^{LM}_{l'l'}(s,E) \qquad (20)$$

Substituting equation (8), from which the R_l's are already included in the $I^{LM}_{l'l}$'s, in equation (20) gives

$$\Delta H^{ij}_{MT} = \sum_{s} \sum_{l'm} \sum_{lm} (4\pi)^2 (-i)^{l'} (i)^{l} \exp[-i(\vec{k}+\vec{G}_i).\vec{R}_s + i(\vec{k}+\vec{G}_j).\vec{R}_s] \ldots .$$

$$Y_{l'm'}(\hat{k}_i) Y^{*}_{lm}(\hat{k}_j) \mathcal{J}_{l'}(k_i R_s) \mathcal{J}_{l}(k_j R_s) \sum_{LM} C^{LM}_{l'm'lm} I^{LM}_{l'l}(s,E)$$

Rewriting the above expression yields

$$\Delta H^{ij}_{MT} = \sum_{l'} \mathcal{J}_{l'}(k_i R_s) \sum_{l} \mathcal{J}_{l}(k_j R_s) \sum_{m'} Y_{l'm'}(\hat{k}_i) \sum_{m} Y^{*}_{lm}(\hat{k}_j) P_{l'l\,m'm}(\vec{G}_j - \vec{G}_i, E) \qquad (21)$$

with

$$P_{l'l\,m'm}(\vec{G}_j - \vec{G}_i, E) = \frac{16\pi^2 (-i)^{l'} (i)^{l'}}{\Omega_0} \sum_{s} \exp[i(\vec{G}_j - \vec{G}_i).\vec{R}_s] \sum_{LM} C^{LM}_{l'm'lm} I^{LM}_{l'l}(s,E) \qquad (22)$$

The polynomials expressed by equation (22) depend on the quantum numbers $l'm'l$ and m, and the differences of the reciprocal lattice vectors, included in the APW basis functions. The polynomials are independent of the wave vector in the Brillouin zone, so they are calculated once an for all outside the main APW program. A mention should be made about the real or complex character of these corrections. Because the A-15 crystal includes inversion symmetry, only the real part of the complex terms, like spherical harmonics, phase factors and powers of i, will survive. The imaginary contributions to the corrections will average to zero. Thus real arithmetic routines for solving the secular matrix can be used rather than complex ones, resulting in a 4 fold computer time savings.

The choice of crystal potential is of prime importance for the accuracy of a non-self-consistent band calculation. The crystal potential is approximated by a potential derived from a superposition of Hartree-Fock-Slater self-consistent atomic charge densities. The assumed atomic configuration for Nb is $4d^2 5s^1$, while that of the B atoms is either $5s^2 5p^2$(Sn) or $5s^2 5p^3$(Sb). The Slater exchange contribution to the atomic potential is taken into account (α=1). A very good discussion of the method and a tabulation of results for all the elements is given by Herman and Skillman[7].

The muffin-tin potential is generated through the method suggested by Mattheiss[8]. In this approach the spherically symmetric contributions from the neighboring atoms are superimposed on the potential of the concerned atom. The exchange and Coulombic contributions are treated separately. The Coulombic part is composed of contributions of the form

$$V_0(r)=2\ Z/r - U_0(r) \tag{23}$$

where Z is the nuclear charge, and $U_0(r)$ is the electronic contribution, i.e. the solution of Poisson's equation

$$\nabla^2 U_0(r) = -8\pi\ \rho_0(r) \tag{24}$$

based on the atomic electronic density

$$\rho_0(r) = \sum_{\text{occupied}} |\ \Psi_{lm}\ |^2 \tag{25}$$

The Ψ_{lm}'s are the densities obtained from the Hartree-Fock-Slater calculation. The contributions from neighboring atoms are determined from

$$V_c(\vec{r}) = V_0(r) + \sum_i V_0(a_i|\vec{r}) \tag{26}$$

where the sum is over all close neighbors, and $V_0(a_i|\vec{r})$ is the spherical symmetric contribution from the Coulombic potential of neighbor i at a distance a_i from the atom concerned. The $V_0(a_i|\vec{r})$ are calculated through the application of Löwdin alpha expansion[9], which is basically an origin transformation.

The exchange contribution is treated using Slater's free electron exchange approximation[10]

$$V_x(\vec{r}) = -6\alpha\left(\frac{3}{8\pi}\rho(\vec{r})\right)^{1/3} \tag{27}$$

where α is chosen equal to one, this is a common value for non-selfconsistent calculations. $\rho(\vec{r})$ is the crystal electronic density and is approximated by adding to the atomic electronic density $\rho_0(r)$ the contributions from neighboring atoms, analogous to the Coulombic part in equation (26).

Adding the Coulombic and exchange contributions for every atom in the unit cell we get the crystal potential

$$V_t(\vec{r}) = V_c(\vec{r}) + V_x(\vec{r}) \tag{28}$$

Outside the muffin-tin spheres this potential is averaged over 1664 random $\vec{r}$-points in one eighth of the unit cell, to obtain the interstitial potential average ($\bar{V}_{IN}$). By shifting the potential inside the spheres this amount, the average becomes zero, as was assumed in the derivation of the matrix elements[2] in equation (12). Inside the muffin-tin spheres $V_t(\vec{r})$ is angle averaged, and substracted by the interstitial average. This procedure yields the muffin-tin potential ($\bar{V}_{MT}(r)$) which gives on the sphere boundaries discontinuities in the approximated crystal potential.

The differences between crystal potential $V_t(\vec{r})$ and the muffin-tin potentials ($\bar{V}_{MT}(r)$ and $\bar{V}_{IN}$) are included through the correction methods discussed in the previous section. For the interstitial corrections the actual crystal potential $V_t(\vec{r})$ is calculated on an $a_0/15$ mesh in one eighth of the unit cell, of course only outside the muffin-tins. These $V_t(\vec{r}_i)$ are input to a Fourier transformation program which evaluates equation (15).

The deviations from spherical average inside the muffin-tins were calculated and included in the APW matrix elements only for the Nb sites. From an examination of figures 2.2 and 2.3 it is visible that the spherical deviations for Sn and Sb are small inside the entire range of the muffin-tin spheres (the dashed lines). For the Nb sites the potential corrections were calculated in the region between the spheres with radius $a_0/8$ and the dashed spheres, radius $a_0/4$; see figures 2.2 and 2.3. The dashed spheres are the actual muffin-tin spheres. In the radial integration of equation (19) twenty three radii were chosen from which the $V_{LM}(r_s)$'s were calculated. The potential corrections $V_{LM}(r_s)$ were obtained from equation (17) by writing them explicitly. This is done by multiplying the left and right side in (18) by $Y^*_{lm}(\hat{r}_s)$

$$Y^*_{lm}(\hat{r}_s)\ [V(\vec{r}_s)-\bar{V}_{MT}(r_s)] = \sum_{LM} Y^*_{lm}(\hat{r}_s)\ Y_{LM}(\hat{r}_s)\ V_{LM}(r_s) \qquad (29)$$

An angle integration of both sides gives

$$\int_0^{\pi} \sin\theta d\theta \int_0^{2\pi} d\phi\ Y^*_{lm}(\hat{r}_s)\ \Delta V(\vec{r}_s) = V_{LM}(r_s)\ \delta_{lL}\ \delta_{mM} \qquad (30)$$

where $\Delta V(\vec{r}_s)$ is the potential deviation from the spherical average. The right side of equation (30) is equal to $V_{lm}(r_s)$ because of the orthonormality of the spherical harmonics[11]. The calculation of the integrals are done by a seventh order Gaussian integration[12] for Θ and a Simpson integration[12] for ϕ. The integration areas are restricted because of symmetry reasons, to one eighth of a sphere where the potential is evaluated on 56 points per shell. An expression of the $Y^*_{lm}(\hat{r}_s)$ can be found in reference 11.

The LM sum, which has to be done only once per Nb-site, is evaluated in the final expression of the muffin-tin corrections (equation (21)), up to L equal 6. The $l'm'$ and lm sums which have to be calculated in the APW run, are limited to l' and l equal 2. This means *p* and *d*-type corrections. If we also included *f* and *g*-type corrections the variation in the total correction is less than 10%. The *d*-type corrections are the most important in the A-15 band calculations because of the linear chain structure of the Niobium atoms. The higher corrections are not important for the actual bands on a scale of 2-3 mRy.

Before discussing the effect of the potential corrections on the bands, a few words should be written about the nature of the energy bands. Figure 2.4 shows all the calculated valence bands and the lower conduction bands for Nb_3Sn. The two bands situated between 0.0 and 0.2 Ry are characterized as Sn-*s* bands. The next six bands (at Γ:Γ_{25} and Γ_{15}) are mainly of Sn-*p* character. The next group of thirty bands (not all plotted) which cross the Fermi energy, corresponds to Niobium *4d* bands. The Fermi energy is calculated from an integration of the bands (see chapters IIc and III), and counting the number of valence electrons in one unit cell. This number is 38 for Nb_3Sn, while Nb_3Sb contains 40 valence electrons per unit cell.

The two potential corrections, muffin-tin and interstitial together which form the general potential in the APW calculation influence individual energy bands in a complex way. This is demonstrated in figure 2.5. The figure shows the influence of the two potential corrections separately for the high symmetry points in the Brillouin zone. These are, of course, the labelled IN and OUT. The inside corrections have the biggest effect on the Nb *d* orbitals, the bands above 0.5 Ry. The B atom *s* bands, the lowest two bands, are not affected by muffin-tin corrections. These effects can be understand through the knowledge that *s* electrons have less probability to be found inside the muffin-tins than *d* like electrons. The absolute value of both corrections is about the same; approximately 30 mRy. These corrections are not negligible for band structures like the A-15's where bands are narrow. From figure 2.5 it is also visible that even the ordering of the *d* bands is changed through the application of the potential corrections.

At this point all the potential corrections have been discussed. What is missing are the common APW parameters. The structure related quantities are listed in table 2.1. The expansion of the individual APW functions in atomic orbitals, equation (7), is done for *l* up to 7.

Figure 2.4 Band structure of Nb_3Sn along high symmetry directions

Figure 2.5 Influence of the potential corrections on high symmetry points of Nb_3Sb (IN *= inside Nb muffin-tins,* OUT *= interstitial)*

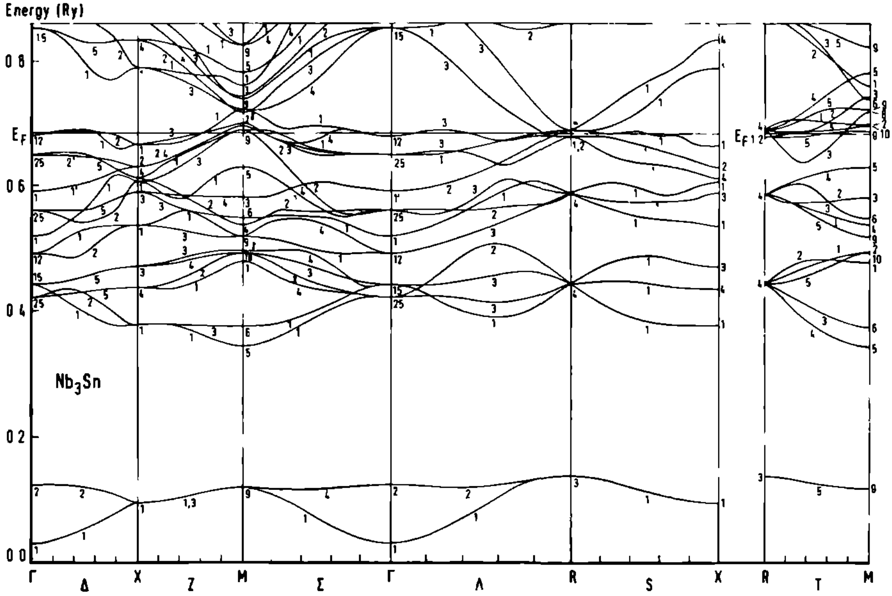

Figure 2.4

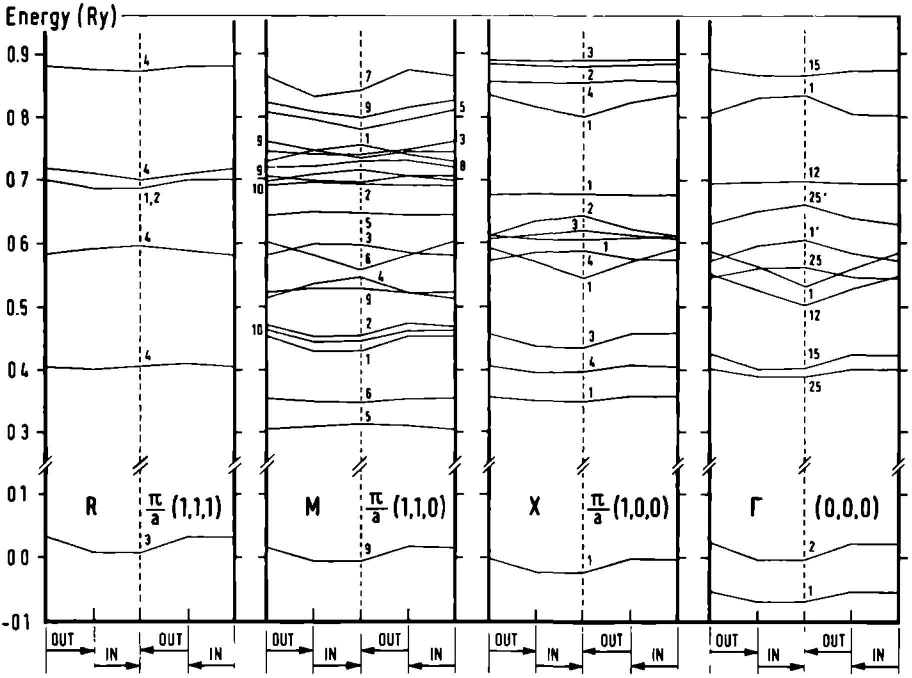

Figure 2.5

TABLE 2.1 Summary of the structure related parameters involved in the APW calculation for Nb_3Sn and Nb_3Sb

	Nb_3Sn	Nb_3Sb	
Lattice constant, a_0	5.282 9.981	5.254 9.928	Å a.u.
Niobium sphere radius, R_s	2.477	2.477	a.u.
B atom sphere radius, R_s	2.477	2.477	a.u.
Fraction of unit cell in interstitial region	0.512	0.520	

For this high upper maximum of l one may expect that the APW function is continuous at the sphere boundaries. The crystal wave function Φ of equation (5) in our calculations includes a summation over 300 APW wave functions. Energy calculations for different size of expansions (up to 432 APW's) of the crystal wave function show that these calculations are converged better than 3 mRy. The precise number of APW's included depends on the wave vector $\vec{k}$ in the Brillouin zone. Around every $\vec{k}$ point a sphere of $\vec{G}$'s is constructed, which includes complete shells of equivalent $\vec{G}$'s. So the size of the APW matrix can vary slightly from 295 to 305 members.

The zeros in the determinant of the energy dependent APW matrix have to be detected, see page 25 . This is done by calculating for every input energy the eigenvalue spectrum and iterating until the absolute smallest eigenvalue approaches zero. The CPU time necessary for a single shot, one $\vec{k}$ and one E value, is 223 seconds on an IBM 370/158 computer. This time is a summation of 19 sec. ordinary APW, 1 sec. interstitial potential corrections, 45 sec. muffin-tin potential corrections and 158 sec. diagonalization. For a discussion of the timing on different computers the reader should consult Appendix B.

1 J.C.Slater,Phys.Rev.51,846 (1937)

2 T.L.Loucks,*Augmented Plane Wave Method* (W.A.Benjamin Inc.,New York, (1967)

3 J.O.Dimmock in *Solid State Physics,* edited by H.Ehrenreich,F.Seitz and D.Turnbull (Academic Press,New York,1971),Vol.26

4 L.F.Mattheiss,J.H.Wood and A.C.Switendick in *Methods in Computational Physics,* edited by B.Alder,S.Fernbach and M.Rotenberg (Academic Press, New York,1968),Vol.8

5 M.Rotenberg,R.Bivins,N.Metropolis and J.K,Wooten jr,*The 3-j and 6-j Symbols* (Technology Press M.I.T.,Cambridge Mass,1959)

6 A.Messiah,*Quantum Mechanics* (North Holland Publishing Company, Amsterdam,1961),Vol.II

7 F.Herman and S.Skillmann,*Atomic Structure Calculations* (Prentice-Hall Inc.,Englewood Cliffs,N.J.,1963)

8 L.F.Mattheiss,Phys.Rev.133,A1399 (1964)

9 P.O.Löwdin,*Advanced Physics* Vol.5,1 (1956)

10 J.C.Slater,Phys.Rev.81,385 (1951)

11 J.C.Slater,*Quantum Theory of Matter* (McGraw-Hill Book Company, New York,1968)

12 M.Abramowitz and I.A.Stegun,*Handbook of Mathematical Functions* (Dover Publications Inc.,New York,1970)

IIb : Generalized $\vec{k}.\vec{p}$ interpolation scheme

Survey

For the calculation of many of the electronic properties of metals a high density mesh band structure is required. Of course one can calculate the energy spectra at all the necessary $\vec{k}$ points from an *ab initio* energy program, but this will use a enormous amount of computer time. The alternative is to work with a model Hamiltonian, which is fitted to the *ab initio* band structure. One of the earliest applications of model Hamiltonian schemes was the $\vec{k}.\vec{p}$ method, based on perturbation theory[1]. Generally this technique has been restricted to considering the electronic structure of semiconductors or semimetals for which only a few bands, local in $\vec{k}$ space, were of interest[2]. The $\vec{k}.\vec{p}$ method forms a convenient and simple scheme to interpolate both energy and wave function. For the A-15 compounds which have many bands theorists have applied other methods, such as the parametrized tight-binding scheme also known as the Slater-Koster method, first utilized for these class of compounds by Mattheiss[3] and Weger[4]. Also pseudopotential techniques have been used by Pickett[5] and Weger[4]. Alternatively much of the recent effort in A-15 band theory has been focussed on the use of techniques to speed up first-principles methods, e.g. LMTO by Jarlborg[6]. Since there will always be problems in which the effects of a few bands out of many dominate the physics, it is clear that the smaller secular matrices available in model Hamiltonians will have their use.

H.J.F.Jansen and F.M.Mueller[7] reexamined the idea of $\vec{k}.\vec{p}$ like model Hamiltonians, $H(\vec{k})$, which approximates the energy band structure in a series of polynomial expansions about selected high symmetry points, $\vec{K}_i$. The polynomial expansion coefficients are symmetry restricted by the transformation properties of the underlying reciprocal lattice and the band structure is initially fit to the high symmetry points while preserving local point group symmetry. Applying this method to the A-15 band structure did not affect the overall accuracy of our calculations. The $\vec{k}.\vec{p}$ error was only about 1 mRy small compared to the APW convergence error of about 2-3 mRy. However, by employing the $\vec{k}.\vec{p}$ method the calculations gained four orders of magnitude in speed. Through this scheme we were able to calculate de Haas-van Alphen frequencies, effective masses and Fermi velocities.

Theory

Here we will summarize the theoretical background on which the model Hamiltonians are based. For a more complete review the interested reader is referred to the work of Jansen and Mueller[7] or Birman, Lee and Berenson[8].

From the Schrödinger equation and using a complete set of Kohn-Luttinger basis functions $\Psi_n(\vec{k},\vec{r})$ the energy matrix elements have the following form

$$H_{nm}(\vec{k}) = \int d^3r\, \Psi_n^*(\vec{k},\vec{r})\,[-\Delta+2(\vec{k}-\vec{K}).\vec{p}+(\vec{k}-\vec{K})^2+V(\vec{r})]\,\Psi_m(\vec{k},\vec{r}) \tag{1}$$

We want to restrict the Schrödinger equation to a small set of levels near the Fermi energy. This can be done using Löwdin perturbation theory. We construct the matrix

$$U_{nm}(\vec{k},E) = H_{nm}(\vec{k}) + \sum_{\alpha} \frac{H_{n\alpha}(\vec{k})H_{\alpha m}(\vec{k})}{E-H_{\alpha\alpha}(\vec{k})} + \sum_{\alpha\neq\beta} \frac{H_{n\alpha}(\vec{k})H_{\alpha\beta}(\vec{k})H_{\beta m}(\vec{k})}{[E-H_{\alpha\alpha}(\vec{k})]\,[E-H_{\beta\beta}(\vec{k})]} + \ldots. \tag{2}$$

where n and m belong to our small set of interesting levels; α and β are all the energy levels outside the selected set. The model Hamiltonian will be used only over a finite range of energies; hence we can replace E in eq.(2) by an average energy $\bar{E}$ with negligible error. Note that the symmetry transformation properties of $H_{nm}(\vec{k})$ are also obeyed by $U(\vec{k},\bar{E})$. Making a polynomial expansion of U in terms of the components $\vec{k}-\vec{K}$, it is easy to see that the nth term has no contribution to lower order than n. The polynomials we use are basis functions for product representations of the group of $\vec{K}$. It is possible to reorder the expansion (2) in the following way

$$U_{nm}(\vec{k},\bar{E}) = \sum_{\alpha ij} A_{nm}^{\alpha ij}(\bar{E})\; P_{\alpha ij}(\vec{k}-\vec{K}) \tag{3}$$

where $P_{\alpha ij}(k)$ is a polynomial belonging to the *i*th row of the *j*th irreducible representation α of the product group of $\vec{K}$. The coefficients A are determined by a general form of the Wigner-Eckart theorem. They can be written as a product of a generalized Clebsch-Gordon coefficient and a reduced matrix element. Equation (3) can now be used to construct model Hamiltonians. We simply use the reduced matrix elements as energy-independent adjustable parameters. The series in equation (3) can be truncated at some order of $(\vec{k}-\vec{K})$.

Fitting procedure

The dimensions of the effective Hamiltonian matrices are equal to the number of bands involved at the high symmetry points. Also the number of bands included in the fit depends on the energy range of interest. Here the band structure is fit close to E_F, so the Fermi surface and related phenomena can be computed.

Löwdin perturbation is used in deriving the model Hamiltonian scheme; this assumes that bands can be separated into two groups: near and far from E_F. To satisfy this criteria completely in our A-15 bands is sometimes difficult; all bands are situated close to each other. Table 2.2 gives the cutoff energies of the bands at the high symmetry points. The energy gap at Γ and R is relatively large in the vicinity of E_F, however at X one is forced to cut somewhere. It is done between X_1(0.607 Ry) and X_4(0.613 Ry). This is done since it is desirable to have the same number of bands fitted throughout the Brillouin zone. A group symmetry as well a cutoff problem is the Z_2 level coming from X_4(0.613 Ry). A careful examination of figure 2.4 page 35 shows that this Z_2 level diminishes in energy as $\vec{k}$ goes from X to M. Meanwhile a Z_3 rises from 0.607 to 0.690 Ry. This last level should be included in the Hamiltonian, because it comes close to E_F at M. Thus the Z_3 instead of the Z_2 level has to be included. Continuing this procedure and taking into account the doublet properties of every X level, brings us to the bottom of the *sp* band some 0.3 Ry below E_F. To avoid this, we fit the lower part (near X) of the aformentioned Z_3 level as if it were a Z_2. At M the upper cutoff is made above M because this state drops rapidly along the T line down to the R_4 level which is in the vicinity

TABLE 2.2 Energy levels and size parameters at the four high symmetry points of Nb_3Sn (energies in Rydberg)

	Γ	X	M	R
lower energy gap	.059	.006	.060	.094
Valence band	.651-$\Gamma_{25'}$ .683-Γ_{12}	.613-X_4 .632-X_2 .660-X_1	.690-M_9 .698-M_{10} .702-M_2 .720-M_8	.681-R_1,R_2
conduction band		.790-X_1	.723-M_9 .741-M_6 .743-M_3 .761-M_1 .782-M_5	.690-R_4
upper energy gap	.179	.044	.048	.167
size of model Hamiltonian	5x5	6x6 2x2	12x12	10x10
local validaty region in π/a units	.90	.56	.50	.71
number of parameters	49	62	90	64
number of APW-$\vec{k}$ points	110	82	63	62

of E_F. It is impossible to reduce the number of bands considered at M, because on the lower site of the energy scale all bands cut the Fermi level. On the higher site, the M_5 level also crosses the Fermi energy (only in the case of Nb_3Sb). Appendix A gives the model Hamiltonians.

The APW bands which have been calculated at 286 $\vec{k}$ points in the irreducible wedge (1/48 th) of the Brillouin zone (a $\pi/10a$ mesh) are now used as input to the fitting procedure. For each of the high symmetry points $\vec{K}_i$ the $\vec{k}$ points were ordered in increasing distance to $\vec{K}_i$. We then determine the parameters in such a way that they gave the best approximation to the energy values of the first n points (see table 2.2). This minimalisation procedure is done by using the Marquardt algorithm[9].

One can hope to get better fits by concentrating all effort at E_F, the Fermi Energy. This idea is tested by introducing weight factors $\exp\{-\gamma[E_F-E(\vec{k})]^2\}$ to the APW bands. One obtains a better fit of the energy bands close to E_F, so the Fermi surface will look more like *ab initio* Fermi surface. Using this procedure, one loses accuracy in the lower and upper end of the fitted energy region, however this effect is of minor interest.

Another way used to improve accuracy is to extend the matrix elements to higher order polynomials. For the readers interest, a list of the number of adjustable parameters per order is given in Appendix A. The initial intention was to go up to fourth order in $\vec{k}-\vec{K}_i$ for $\vec{K}_i$ equal X, M and R. However at the M point the number of parameters would be over a hundred, due to low symmetry (16 operands) and the large number of bands involved. For the Γ point the interest is different, we want to have the Nb_3Sn Fermi surface (coming from the Γ_{12} level) all to be in the Γ sphere of influence. So the sphere radius is chosen large (.90 π/a). In order to achieve the same accuracy of 1 mRy it is necessary to use a fit of order 10.

The model Hamiltonians about the four high symmetry points are considered separately. In order to use our scheme we need, of course, to be able to move smoothly throughout the Brillouin zone. We use a Gaussian interpolation for combining the local fits: the Gaussian function cuts off the expansions faster than the exponentially growing errors. The partial fits are combined to one global fit in the following way

$$E_n(\vec{k}) = \frac{\Sigma_{\vec{k}} \exp[-\alpha(\vec{k}-\vec{K})^2/r^2(\vec{K})].E_n(\vec{K},\vec{k})}{\Sigma_{\vec{k}} \exp[-\alpha(\vec{k}-\vec{K})^2/r^2(\vec{K})]} \qquad (4)$$

where $r(\vec{K})$ is the local validity region and α is the freely chosen crossing rate. After some experimentation we found that spherical weight factors as in equation (4) are not sufficient; because the Γ fit gets too much weight in the interior of the Brillouin zone. This problem is solved by substracting a non-spherical factor

$$\exp[\beta k_x^2 k_y^2 k_z^2]. \tag{5}$$

For an easy application of the fit it is desirable to have the same number of bands fitted throughout the Brillouin zone. Since the dimension of the Hamiltonian at M is twelve and there are no other bands of interest at M, we fix the total number of bands fitted to that number. As a consequence we need to introduce additional bands into the other local Hamiltonians. This is facilitated through an extension of the dimensions everywhere to twelve by adding diagonal elements, while fixing the additional off-diagonal elements to zero. The new diagonal elements are parameterized polynomials up to the fourth order, except the first conduction band at the X point, which is represented as a full $X_1 \times X_1$ block.

Discussion

Figure 2.6 shows the $\vec{k}.\vec{p}$ fitted band structure of Nb_3Sn. This band structure has the same scale as the APW energy bands shown in figure 1 on page 56. Notice that the $\vec{k}.\vec{p}$ fit has some discontinuities in slope about the middle of the high symmetry lines. These discontinuities arise from the Gaussian combining functions. The crossing rate α is chosen big to make the transition range small, so connection mistakes are excluded. Having a short transition range, one introduces steep bands if they are not matched perfectly together.

On comparing figure 2.6 with figure 1, it is clear that some bands are missing in the former. At M the levels M_5 (0.631 Ry) and M_9 (0.805 Ry) are not present. These levels are not included in the $\vec{k}.\vec{p}$ fit set. So a density of states calculation using the $\vec{k}.\vec{p}$ fits, between 0.631 and 0.805 Ry, will only gives a complete density.

The band structure is presented along the high symmetry lines using the fits. Along these lines many of the $\vec{k}.\vec{p}$ adjustable parameters have no influence on the result, since many polynomials are zero due to symmetry. Thus, there are less parameters available for fitting the band structure, so the fit along the high symmetry lines will be less

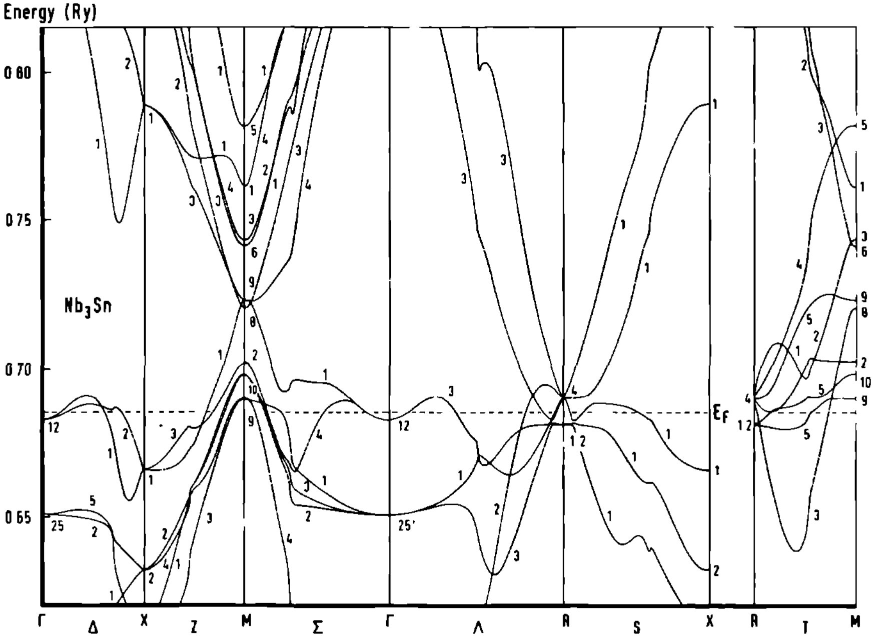

Figure 2.6

The $\vec{k}.\vec{p}$ derived electronic band structure of Nb$_3$Sn near E_F

accurate than inside the Brillouin zone. The advantage of showing bands along the high symmetry lines is first of all the relative simplicity for understanding the origin of the different phenomena and second the possibility of talking about bands using their symmetry labels. Here we are able to show the main properties of the generalized $\vec{k}.\vec{p}$ fit scheme; preserving symmetry and degeneracy of the energy bands. Band crossings are fitted correct.

At most places inside the Brillouin zone there is no symmetry present, so every introduced parameter is significant. This is helpful since the $\vec{k}$ point with the biggest distances to the four corners $\vec{K}_i$ of the tetrahedron, the Brillouin zone, is in the center of the zone. This $\vec{k}$ point and those in its environment are the worst fit, because of their large distances to the expansion points $\vec{K}_i$. Calculations of the error spectrum of these points confirm this idea. The error in this neighborhood is about 3 mRy compared to an overall error 1 mRy. This error is too big using the $\vec{k}.\vec{p}$ directly in the determination of the Fermi surfaces which have pieces in the center of the zone. For example band 20 of figure 3.2 in chapter III. There we discuss the solution of this problem.

Table 2.3 gives a list of the root mean square (RMS) errors as function of $|E_{\vec{k}} - E_F|$. This function is a monotonically increasing function, since we applied the weight factors $\exp\{-\gamma(E_F - E_{\vec{k}})^2\}$. Since the shift of the Fermi energy, for getting optimal correspondence to experimental data, will not be more than 5 mRy, energy levels closer than 10 mRy away from the preliminary Fermi level are of interest. The overall $\vec{k}.\vec{p}$ RMS error is put to 1 mRy for Nb_3Sn; that of Nb_3Sb fit is somewhat smaller (0.7 mRy). This small error reflects the fact that most of the energy levels fitted are situated close to M or R, where the fit is better than overall.

Parallel to Jansen and Mueller[7], Birman, Lee and Berenson[8] developed the $\vec{k}.\vec{p}$ effective Hamiltonian, by the same reformulation of the $\vec{k}.\vec{p}$ method. They applied this scheme to the A-15 crystal structure[10]. As explained in the theory section the $\vec{k}.\vec{p}$ model Hamiltonian is obtained through Löwdin perturbation. So a well defined set of energy levels is required to construct the Hamiltonian. In the band structure of Nb_3Sn (figure 2.6) a R_1,R_2 and a R_4 level are situated close to each

TABLE 2.3 Root mean square error of the $\vec{k}.\vec{p}$ fits as function of energy range

range $\lvert E_{\vec{k}}-E_F \rvert \leq E_r$ (in mRy)	rms error (in mRy) Nb_3Sn	 Nb_3Sb
10.	0.9	0.7
20.	1.1	0.9
30.	1.2	1.7
40.	2.5	2.2
50.	2.6	2.5

other. This situation is common to many A-15 band structures [5,11]. Only taking the R_4 level into account in the $\vec{k}.\vec{p}$ model Hamiltonian basis is insufficient; one will exclude the non-negligible interaction between the two levels. Lee *et al.*[10] constructed an effective Hamiltonian which included only the R_4 level. This restriction will have severe consequences on the fit of the R_4 level; the Fermi surface will differ from that calculated via *ab initio* means. Another shortcoming in Lee's effective Hamiltonian arises from the simple polynomials for the R_4 bands. Their polynomials, up to quadratic order, can never describe the *ab initio* behavior of the bands. They have to fit the hybridization between R_1, R_2 and R_4 levels with quadratic terms; in this they will fail.

In conclusion we can say that the generalized $\vec{k}.\vec{p}$ method forms a convenient and simple means to interpolate electronic and phononic structure. The combination of partial fits into one global fit is simple. With the global fit we have a powerful tool which produces the A-15 electronic bands ten thousand times faster than an *ab initio* APW program. Unfortunately one requires the APW band structure on a sufficiently fine mesh to determine the $\vec{k}.\vec{p}$ fit parameters accurately.

References

1 See, for example, J.Callaway,*Quantum Theory of Solids* (Academic Press,New York,1974), Parts A and B and references therein

2 E.O.Kane,in *Semi-conductors and Semi-metals*, edited by R.K. Willardson and A.C.Beer (Academic Press,New York,1966),Vol.1

3 L.F.Mattheiss,Phys.Rev.B12,2161 (1975)

4 M.Weger and I.B.Goldberg,in *Solid State Physics*,edited by H. Ehrenreich,F.Seitz and D.Turnbull (Academic Press,New York,1973), Vol.28

5 W.E.Pickett,K.M.Ho and M.L.Cohen,Phys.Rev.B19,1734 (1979)

6 T.Jarlborg,thesis,Chalmers University of Technology,Göteborg (1978) *unpublished*

7 H.J.F.Jansen and F.M.Mueller,Phys.Rev.B20,1426 (1979)

8 J.L.Birman,T-K Lee and R.Berenson,Phys.Rev.B14,318 (1976)

9 D.W.Marquardt,J.Appl.Math.11,431 (1963)

10 T-K Lee,J.L.Birman and S.J.Williamson,Phys.Rev.Lett.39,839 (1977)

11 B.M.Klein,L.L.Boyer,D.A.Papaconstantopoulos and L.F.Mattheiss,Phys. Rev.B18,6411 (1978)

Several physical quantities can be obtained through the evaluation of an integral over the Brillouin zone. Examples are density of states, magnetic susceptibility, Fermi velocities and other related transport quantities. The most simple way to evaluate this type of integral is by using the Monte Carlo or an uniform point sampling method. These methods sum over a large number of random or uniform $\vec{k}$ points. There is a big influence of statistical noise involved,so a large number of random (uniform) points are necessary in order to achieve accurate enough results. Despite this problem the transport quantities in section "Applied Superconductivity" of chapter III are calculated by applying the Monte Carlo method. 50,000 random points in the irreducible wedge of the Brillouin zone (1/48th) were calculated. The number of necessary $\vec{k}$ points can be reduced if a proper interpolation scheme is applied. Lehman *et al.*[1] developed a linear interpolation expression for Brillouin zone integrations like the density of states. The use of higher than linear interpolation expressions for $E(\vec{k})$, like in the QUAD method (e.g. Mueller *et al.*[2]) is also possible. We chose the linear interpolation scheme applied to tetrahedrons, because we believe that this method will reproduce the van Hove singularities in the density of states from expressions, which can be written analytically, through less computational effort.

The treatment of Lehmann *et al.*[1] reformulated by Lehmann and Taut starts from the fact that the coefficients of the linear interpolation expression in a tetrahedron are determined uniquely by the values of $E(\vec{k})$ at the corners of the tetrahedron. In this way a continuous interpolation over the total Brillouin zone is obtained and in addition, there are no boundary effects. Moreover, the resulting formulae are very handy. The method can be applied to physical quantities which need an evaluation of integrals of type

$$\int_{E(\vec{k})=E} \frac{dS}{|E(\vec{k})|} A(\vec{k}) \tag{1}$$

where the integration has to be performed over constant energy surfaces.

$A(\vec{k})$ can be any $\vec{k}$ dependent function (continuous or discontinuous). The density of states has a formulation like equation (1), namely

$$N(E) = \frac{1}{4\pi^3} \int_{E(\vec{k})=E} \frac{dS}{|\vec{\nabla}E(\vec{K})|} \tag{2}$$

$A(\vec{k})$ is here the unity.

The techniques of the tetrahedron method applied to the density of states function are as follows. First the Brillouin zone is subdivided in a large number of tetrahedrons, with an arbitrary shape and volume. In the case of a cubic Brillouin zone one is able to make identical tetrahedrons. The energy bands are then calculated on the corners of every tetrahedron. Per tetrahedron and per band the energies are ordered according to their magnitude, so that $E_0 \leq E_1 \leq E_2 \leq E_3$. These energy values are used to define a linear interpolation inside the tetrahedron. The contribution to the density of states of this tetrahedron, which is equal to the cross section of the plan $E(\vec{k})=E$ with the tetrahedron, may be written as a sum of triangular areas. The surface depends on the relative position of E to the corner energies. Table 2.4 lists these contributions. Ω_t is the volume of the tetrahedron.

For our density of states calculations we subdivided the irreducible wedge of the Brillouin zone, which itself is a tetrahedron, in 3375 identical tetrahedrons; this is equivalent to a $\pi/15a$ mesh on corners. The total number of different corners, where the $\vec{k}.\vec{p}$ bands have to be calculated, is for this subdivision 816. This number is very small compared to the 50,000 points of the Monte Carlo method.

References

1 G.Lehmann, P.Rennert, M.Taut and H.Wonn, Phys Status Solidi 37, K27 (1970)

2 F.M.Mueller, J.W.Garland, M.H.Cohen and K.H.Bennemann, Ann.Phys. 67, 19 (1971)

3 G.Lehmann and M.Taut, Phys Status Solidi 54, 469 (1972)

TABLE 2.4 Density of states contribution of an individual tetrahedron of which the corner energies are ordered $E_0 \le E_1 \le E_2 \le E_3$

E	$N_t(E)$
$E \le E_0$	0
$E_0 \le E \le E_1$	$\dfrac{3\Omega_t\ (E-E_0)^2}{(E_1-E_0)(E_2-E_0)(E_3-E_0)}$
$E_1 \le E \le E_2$	$\dfrac{3\Omega_t}{(E_1-E_0)}\left[\dfrac{(E-E_0)^2}{(E_2-E_0)(E_3-E_0)}+\dfrac{(E-E_1)^2}{(E_1-E_2)(E_3-E_1)}\right]$
$E_2 \le E \le E_3$	$\dfrac{3\Omega_t\ (E-E_3)^2}{(E_3-E_0)(E_3-E_1)(E_3-E_2)}$
$E_4 \le E$	0

Along with V_3Si, the isoelectronic material, Nb_3Sn is the most thoroughly studied A-15 compound. This wide ranging interest is primarily due to the anomalous behavior of their physical properties, and started in 1954 with the discovery of a high superconducting transition temperature (T_c) of 17°K for V_3Si[1]. Later, anomalies were discovered[2] in their elastic constants, magnetic susceptibility and Knight shift. In addition, structural transitions have been observed. Although different crystals of Nb_3Sn and V_3Si show considerable similarities in their anomalous behavior, exact reproducibility has not been achieved. Workers in this field are constantly faced with accessing to what extent the data are sample dependent. Probably the most important non-reproducible behavior is the occurrence of the low temperature (45°K and 21°K for Nb_3Sn and V_3Si respectively structural transformation which has been called the Martensitic transformation. Chemical composition, crystallographic structure and long-range order are the most common criteria for characterizing the samples according to their Martensitic transformation and other listed properties.

Similarities[2] of Nb_3Sn and V_3Si include high T_c's (17-18°K), anomalous temperature dependences of many properties, very soft acoustic phonon modes, cubic to tetragonal structural transformations and large stress dependences for some of their physical properties. The major differences are that the structural transformations are first-order for Nb_3Sn and second-order for V_3Si and that the tetragonal distortions are negative for Nb_3Sn and positive for V_3Si. Also a substantially larger softening of the acoustic mode (C_{44}) occurs in Nb_3Sn as compared to that of V_3Si.

Other A-15 compounds (i.e. the high T_c's Nb_3Al, Nb_3Ge and the low T_c Nb_3Sb) have become of experimental and theoretical interest more recently. Such homological investigations are important. A-15's with low T_c are useful for this tandem effort, since experimental difficulties are minimized compared to those encounted in high T_c materials. For example the properties which make things so interesting in Nb_3Sn, Martensitic transformation, high mass sheets of Fermi surface and flat band structures make this compound difficult to measure as well as to calculate. The situation is much simpler in Nb_3Sb. To be explicit, Nb_3Sn needs a magnetic field of more than 22 T (H_{c_2}) before it is in the normal state and de Haas-van Alphen experiments may be performed. Fields of such intensity are not readily available in most laboratories.

This chapter describes the band calculations and the derived physical quantities of Nb_3Sn. We describe the density of states, Fermi surface, band masses, Fermi velocity and anisotropy of H_{c_2}. Chapter IV describes our work done on Nb_3Sb, where we calculated density of states, Fermi surface and band masses. These last two properties have been extensively compared to a rather large wealth of data mainly derived from de Haas-van Alphen effect. These comparisons of Nb_3Sb lend greater credence to the less well experimentally documented results for Nb_3Sn.

Survey

The electronic band structure of Nb_3Sn is calculated along the lines outlined in chapter IIa. Figure 2.4 shows all the valence bands and the lowest conduction bands. The energy bands around the Fermi energy are of major physical importance because their occupation can be changed by the temperature, or by applying a magnetic or electric field. The lower lying valence bands are only of interest for the determination of the density of states and the Fermi energy (E_F). Figure 1 of the following reprint shows the Nb_3Sn bands near E_F. This picture is obtained through the evaluation of the APW matrix at 56 independent points in the irreducible 1/48th of the Brillouin zone (a $\pi/4a_0$ mesh). The $\vec{k}$ points of this set on the high symmetry lines are marked in figure 1. These calculated energies are interconnected by the use of the symmetry of the wave functions.

The energies of this set of 56 $\vec{k}$ points are fitted to 28 symmetrized Fourier terms ("stars"). The density of states is calculated by using this fit and the tetrahedron method, discussed in chapter IIc. The Brillouin zone is hereby subdivided in 1728 tetrahedrons. Figure 3.1 shows the resulting density of states function. The Fermi level

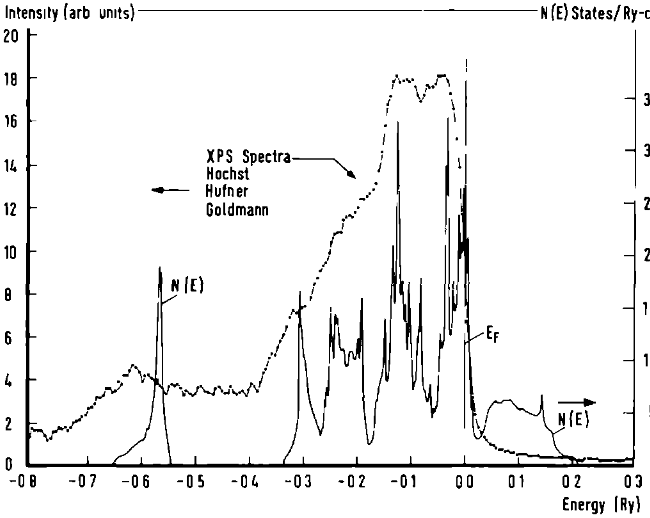

Figure 3.1 The electronic density of states of Nb_3Sn. The experimental data are those of ref.3 .

(0.6851 Ry) is obtained by integrating the differential density of states to 38 electrons (6 times 5 Nb and 2 times 4 Sn valence electrons). The zero of the energy scale is put at E_F. Table 1 of the following reprint lists the calculated and measured density of states at the Fermi level, $N(E_F)$. Our $N(E_F)$ may be compared with experimentally derived values. The experimental result as given in figure 3.1 is the XPS (X-ray photoelectron spectroscopy) spectrum of Höchst *et al.*[3]

The Fourier fit can be used for Brillouin zone integrations, but is not accurate to calculate $\vec{k}$ dependent quantities, such as the Fermi surface. This problem arises from the fact that Fourier fits have difficulties near band crossings. But the weight of high symmetry planes, where band crossings occur, is a set of measure zero compared with the bulk of the Brillouin zone. The Fermi surface shown in figure 3 of the first reprint is obtained by drawing contour lines between $\vec{k}$ points in the symmetry planes, for which the APW matrix is solved (on a $\pi/8a_0$ mesh). The four M centered ellipsodal pieces are fitted by M derived harmonics, up to eighth order. This polynomial fit is used for the calculation of the dHvA frequencies plotted in figure 2 of the second reprint.

Both fit schemes, the Fourier fit and harmonic fit, are not applicable to the entire Fermi surface of Nb_3Sn. The generalized $\vec{k}.\vec{p}$ scheme developed by Jansen and Mueller[4] is adapted to the A-15 crystal structure. Chapter IIb describes this method together with appendix A and the necessary quantities and matrices which can be extracted from them. This $\vec{k}.\vec{p}$ method reproduces the APW Fermi surface quite well (figure 3.2). The differences do not arise from shortcomings of the fit but rather from a data lack at the time the APW Fermi surface was drawn. Though the applied mesh band crossings were not always detectable; later APW calculations confirm the band crossings and the shapes found in the $\vec{k}.\vec{p}$ derived Fermi surface. This matter is discussed together with some band masses in a separate section.

The two density of states, one obtained from the Fourier fit and one from the $\vec{k}.\vec{p}$ fit, are discussed in the next section. Also discussed is the decomposition of the density of states into band by band contributions. Finally we, in collaboration with Dr.R.Blaschke, calculated some relevant superconducting parameters, such as plasma energy, Fermi velocity, London penetration depth and anisotropy of the upper critical field. These calculations are described in the last section of this Nb_3Sn chapter.

reprinted from
PHYSICAL REVIEW LETTERS
vol.41 (1978) 181-184

Electronic Structure of Nb_3Sn

A. T. van Kessel, H. W. Myron, and F. M. Mueller
Physics Laboratory and Research Institute for Materials, University of Nijmegen, Toernooiveld, Nijmegen, The Netherlands

(Received 13 December 1977)

The electronic band structure of Nb_3Sn has been calculated by means of the augmented-plane-wave method. Comparison with a variety of experimental data suggest that the band model is highly accurate.

Primarily because of its high superconducting critical temperature,[1] the A-15 material Nb_3Sn has continued to interest experimentalists and theorists. Recent interest has focused on a number of anomalous properties in the normal state. Theoretical models have been used to correlate or make these anomalous properties understandable. Many models have focused on point-group symmetry of selected points in the Brillouin zone (BZ), others have invoked the use of tight-binding schemes with a variety of couplings within or between the dominant Nb chains.[2] Clogston and Jaccarino[3] suggested that the temperature dependence of the susceptibility and the Knight shift in V-based A-15's could be understood by a narrow peak in the density of states, $N(E)$, close to the Fermi energy E_F.

In this Letter we report an *ab initio* calculation of the electronic structure, density of states, and Fermi surface of Nb_3Sn. Our technique and methodology is similar to the well-known work of Mattheiss.[4] Without adjustment, we find good agreement with a number of experiments including the temperature dependence of the susceptibility and a recent measurement of the de Haas-van Alphen (dHvA) effect.[5]

The crystal potential was constructed from overlapping neutral atomic charge densities and exchange was treated in Slater's ($\alpha = 1$) local approximation, this technique, the "Mattheiss prescription," has produced good agreement with self-consistent local density exchange calculations in Nb.[5] Since the linear chains distort severely the spherical symmetry about the Nb sites, we have incorporated nonspherical corrections inside the MT's (muffin-tin potential). The interstitial potential deviations from a constant MT floor were incorporated as Fourier terms.[7] We have found that the contours of potential were similar to a potential constructed from the experimental charge density,[8] if appropriate cores were added.

A length ordered basis of more than 300 augmented plane waves (APW) was used to form the secular matrix Using our potential, tests showed that all bands were converged to better than 3 mRy. Globally, the resultant band structure of Nb_3Sn was the same as that of Ref. 4 and compared equally well with XPS (x-ray photoelectron spectroscopy) data.[9] Microscopically it differed in that the Γ_{12} level (intersecting E_F) has dropped by approximately 30 mRy relative to a host of levels at M. In Fig. 1 is given the band structure in the immediate vicinity of the Fermi level, showing multiple hole structure at the point M and an intersection of the flat bands associated with Γ_{12} symmetry.

The band structure for the lowest 24 bands was found at 56 equally spaced independent points in the irreducible $\frac{1}{48}$th of the BZ. The structure was fitted to 28 symmetrized Fourier terms ("stars") and the density of states was calculated by a linear gradient method using 1728 tetrahedrons in the irreducible BZ. In Table I are listed (bare) values of the experimentally derived $N(E_F)$'s. Our results are fortuitously close to Junod's specific-heat value.[10] NMR-derived[11] results give similar agreement.

We have used $N(E)$ near E_F to calculate the temperature dependence of the Pauli contribution to the susceptibility, which depends on the derivatives of $N(E)$. Linear interpolation was applied between a $N(E)$ grid spaced by 1.25 mRy. The Fermi level was calculated at every temperature by a self-consistent procedure, it varied by more than 4 mRy nonmonotonically as T varied between 0 and 300 K. In Fig. 2 is given the temperature dependence of the susceptibility χ of Rehwald *et al.*[12] The relationship between χ and the martensitic phase transformation has recently been considered,[13] using parametrized Hamiltonians and the group symmetries of special points in the zone. Most previous discussions of $\chi(T)$ have relied on the model of Ref. 3 which utilized a large orbital contribution to explain the anomalous temperature dependence of the Knight shift. Recently,[8] it was found that in forming the related compound V_3Si, approximately two electrons transfer from each Si site to the V chains. This removes the necessity of a large

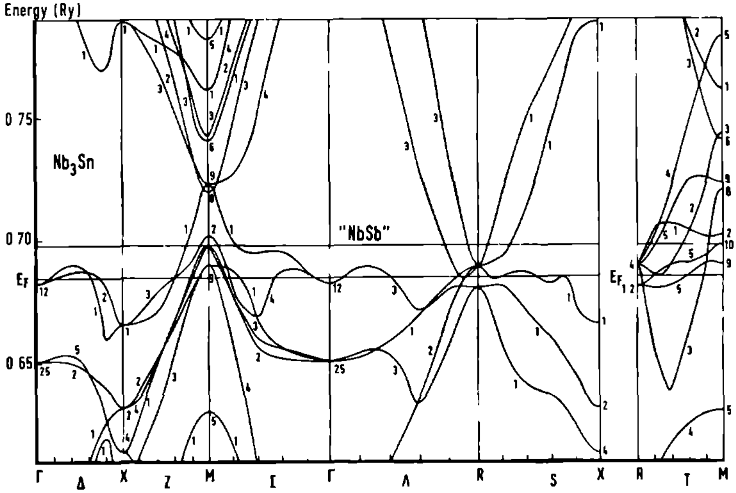

FIG 1. The band structure of Nb_3Sn near E_F The dashed line is E_F appropriate to Nb_3Sb.

orbital term. We plan to return to this important point. We find that by applying a constant enhancement[14] of $3.69 S = \chi/\chi_0 \equiv 1/(1-\mu)$, the temperature dependence of the susceptibility is consistent with a Pauli term, where $\chi_0 = \mu_B{}^2 N(E_F)$, shown in Fig. 2 as the dashed curve.

For purposes of comparison, we consider an enlarged cell of six atoms of pure bcc Nb. Taking data from McMillan[15] ($\chi = 514$ and $\gamma = 269$ in states/Ry "cell"), and using $\lambda = 0.82$ we find a pure Nb Stoner factor of $(1+\lambda)\chi/\gamma$ or 3.38. Deriving an effective exchange interaction[14] per Nb site from $I = 12(1-1/S)N(E_F)$, we find 0.79 eV for bcc Nb compared with a value of 0.49 eV for Nb in Nb_3Sn. This difference reflects two competing effects (1) The Nb-Nb nearest-neighbor distance is 7.3% smaller in Nb_3Sn (2.65 Å) than in bcc Nb (2.86 Å), (2) the number of nearest neighbors is far less in Nb_3Sn (2) than in bcc Nb (8). The second effect dominates the first.

Using these results we find estimates of μ^*, the Coulomb pseudopotential[15, 16] of Morel and

TABLE I. Comparisons of $N(E_F)$ and results.

$N(E_F)$	Density of states	This work	249 states/Ry cell	
N_s	NMR	Fradin *et al.*[a]	264 states/Ry cell	
γ_0	Specific heat	Junod[b] $\gamma/(1+\lambda)$	240 states/Ry cell	
χ	Susceptibility (extrapolated)	Rehwald *et al.*[c]	896 states/Ry cell	
			Nb_3Sn	Nb
S	Stoner factor	χ/χ_0	3.69	3 48
I	Exchange interaction per Nb atom-spin	$12\mu/N(E_F)$	0.49 eV	0 79 eV
μ^*	Coulomb pseudo-potential		0.25	0.19

[a] Ref. 11. [b] Ref. 10 [c] Ref 12

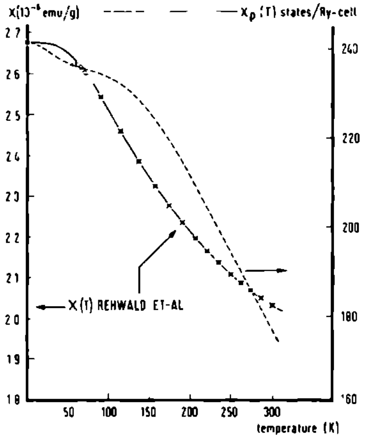

FIG. 2. The temperature dependence of the susceptibility of Nb_3Sn. The circles are the data of Rehwald *et al.* (Ref. 12) taken in the tetragonal phase, the crosses in the cubic phase, and the solid line their extrapolation function (left-band scale). Note that both left- and right-hand scales share a common zero.

Anderson,

$$\mu^* = \frac{\mu}{1 + \mu \ln(E_B/\omega_0)}, \qquad (1)$$

of 0.18 and 0.25 for Nb and Nb_3Sn, respectively. We have assumed that $\omega_0 = \omega_D/1.2$ and have used the values of 0.11 Ry[9] and 0.02 Ry (Fig. 1) for the band width E_B (near E_F), and the values[10,15] of 277 and 227' for ω_D, for Nb and Nb_3Sn, respectively.

In Fig. 3 we present the Fermi surface of Nb_3Sn (intersecting bands 15–21) in the principal symmetry planes. Because of the sensitivity of small energy shifts (especially bands 19 and 20) we have used the APW secular itself as an "interpolation scheme." Two features are noteworthy compared to the previous V_3Si isoelectronic Fermi surface[4] (1) the greater confluence of osculated structure at M, and (2) the flat "boxlike" structures centered at Γ. A microscopic test of band structure near E_F is provided by the dHvA effect. Recently Arko *et al.*[5] found dHvA oscillations in Nb_3Sn single crystals using 400-kG pulsed fields. Within their accuracy and insensitivity to small pieces we find that the rich structure exhibited in Fig. 3 is consistent and can be used to interpret their data (the M-centered pieces).

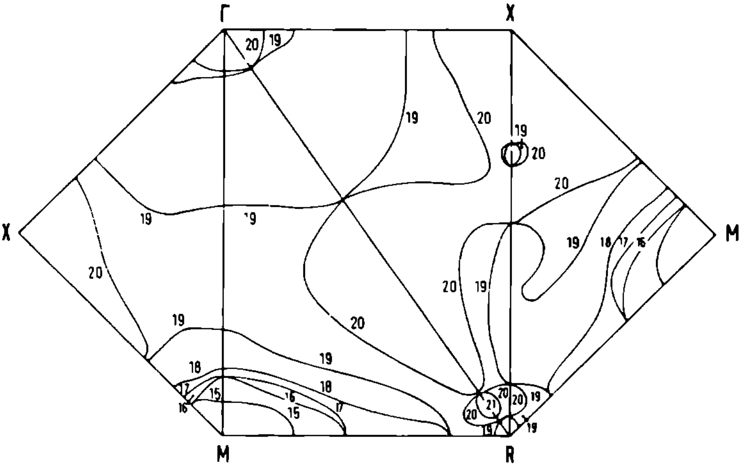

FIG. 3. The Fermi surface of Nb_3Sn. The band indexing follows Ref. 5. The positions of the labels follows the filling of $\vec{k}$ space volumes so that band 20 near Γ is an electron piece and band 15 near M is a hole piece.

Other band models[17] show frequencies with neither the correct magnitude nor angular variation. The pieces at M have band masses ranging from 0.23 to 1.03m_e, those centered at Γ, 2 to 3, and those at R, 0.2. Our R-centered pieces have dHvA frequencies smaller than any seen.[5] The high mass of the Γ-centered pieces inhibits observation in the dHvA effect. Samoilov and Weger[18] have reported structure in V_3Si, using positron annihilation, in the [100] direction at 0.2, 0.6, and 0.8 π/a units. The intersections of the "flat" sheets along Γ-X are 0.15 and 0.64 π/a units in good agreement with the first pieces of structure. The twentieth band near X and surrounding the X-R line is a possible candidate for the third structure.

We conclude that our results compare well with available experimental data. In addition, the intersections of E_F for pseudo Nb_3Sb (shown in Fig. 1) are in quantitative agreement with dHvA data.[19]

This work was supported as part of the research program of the Sticting voor Fundamental Onderzoek der Materie with financial support from the Nederlandse Organisatie voor Zuiver Wetenschappelijk Onderzoek.

---

[1] G. F. Hardy and J. K. Hulm, Phys. Rev. 93, 1004 (1954); S. Geller and B. T. Matthias, J. Am. Chem. Soc. 77, 1502 (1955); see also *Superconductivity in d- and f-Band Metals*, edited by D. H. Douglass (Plenum, New York, 1976).

[2] M. Weger and I. B. Goldberg, in *Solid State Physics*, edited by H. Ehrenreich, F. Seitz, and D. Turnbull (Academic, New York, 1973), Vol. 23, and references therein.

[3] A. M. Clogston and V. Jaccarino, Phys. Rev. 121, 1357 (1961).

[4] L. F. Mattheiss, Phys. Rev. B 12, 2161 (1975).

[5] A. J. Arko *et al.*, Phys. Rev. Lett. 40, 1590 (1978).

[6] N. Flyashar and D. D. Koelling, Phys. Rev. B 15, 3620 (1977), and references therein.

[7] P. D. De Cicco, Phys. Rev. 153, 931 (1967).

[8] J. L. Staudenmann, P. Coppens, and J. Muller, Solid State Commun. 19, 29 (1976).

[9] H. Höchst, S. Hüfner, and A. Goldman, Solid State Commun. 19, 899 (1976).

[10] A. Jonod, thesis, Université de Genève, 1974 (unpublished); Jonod used McMillans value of $\lambda = 1.40$.

[11] F. Y. Fradin, G. S. Knapp, S. D. Bader, G. Cinader, and C. W. Kimball, Ref. 1, p. 297, used $\lambda = 1.17$.

[12] W. Rehwald, M. Rayl, R. W. Cohen, and G. D. Cody, Phys. Rev. B 6, 363 (1972).

[13] T. K. Lee, J. L. Birman, and J. Williamson, Phys. Rev. Lett. 39, 839 (1977).

[14] C. Herring, in *Magnetism*, edited by G. T. Rado and H. Suhl (Academic, New York, 1966), Vol. IV, p. 254.

[15] W. L. McMillan, Phys. Rev. 167, 331 (1967), and references therein.

[16] P. Morel and P. W. Anderson, Phys. Rev. 125, 1263 (1962).

[17] B. M. Klein *et al.*, Ferroelectrics 16, 299 (1977); T. Jarlborg and G. Arbman, J. Phys. F 6, 189 (1976); K. M. Ho *et al.*, to be published.

[18] S. Samoilov and M. Weger, Solid State Commun. 24, 821 (1977).

[19] A. J. Arko, Z. Fisk, and F. M. Mueller, Phys. Rev. B 16, 1387 (1977).

reprinted from
PHYSICAL REVIEW LETTERS
vol.40 (1978) 1590-1593

de Haas–van Alphen Effect in the High-T_c $A15$ Superconductors Nb_3Sn and V_3Si

A. J. Arko
Materials Science Division, Argonne National Laboratory, Argonne, Illinois 60439

and

D. H. Lowndes
Department of Physics, University of Oregon, Eugene, Oregon 97403, and Physics Laboratory, University of Nijmegen, Nijmegen, The Netherlands

and

F. A. Muller, L. W. Roeland, and J. Wolfrat
Natuurkundig Laboratorium, University of Amsterdam, Amsterdam, The Netherlands

and

A. T. van Kessel, H. W. Myron, and F. M. Mueller
Physics Laboratory, University of Nijmegen, Nijmegen, The Netherlands

and

G. W. Webb
Institute for Pure and Applied Sciences, University of California, San Diego, La Jolla, California 92093

(Received 25 January 1978)

de Haas–van Alphen (dHvA) oscillations have been observed in Nb_3Sn in the (110) plane and in V_3Si at two orientations using single crystals of high resistance ratio and magnetic fields in excess of H_{c2}. The dHvA frequency data for Nb_3Sn can be interpreted as a series of nested ellipsoids centered at M, as suggested by a recent high-precision calculation of the Nb_3Sn Fermi surface.

We present the first de Haas–van Alphen (dHvA) measurements of the Fermi surfaces of high-T_c $A15$ structure superconductors, with measurements for both Nb_3Sn and V_3Si. We compare the Nb_3Sn results to a recent band-structure calculation[1] and find good agreement. The upper critical fields, H_{c2}, are ~20 kOe lower than earlier measurements,[2] apparently due to the high-purity single crystals of Nb_3Sn and V_3Si used.

The current high level of interest in $A15$ materials is due to the recent and continuing discoveries of the coexistence of a variety of anomalous normal-state properties[3] at both high and low temperatures, with the highest-T_c materials showing the most puzzling behavior. It is widely felt that the underlying physical features leading to these unusual normal-state properties are also the cause of the high transition temperatures observed in many $A15$-structure materials. A variety of physical models ascribing special features to either the phonon or electron distributions have been invoked to explain the normal-state properties. Our results are a first step in providing a microscopic test of the various electronic models.

Unfortunately, the very properties which make the high-T_c $A15$'s such interesting materials had until now, combined to prevent dHvA measurements of the Fermi surface, the only prior dHvA measurements being the very recent results of Arko, Fisk, and Mueller[4] for Nb_3Sb ($T_c \sim 0.2$ K). Magnetothermal oscillations were previously observed in V_3Ge.[5] The main limiting experimental factors are the following (1) Effective masses are expected to be high because of the intrinsically flat electronic band structure and because of the strong electron-phonon coupling ($\lambda \sim 1.4$ for Nb_3Sn). (2) H_{c2} is large, so that exceptionally high magnetic fields are needed simply to reach the normal state. (3) The materials tend to have high residual (and intrinsic) resistivities[6] so that T_D, the Dingle temperature, would be expected to be large. (4) Some of the most interesting materials undergo a martensitic transformation so that the dHvA signal is suppressed due to interference of oscillations and to phase smearing between tetragonally distorted subdomains.

The Nb_3Sn crystals were grown over a period of four months by closed-tube vapor transport with iodine as the transporting agent. X-ray diffraction on part of the deposit showed only sharp lines of the *A*15 structure with a room-temperature lattice parameter of 5.290 Å. An inductive measurement of the actual dHvA crystal showed a T_c (midpoint) of 17.8 K and a width (10%–90%) of 0.07 K. Resistivity measurements confirm that the samples undergo a martensitic transformation at 51 K. We estimate that $R(300\ \mathrm{K})/R(0\ \mathrm{K}) = 50$ assuming that T^2 is a satisfactory extrapolation function.[6,7] The V$_3$Si specimen was grown using a floating-molten-zone technique with induction heating in a pure-argon atmosphere. No resistance ratio or T_c measurements were made. However, from the amplitude of the dHvA signals we estimate the purity to be at least comparable to that of Nb$_3$Sn

Oriented single-crystal samples were mounted in a spiral-gear-driven rotator. The accuracy with which orientations are known in the (110) plane is estimated to be about 1 .

The experiments were conducted in the 400-kOe "slow-pulsed-field" facility at the University of Amsterdam.[8] The principal advantage of a slow magnetic field pulse is that self-heating and signal-detection problems associated with eddy currents in metallic samples are avoided and mechanical vibrational noise is minimized All dHvA data were taken in the free-inductive-decay mode from 400 kOe in order to eliminate electrical noise introduced through the current-regulating circuits. The entire system was checked by observing dHvA oscillations in a single crystal of Mg, the results agreed with published values of Mg dHvA frequencies to within 1–3%.

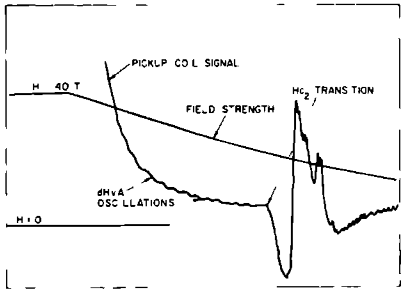

FIG. 1. Dual traces of a typical high-speed chart recording for Nb$_3$Sn at 75° from [100] showing the decay of a 40-T magnetic field pulse and the simultaneous recording of dHvA oscillations followed by the superconducting transition at H_c vs time (the field decays from 40 T to H_{c2} in about 0.15 sec) The apparent oscillations below H_{c2} are noise generated in the pickup coil in the superconducting state due to eddy currents, flux jumps, etc., and are *not* periodic in $1/H$.

The output of a compensated dHvA pickup coil was differentiated twice, filtered to take out some of the slowly varying voltage resulting from incomplete coil compensation, amplified, and displayed directly on the recorder. A typical recorder tracing is shown in Fig. 1. Since the induced voltage in the dHvA pickup coil is directly proportional to the time frequency of the dHvA oscillations, the usual exponential amplitude increase as H increases will not be observed due to the $1/H$ periodicity of the dHvA oscillations. For low-mass, low-frequency oscillations one may even see an amplitude decrease, which is further accentuated by the dc filter. This decrease in amplitude is clearly evident in Fig. 1.

The dHvA oscillations were analyzed by marking the positions of successive oscillation peaks and making a plot of oscillation number versus $1/H$, the slope of this "number plot" gives the dHvA frequency directly and was generally found to be a good straight line, giving us confidence in our field calibration. Beat structure, while obviously present at some orientations, was difficult to resolve because of the few oscillations

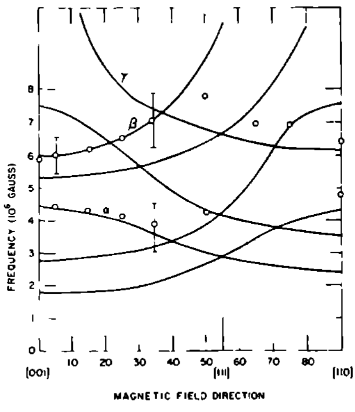

FIG. 2. dHvA frequencies for Nb$_3$Sn in the (110) plane. The solid circles (with typical error bars) are the experimental results. The solid lines are generated from the Fermi-surface model and band-structure calculation of Ref. 1

plus the above-mentioned problems with the amplitude dependence. Nevertheless, it is possible to resolve several separate branches in the Nb_3Sn data. Figure 2 displays the dHvA frequencies (open circles) found for Nb_3Sn in the (110) plane, while the limited data for V_3Si are given in Table I. The long cooling time of the magnet (~4 h after each pulse) made it necessary to space data at only 10 intervals. The typical error estimates indicated in Fig. 2 are conservative, based on a maximum possible counting error of one-half oscillation. The reproducibility of the dHvA frequency measurements at a given orientation was a few percent. There was evidence in the raw data for additional dHvA frequencies, both larger and smaller than those presented in Fig. 2. However, the signal-to-noise ratio for these oscillations is barely greater than 1, so they are not included here.

To interpret our results we have used the band calculation of Ref. 1. The calculation is similar to that of Mattheiss[9] (i.e., augmented-plane-wave method used with a *non*-self-consistent overlapping charge-density model, and Slater $\alpha = 1$ exchange) except that non-muffin-tin terms were included, and much greater precision was maintained throughout (i.e., 56 points in $\frac{1}{48}$th of the zone versus Mattheiss's 4, 3-mRy convergence versus 30 mRy, etc.). The solid lines in Fig. 2 are the predicted theoretical frequencies from Ref. 1. The correspondence between the observed frequencies and those labeled α, β, and γ is good. Based on this we conclude that the observed frequencies are consistent with a set of nested ellipsoids at M, similar to the observations in Nb_3Sb[5] and V_3Ge.[8,9] (This conclusion is not reached from the data alone.) Since very low dHvA frequencies are discriminated against in pulsed-field experiments as discussed above, it is reasonable that we do not observe the (low-mass) lowest predicted branches in Fig. 2. Other larger "missing" orbits have too high a mass ($m_{\mathrm{exp}}^* \sim 2.4 m_{\mathrm{band}}$) to be observed with this relatively insensitive technique. Further, the frequencies bunched near 5×10^6 G are too closely spaced to allow a clear resolution of beats. Within these limitations there is excellent agreement between our data and the predictions of the theory of Ref. 1. While the symmetry of the experimental frequencies is ambiguous, the magnitude is not. Several other band calculations[3,9,10] predict surfaces too large to fit our data, although it was pointed out that the size of small pieces is quite sensitive to the exchange approximation.[10]

TABLE I. dHvA frequencies for V_3Si.

Orientation	Frequency (10^6 G)
[100]	6.24
	4.60
[110]	7.78

We have indirectly and simultaneously measured the anisotropy of the upper critical field H_{c2} for Nb_3Sn at the same 10° intervals. Taking the highest-field point of the normal-to-superconducting transition (H decreasing) as defining H_{c2}, we find that $H_{c2} \approx 214$ kOe (at $T = 1.5$ K) and is isotropic within the 1% precision of our measurements. (For V_3Si we find $H_{c2} = 216$ kOe at $T = 1.5$ K.) This result is significantly smaller than the earlier (extrapolated) value of 240 kOe at $T = 0$ or $H_{c2} = 235$ kOe at $T = 1.5$ K. We have ruled out that this difference is due to extrinsic effects. Instead, we believe that the lower H_{c2} is intrinsic to the highly perfect (and well annealed) single crystals used. Evidence to support this comes from the fact that a poorer Nb_3Sn specimen, which gave only weak lower-frequency dHvA oscillations, had a higher critical field ($H_{c2} \sim 230$ kOe along [100]) and also displayed some slight anisotropy of H_{c2} (slightly lower values elsewhere), consistent with literature values.[2]

A significant concern for future dHvA experiments on Nb_3Sn may turn out to be the effect of thermally cycling a single crystal through the structural transformation. Repeated thermal cycling decreased the dHvA amplitudes by at least a factor of 2. These were restored by annealing at 700 C for five days. Our data do not yet allow us to determine which factor (high T_D, phase smearing, changes in electronic structure) is primarily responsible for the signal degradation. The change in the lattice parameter accompanying the transformation is only of order 1% so that a major change in the band structure is not expected. It does seem, however, that it may be possible to use the dHvA effect as a detailed probe of the electronic consequences of the $A15$ structural transformation and defect formation.

We acknowledge the help provided by Dr. Sven Hornfeldt in connection with the sample rotator design, and by Mr. Weizenbeek in connection with data logging. This work was supported by the U. S. Department of Energy, the National

Science Foundation, the Stichting voor Fundamenteel Onderzoek der Materie (The Netherlands), and the National Aeronautics and Space Administration.

---

[1] A. T. van Kessel, H. W. Myron, and F. M. Mueller, to be published.

[2] S. Foner and E. J. McNiff, Jr., Phys. Lett. 58A, 318 (1976).

[3] For a review see M. Weger and I. B. Goldberg, in *Solid State Physics*, edited by H. Ehrenreich, F. Seitz, and D. Turnbull (Academic, New York, 1973), Vol. 28; L. R. Testardi, in *Physical Acoustics*, edited by W. P. Mason and R. N. Thurston (Academic, New York, 1973), Vol. 10.

[4] A. J. Arko, Z. Fisk, and F. M. Mueller, Phys. Rev. B 16, 1387 (1977).

[5] J. E. Graebner and J. E. Kunzler, J. Low Temp. Phys. 1, 443 (1969).

[6] See, for example, Z. Fisk and G. W. Webb, Phys. Rev. Lett. 36, 1084 (1976); and D. W. Woodard and G. D. Cody, Phys. Rev. 136, A166 (1964).

[7] G. W. Webb, Z. Fisk, J. J. Engelhardt, and S. D. Bader, Phys. Rev. B 15, 2624 (1977).

[8] R. Gersdorf, F. A. Muller, and L. W. Roeland, Rev. Sci. Instrum. 36, 1100 (1965).

[9] L. F. Mattheiss, Phys. Rev. B 12, 2161 (1975).

[10] B. Klein, L. Boyer, D. Papaconstantopoulos, and L. Mattheiss, unpublished and private communication.

Fermi surface

The Fermi surface of a material is a $\vec{k}$ dependent property, which readily leads to a detailed comparison between experiment and band theory. The Fermi surface is a cut at the Fermi level through the energy bands and it is easily derivable from the band structure. The interest is because it is the sharp border between occupied and empty levels at low temperature. At higher temperature there is a probability of smearing due to the Fermi-Dirac distribution functions. In a metal the electrons which are close to or at the surface, are the most mobile, since they can move with a small amount of energy to other $\vec{k}$ states.

The Fermi surface of the isoelectronic A-15 materials Nb_3Sn, V_3Si and V_3Ge have been studied experimentally by many techniques, which include magnetothermal oscillations[5], de Haas-van Alphen effect[6] and positron annihilation techniques[7-10]. The quantum oscillation techniques yield frequencies which can be correlated to the extremal Fermi surface cross-sectional areas. The second reprint of this chapter, ref.6, discusses the de Haas-van Alphen effect in Nb_3Sn. The positron annihilation data can also give direct information concerning the Fermi surface topology.

Figure 3 of the first reprint shows the APW derived Fermi surface. The labelling of the bands started with the lowest valence band. Each band can be occupied by two electrons, one with spin up and one with spin down. Nb_3Sn has 38 valence electrons, so the Fermi energy has to fall between band 19 and 20. The five M centered pieces and the big Γ centered piece are hole like while the open surface labelled 20 and the small Γ centered are electron like sheets.

The construction of a three-dimensional Fermi surface requires many *ab initio* calculations, in practice this is not feasible thus various interpolation schemes are required. A M-cubic harmonic fit has been used for the ellipsodal like M centered pieces in Nb_3Sn. The generalized $\vec{k}.\vec{p}$ interpolation scheme (see ref.4 and chapter IIb) can be applied to all parts of the Fermi surface which gives a good reflection of the *ab initio* Fermi surface along the high symmetry planes. Figure 3.2 shows the $\vec{k}.\vec{p}$ derived Fermi surface. As discussed in chapter IIb the total fit is a summation of four local $\vec{k}.\vec{p}$ fits. The four centers are the high symmetry points. Points far away from every Brillouin zone corner are

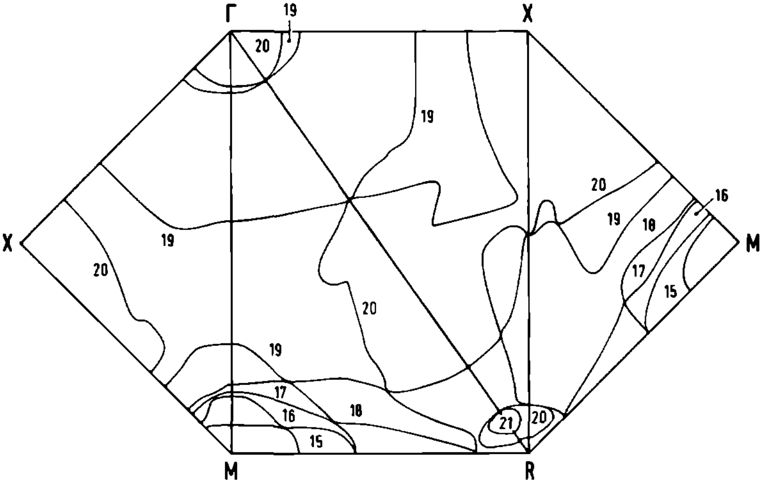

Figure 3.2 The $\vec{k}.\vec{p}$ derived Fermi surface of Nb_3Sn

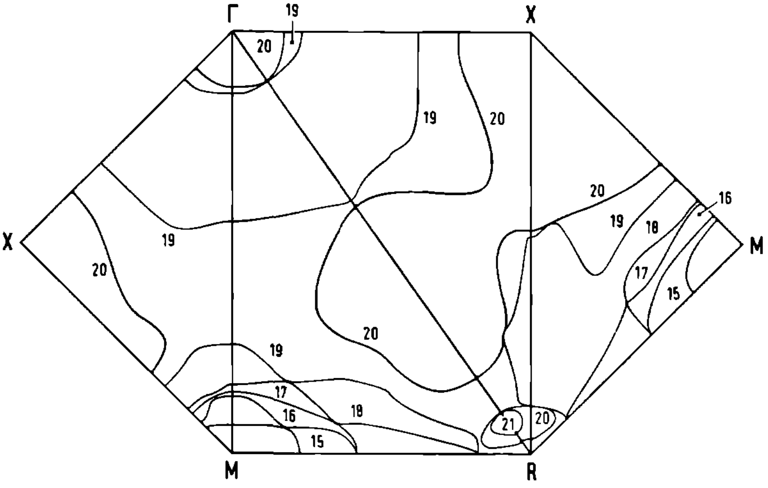

Figure 3.3 The combined $\vec{k}.\vec{p}$ and Fourier Fermi surface of Nb_3Sn

difficult to fit and in these regions one introduces artificial band slopes which have their origin in the combining function. The large 20 surface in figure 3.2 demonstrates these effects. The gradient of the bands at the Fermi level, the Fermi velocity are also artificial in these regions.

The calculation of the averaged Fermi velocity and thus the plasma energy and the anisotropy of H_{c_2} in section "Applied Superconductivity" requires a Brillouin zone integration. However the entire Fermi surface should be represented correctly before such an integration should be evaluated. We require that sheet 20 is smooth throughout the zone, thus we apply the Fourier fit scheme rather than the $\vec{k}.\vec{p}$ scheme. The Fourier fit scheme has also been used to obtain the density of states shown in figure 3.1. In order to improve the accuracy of the fit one hundred twenty additional $\vec{k}$ points for band 20, close to the Fermi surface, have been fit to fourty symmetrized Fourier stars. This Fourier fit is only valid in a small energy range around the Fermi level (from 0.680 to 0.690 Ry) and is only used for the representation of the band 20 Fermi surface; the small sheets close to Γ and R remain in the $\vec{k}.\vec{p}$ fit. Figure 3.3 shows the combined Fermi surface fit. This new fit is used in the section "Applied Superconductivity".

Table 3.1 lists the correspondence between the experimental and theoretical the de Haas-van Alphen frequencies. In addition, it lists the calculated cyclotron band masses, which are not corrected for the electron-phonon mass enhancement. The size of this correction, to the band masses, can be estimated from heat capacity measurements[11] as 1.2 or from tunneling measurements[19] as 1.8. This large electron-phonon enhancement is due to soft phonon-modes present in many high T_c superconductivity materials. The M centered orbit properties are calculated from the M harmonic fit, while the Γ centered orbit data are derived from $\vec{k}$ vectors found from the APW secular matrix. The errors of the two 19th masses are relatively large because they were found by numerical differentiation.

The positron annihilation technique, as far as we know, has not been used to study Nb_3Sn single crystals. However V_3Si, which is isoelectronic to Nb_3Sn, has been the subject of several positron annihilation measurements[7-10].

TABLE 3.1 Areas and effective masses in the [001] and [110] directions. All entires are given in atomic units.

Symmetry	[001]			[110]		
	A_{exp} (x100)	A_{theory} (x100)	m^*_{theory} b)	A_{exp} (x100)	A_{theory} (x100)	m^*_{theory} b)
M-centered orbits a)						
15 (z)		0.47	0.23	1.28	1.16	0.42
16 (z)		0.74	0.64		2.02	0.97
15 (x,y)	1.12	1.17	0.35		0.65	0.32
17 (z)		1.43	0.43			
18 (z)	1.58	1.61	0.46			
16 (x,y)		2.01	1.03		0.99	0.77
17 (x,y)				1.59	1.66	0.49
Γ-centered orbit						
19		13.14	2.13 ± .05		13.66	2.9 ± .15

Notes:

a) The M orbits are ordered from low to high frequency in the [001] direction of figure 2 on page 60

b) m^*_{theory} should be multiplied by $1+\lambda(\simeq 2.5)$ to obtain the experimental masses

The dHvA data of Arko *et al.*[6] for V_3Si, taken along [100] and [110], show oscillations whose ratios are within 5% of those of Nb_3Sn, although the magnitudes differ by about 7%. We interprete these data to imply that the Fermi surfaces of Nb_3Sn and V_3Si are microscopically rather similar (the M-centered pieces represent only a small volume of $\vec{k}$ space). If we make a comparison between the V_3Si positron annihilation derived Fermi surface and our calculated Nb_3Sn surface, we can perhaps make some detailed statements about the relationship of the electronic structure of these two A-15's materials.

Samoilov and Weger[8] have reported positron annihilation experiments in V_3Si in the [100] direction. Although they have enhanced the sensitivity of their data by means of a novel folding technique, the resolution of their experiment was limited to 0.5 milliradians (or 0.20 π/a units). They find (their figure 2) a derivative structure of the momentum distribution with three peaks along [100] at 0.19, 0.64 and 0.84 π/a units. A planar section of the Fermi surface perpendicular to the measure direction gives rise to discontinuities in the momentum distribution, hence to δ-function singularities in its derivative. This is strong evidence for boxlike Fermi surface pieces. If we now focus on our calculated Nb_3Sn surface, we see two cubical boxlike structures of band 20 and 19 centered at Γ and intersecting the Γ to X ([100]) line at 0.15 and 0.64 π/a units, respectively, and the Γ to M ([110]) line at 0.15 and 0.62 π/a units, respectively. Figure 3.4 shows one half of the Γ centered band 19 Fermi surface. Visible is the planar structure perpendicular to the [100] direction. These boxlike features are also invariant to slight shifts ($\pm$ 3 mRy) of E_F, although the exact intersection distances varies slightly with E_F. Clearly there is a good agreement between the flat band 20 and 19 intersections of [100] and Samoilov and Weger's first two peaks[8]. Band 20 is a possible candidate for their third peak, particularly the flat structure centered at X in confluence with the multiple structure at M. However the identification of the third peak remains tentative.

Manuel *et al.*[9] measured the angular correlation of the positron annihilation radiation also for V_3Si. Their derived Fermi surface topology is in agreement with our Nb_3Sn derived Fermi surface. Their conclusions and our interpretations are the following. There is a hole box centered at Γ whose edge is at 0.25 ± 0.07 π/a, our band 20 box. There is an electron box centered at Γ with a 0.75 ± 0.07 π/a edge, our 19th box. In addition, there is a hole ellipsoid like structure at M, one of our M centered ellipsoids (band 15 through 18) and they have

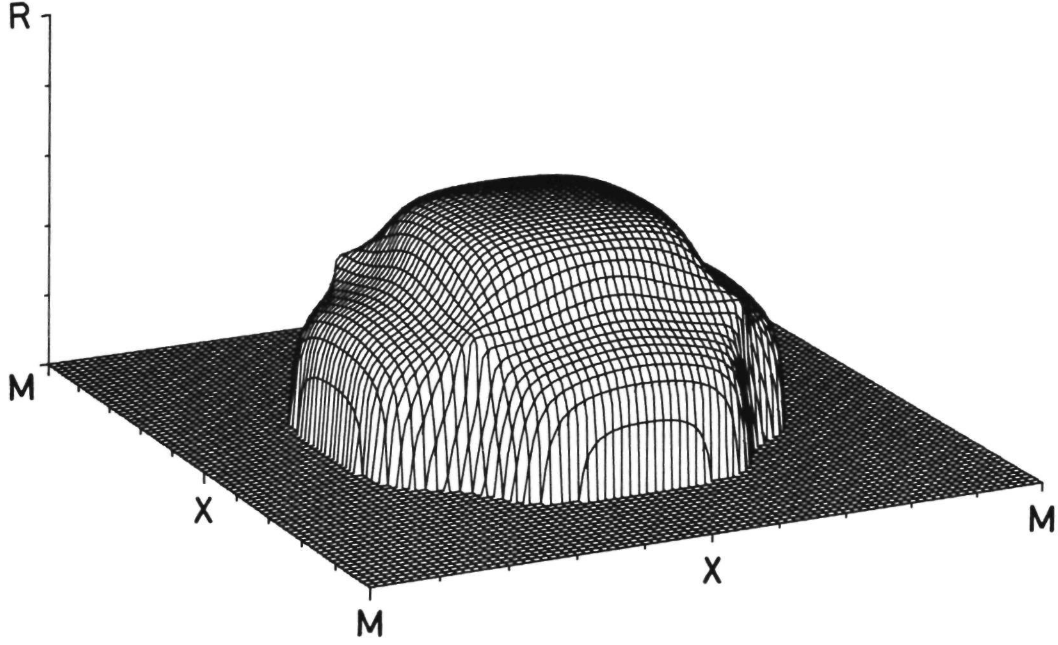

Figure 3.4
One half of the Γ centered boxlike Fermi surface sheet labelled 19

seen electron structure at R, which perhaps can be interpreted by our small electron pockets 20 and 21. However, there is one rather strange phenomena namely the charge signs of the Γ centered boxes are reversed (a hole becomes an electron pocket and visa vera). Our Γ_{12} band which is the origin of the boxes is in qualtitative agreement concerning slope with other Nb_3Sn band calculations (see chapter V).

Farmer *et al.*[10] have also performed two-dimensional angular correlation studies of the positron annihilation radiation of V_3Si. Their conclusions which are shown in figure 4 of ref. 12 are two nested cylindrical surfaces along the zone edges ($r=0.2$ and 0.4 π/a), a hole surface around R, and extra electron density centered at X. The first observation can be described by a cylindrical like surface with $r=0.1$ π/a formed by bands 15, 16 and 18, and by a not completely cylindrical surface with $r=0.25$ π/a formed by bands 18 and 19. The second observation of Farmer *et al.* can not be related to one of our sheets, while the last conclusion can be related to our band 20 which surrounds almost completely X. Strange, Farmer *et al.*[10] did not find any evidence for a boxlike structure.

This boxlike structures are important because it has the same physical effects as the linear chain or Labbé-Friedel -Weger band model[13]. The distance between nearest neighbors in one chain is about 20% less than the distance between nearest neighbors in different chains. Suppose that the electronic band structure of the *d* electrons of the Niobium (or the Vanadium) atoms can be described in the tight-binding approximation. If only nearest neighbor interactions are considered, then the chains are decoupled and the band structure has a largely one-dimensional character. The wave functions are localized on one family of chains, the constant energy surfaces are planar, perpendicular to the coordinate axes, and the Fermi surface is composed of rectangular "boxlike" surfaces. The surfaces seen by Samoilov and Weger[8], Manuel *et al.*[9] and calculated here indicate quite convincingly that one-dimensional character is present in the high T_c A-15 compounds Nb_3Sn and V_3Si. In chapter V we will discuss the linear chain model more extensively as well as other band models.

Density of states

The density of energy levels per unit volume of a crystal is commonly known as the density of states. It reflects the density of electron bands sorted according to energy, and can be thought of as a horizontal ($\vec{k}$ space) summation of the energy bands. This quantity which is a scalar function, can be expressed by

$$N(E) = \frac{1}{4\pi^3} \int_{E(\vec{k})=E} \frac{dS}{|\vec{\nabla}E(\vec{k})|} \qquad (1)$$

where the integration is over constant energy surfaces. Chapter IIc discusses the integration method, the tetrahedron scheme, as applied in this work. In figure 3.1 of the survey section of this chapter the total density of states is shown from the bottom of the valence band to just above E_F for Nb_3Sn. There we also discuss the experimental density of states obtained from an XPS measurement[3]. Table 1 of the first reprint in this chapter compares the densities of states at the Fermi energy (E_F) derived from several experiments and from our calculation.

As noted above, the density of states shown in figure 3.1 is obtained from the Fourier fit of the APW energy bands. It is plotted in figure 3.5 on a similar energy scale as used for the band structure figure 1 on page 56. We estimate that the vertical accuracy of figure 3.5 is better than 1%[14]. Thus, in a simple model, the electron count used to define E_F could be in error by about 38x1%=0.38 electrons, leading to an error in E_F of $\delta E_F = N/(dN/dE) \simeq 1.6$ mRy. E_F in Nb_3Sn can vary only slightly because the value of the density of states is so large. Although there is much structure on a fine scale, a singular Labbé-Friedel density of states[15] near E_F does not emerge. (It is possible that anomalies exist between the grid points spaced at 1.25 mRy, but we believe that this is unlikely). Since there is no large rise in the density of states just above E_F. there is no evidence from our work to support an electronic Jahn-Teller distortion.

A microscopic test of derivatives of the density of states is provided by the temperature dependence of the magnetic or Pauli susceptibility (χ). In most metals the temperature dependence of χ is

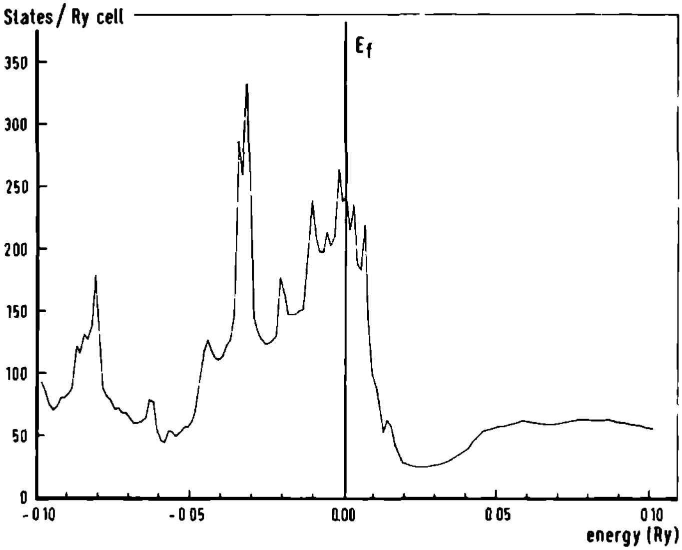

Figure 3.5 The Fourier fit derived electronic density of states of Nb_3Sn *near* E_F *and on a scale similar to fig.1 (page 56)*

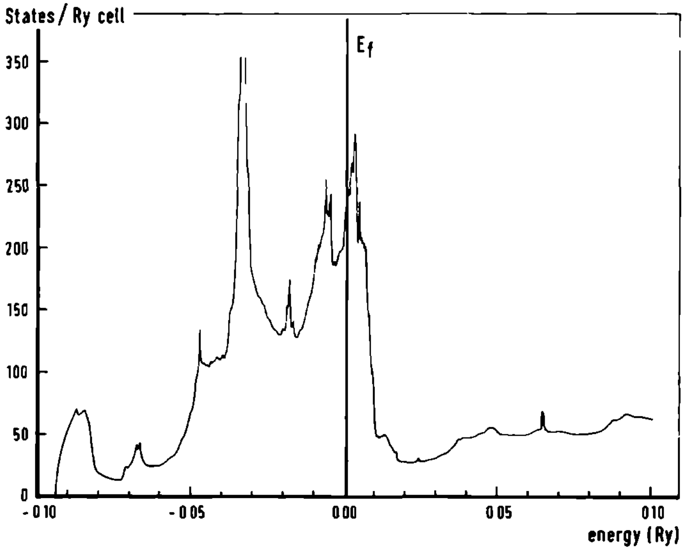

Figure 3.6 The $\vec{k}.\vec{p}$ *derived density of states of* Nb_3Sn

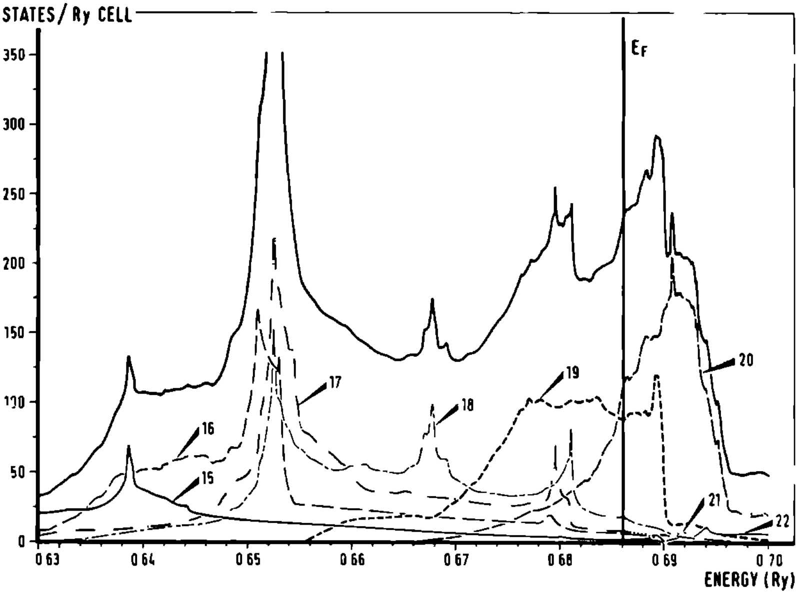

Figure 3.7 The band by band decomposition of the $\vec{k}.\vec{p}$ derived density of states of Nb_3Sn near E_F.

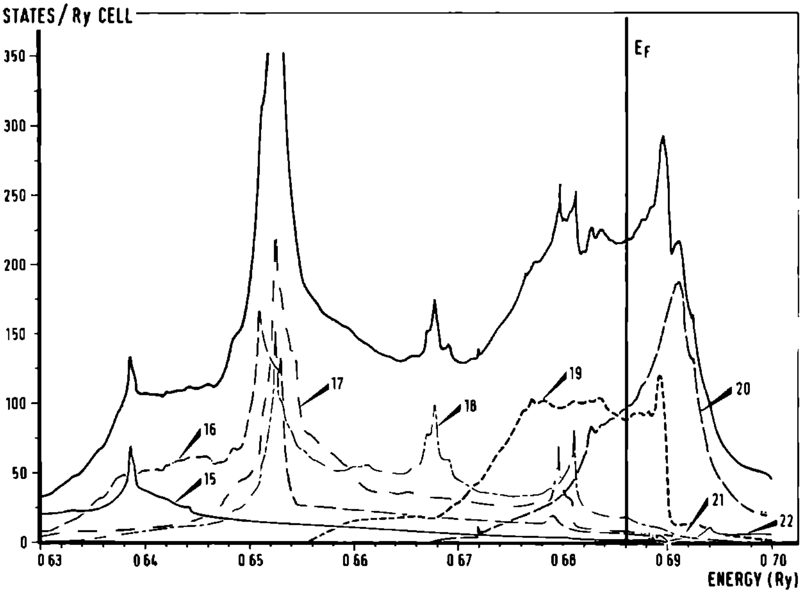

Figure 3.8 Similar to figure 3.7, except band 20 is now fitted by Fourier series.

very small. The first reprint of this chapter discusses the calculation and results of $\chi(T)$. The dominant effect is that the Fermi level itself is strongly temperature dependent and varies by more than 4 mRy as the temperature ranges from 0^{o} to 300^{o}K. The possibility of such strong Fermi level motion in Nb_3Sn has previously been stressed in the model calculations of Cohen *et al.*[16] A microscopic examination shows that the band model density of states of figure 3.5 is rather similar in its features to the Cohen model and without adjustment would fit, in the same way, the temperature dependent resistivity[16].

As discussed earlier the generalized $\vec{k}.\vec{p}$ interpolation method is applied to the Nb_3Sn APW energy bands. The $\vec{k}.\vec{p}$ representation of the electronic bands around E_F is used to calculate a finer density of states in this energy region. Figure 3.6 which has the same horizontal scale as figure 3.5, shows the $\vec{k}.\vec{p}$ derived density of states. The difference in N(E) below -0.05 Ry between the two figures is arising from the fact that only bands around E_F are included in the $\vec{k}.\vec{p}$ fit set. No anomalies appear in N(E) if the space between the grid points is lowered to 0.1 mRy. This result was already above suggested.
The Fermi energy in the $\vec{k}.\vec{p}$ fit is calculated to be 1 mRy higher than in the Fourier fit. This shift is within the root mean square error of the Fourier and $\vec{k}.\vec{p}$ fit and comparable to the error inherent in the *ab initio* band structure.

The detailed structure around E_F (+10 mRy) shows microscopic differences between the two densities of states. Remaining, however, is the steep drop in N(E) at E_F+7 mRy. This fall in the density of states is situated, within 1 mRy, at the same place in the Fourier case. So the temperature dependence of the susceptibility, calculated from the $\vec{k}.\vec{p}$ fit, will be of the same order as calculated previously (figure 2 on page 57). A large $N(E_F)$ is also present in both fits, namely 243 and 232 states/Ry-unit cell, respectively.

Figure 3.7 shows the band by band decomposition of the $\vec{k}.\vec{p}$ density of states. Note that the energy scale is even more expanded than in figure 3.6. The various kind of van Hove singularities which are visible in the figure can be labelled by the wave function character at the high symmetry points. For example, the enormous peak at 0.652 Ry can be labelled Γ_{25}' The density of states at the Fermi energy is for 85%

derived from contributions of band 19 and 20. This corresponds to the Fermi surface of the big hole centered at Γ and the electron sea around X, respectively. Another surprizing effect found by this decomposition is the drop in band 19 density of states 4 mRy above E_F. This drop is from 120 to 15 states/Ry unit-cell, and can in part be responsible for the extreme temperature dependence of the Pauli susceptibility. The susceptibility does not show such a drastic dependence since band 20 rises by 60 states/Ry-unit cell in the same energy range.

Figure 3.8 is equivalent to figure 3.7 except the $\vec{k}.\vec{p}$ fit of band 20 is replaced by its Fourier fit. This replacement has been discussed above. As expected there are no large changes in the overall density of states. The N(E) of band 20 is now smooth compared to its subdensity of states in figure 3.7, because the artificial singularities created in the bands have now been eliminated. The gradient of the energy and thus the density of states contribution is now reliable in that Brillouin zone region. The $N(E_F)$ in the new fit is 221 states/Ry-unit cell which is 5% lower than in the complete $\vec{k}.\vec{p}$ fit. The change in E_F itself is on a milliRydberg scale negligible. The rise in band 20 subdensity of states at 0.690 Ry remains.

In conclusion, a large $N(E_F)$ is a firm property of Nb_3Sn, and its N(E) curve shows a large drop just above E_F. The first feature gives anomalous values to some derived quantities (see next section) and the second feature is maybe responsible for the anomalous temperature dependence of several properties (listed in chapter I).

This last section of this chapter on Nb_3Sn presents calculations of several transport properties and of the anisotropy of the upper critical field (H_{c_2}). This work is done in collaboration with Dr. R. Blaschke of the Gesamthochschule Wuppertal at Wuppertal, West Germany.

The Drude plasma energy, Ω_p; the averaged Fermi velocity at the Fermi energy, $<V_F^2>^{\frac{1}{2}}$; and the London penetration depth at $0^{o}K$, λ_L^* can be derived from the electronic band structure near E_F[17]. The function $x(\vec{k})$ averaged over k space is defined as $<x(\vec{k})>$. The asteriks superscript for lambda, the penetration depth, is the renormalized penetration depth as it influences the electron-electron coupling. The Fermi velocity squared is expressed by

$$<V_F^2> \;=\; \frac{1}{4\pi^3} \int_{E(\vec{k})=E_F} dS \;|\vec{\nabla} E(\vec{k})| \tag{1}$$

where the integration is over all Fermi surface pieces, and is evaluated through the application of the Monte Carlo method (see chapter IIc). 45,769 $\vec{k}$ Points in 1/48th of the Brillouin zone were involved, of which 10,000 were situated within 4 mRy of the Fermi level. The summation is performed for each band; a summation over bands is implied in equation (1).

The plasma energy is a measure of the energy involved in the formation of a collective electronic density variation, a plasmon, and its square is given by

$$\Omega_p^2 = \frac{8\pi}{3}\hbar^2 e^2 \;<V_F^2>\; N(E_F) \;=\; \frac{5.24\text{x}10^3 <V_F^2> N(E_F)}{a_0^3} \tag{2}$$

where a_0^3 is the volume of the unit cell in $\mathring{A}^3$ and $N(E_F)$ the density of states at the Fermi energy in states/spin-eV-unit cell. The $N(E_F)$ is obtained by applying the same method and the same $\vec{k}$ points set as used in obtaining $<V_F^2>$.

The London penetration depth gives the distance that an external magnetic field can make itself felt inside a superconductor. The surface of the superconductor is parallel to the field direction[18] and λ_L^* is given by

$$\lambda_L^* = \frac{c\hbar}{\Omega_p} = \frac{1.98\times10^3\ (1+\lambda)^{\frac{1}{2}}}{\Omega_p} \qquad (3)$$

where $(1+\lambda)^{\frac{1}{2}}$ is the renormalisation factor which one can derive from experiments, for example electron tunneling measurements[19] ($\lambda=1.8 \pm 0.15$).

Table 3.2 lists some calculated transport quantities and those derived from experiments. Our agreement with the experimental data is better than that found from other band structure calculations. Those band structures were also obtained by APW calculations but did not include a general form of potential.

Macroscopic anisotropy phenomena[25] are observed in the magnetisation curve of crystalline superconductors (e.g. the anisotropy of H_{c1} and H_{c_2}), and in the structure of the flux-line lattice of the mixed state. The anisotropy of a quantity is the dependence of that quantity on the orientation of the crystal axes relative to the direction of the external magnetic field. In addition, a correlation exists between the symmetry of the crystal lattice and the structure of the flux-line lattice, and a relation between the relative orientation of these two lattices. Among the various macroscopic anisotropy phenomena, up to now only the anisotropy of H_{c_2}, the upper critical field of a type II superconductor, has been extensively investigated by theory[26-28] and experiment (e.g. for Nb_3Sn by Foner and McNiff[29]). The anisotropy of H_{c2} reflects the microscopic anisotropies of the electronic system, i.e. the electronic anisotropies in the normal state (Fermi surface and Fermi velocity) and the anisotropy of the energy gap of the superconducting state.

In cubic metals the dependence of H_{c_2} on the orientation of field direction $\hat{H}$ relative to the crystal axes obviously has to reflect the cubic symmetry. Hence the orientation dependence of $H_{c_2}(\hat{H})$ (or of the relative anisotropy $\Delta H_{c_2}(\hat{H})/\bar{H}_{c_2}$) may be expressed[27] in terms of orthonormalised cubic harmonics[30] $H_l(\hat{H})$ of the identity representation

$$\frac{\Delta H_{c_2}(\hat{H})}{\bar{H}_{c_2}} \equiv \frac{H_{c_2}(\hat{H})-\bar{H}_{c_2}}{\bar{H}_{c_2}} = \sum_{l=4,6..} H_l(\hat{H})\ a_l(t,\alpha) \qquad (4)$$

TABLE 3.2 Calculated and experimental transport parameters of Nb_3Sn

Source	$\langle V_F^2\rangle^{\frac{1}{2}}$ (10^8 cm/sec)	$\langle V_F^{*2}\rangle^{\frac{1}{2}}$ (10^8 cm/sec)	$N(E_F)$ (states/ eV-cell)	Ω_p (eV)	λ_L^* (Å)
our work	0.318	0.114	16.2	5.41	610
other band calculations:					
Mattheiss *et al.*[17]	0.305	0.110	7.1	3.42	965
Klein *et al.*[20]	0.278	0.100	11.7	4.00	
experimental work:					
Orlando *et al.*[21]		0.074	15±6		
Tüttö *et al.*[22]				4.0	
"				5.6	
Arnolds *et al.*[23]					600
Blaschke[24]					690

$\lambda = 1.78$ taken from Ref.19

TABLE 3.3 Calculated anisotropy parameters of H_{c2} in Nb_3Sn

l	γ_l^{1F}	γ_l^2
4	.34 ± 0.2	.15 ± .013
6	.18 ± 0.16	-.03 ± .01
8	.27 ± .02	-.02 ± .01

where $\bar{H}_{c2}$ denotes the average over all possible field directions. An additional subscript should be introduced in the notation of cubic harmonics to label the different irreducible representations for an l equal twelve or higher. We suppress this subscript since high order angular momentum contributions are far beyond the resolution of present H_{c2} anisotropy measurements. The expansion coefficients $a_l(t,\alpha)$ reveal the microscopic anisotropies of the superconducting electron system. These coefficients depend on the reduced temperature ($t=T/T_c$) and on the impurity parameter α which measures the impurity scattering in the sample.For weak coupling superconductors with small anisotropy (only linear effects are considered) Teichler[27] has given an expression of the form

$$a_l(t,\alpha) = C_l \, [\gamma_l^{1F} \, h_l^{1F}(t,\alpha) + \gamma_l^{1\Phi} \, h_l^{1\Phi}(t,\alpha) + \gamma_l^2 \, h_l^2(t,\alpha) \,] \tag{5}$$

The numerical coefficients C_l are given in Ref.27. The quantities

$$\gamma_l^{1F} = \langle H_l(\hat{V}_F) \rangle_{FS} \tag{6}$$

$$\gamma_l^{1\Phi} = 2\langle H_l(\hat{V}_F)(\Delta_p/\langle\Delta_p\rangle-1)\rangle_{FS} \tag{7}$$

$$\gamma_l^2 = \langle H_l(\hat{V}_F)(V_F^2/\langle V_F^2\rangle-1)\rangle_{FS} \tag{8}$$

where $V_F.\hat{V}_F$ is the Fermi velocity and Δ_p is the gap function in the pure state, are material parameters of the host metal. The parameters $\gamma_l^{1\Phi}$ describe the anisotropy of the attractive electron-electron coupling and thus the anisotropy of the energy gap of the pure material. γ_l^{1F} measures the anisotropy of the direction of the Fermi velocity and thus the shape of the Fermi surface and γ_l^2 characterizes the anisotropy of V_F^2. The h_l^i (t,α) are weight functions describing the weights by which these different microscopic anisotropies contribute to the anisotropy of H_{c2}. Numerically calculated plots of the $h_l^i(t,\alpha)$ have been published in Ref. 27 for $l=4$ and $l=6$ and $0\leq\alpha\leq2$.

From our electronic band structure of the cubic normal state of Nb3Sn we are able to calculate the material parameters γ_l^{1F} and γ_l^2. We can not derive $\gamma_l^{1\Phi}$, so we ignore it. Although $\gamma_l^{1\Phi}$ is comparable to γ_l^{1F}, but experiments show a small gap anisotropy of Nb_3Sn[31]. Table 3.3 gives the calculated γ_l^{i}'s. From these values and using the plots of $h_l^{i}(t,\alpha)$ in Ref.27, we evaluate equation 4 for several reduced temperatures and impurities.

Foner and McNiff[29] measured the anisotropy of H_{c_2} in Nb_3Sn single crystals; they found at 8°K $H_{c_2}[100]>H_{c_2}[111]>H_{c_2}[110]$and $\delta=(H_{c_2}[100]-H_c[110])/H_{c_2}[100]\approx 0.05$. On the contrary Arko *et al.* found that in Nb_3Sb H_{c_2} is isotropic to within 1% the accuracy of their measurements. The temperature of the samples and their purity were different for the two experiments. We found for the pure material (α=0.0) at t=0.5 (T=8.5°K) an $\delta=0.06 \pm 0.01$ which is within the experimental error equal of the Foner and McNiff value. An increase of α will decrease our δ. The ordering in $H_{c_2}(\hat{H})$ is slightly different, we find $H_{c_2}[100]>H_{c_2}[111]>H_{c_2}[110]$,but the difference between the last two is only 10% of the difference between the first two.

The behavior of $H_{c_2}(\hat{H})$ for Nb_3Sn below the critical temperature T_c, can be expressed using a perturbation on the H_{c_2} behavior at T_c[28]. Of course, $H_{c_2}(T=T_c)=0$ kG, so we will normalize with respect to the derivative of H_{c_2}

$$H'_{c_2} = -T_c \left. \frac{\delta H_{c_2}}{\delta T} \right|_{T=T_c} \tag{9}$$

Berthel and Pietrass[28] derived such an expression for clean superconductors. They deduce an expression for H_{c_2} as function of the reduced temperature dependence $\Theta=1-T/T_c$,

$$H_{c_2}(\Theta,\hat{H})/H'_{c_2} = \Theta+1.35\Theta^2+3.065[A_1+A_2K_2(\hat{H})]\Theta^2+O(\Theta^3) \tag{10}$$

where

$$A_1 = (8/15)(<U_F^4>_{FS}-1) \tag{11}$$

$$A_2 = (1/2)(5<U_{F,x}^4>_{FS}-<U_F^4>_{FS}) \tag{12}$$

$$\vec{U}_F = \vec{V}_F/<V_F^2>_{FS}^{\frac{1}{2}} \tag{13}$$

$K_2(\hat{H})$ is the second order cubic harmonic[30]. A_2 is the anisotropic parameter of the lowest order, and is similar to the Fermi surface average of the fourth order cubic harmonic $<H_4(\hat{V}_F)>_{FS}$, which is equivalent to γ_4^{1F} in Teichler's theory[27]. The isotropic averages like A_1 are absorbed in a redefinition of the parameters which determine the magnitude of the coefficients h_l^i.

A_1 and A_2 were calculated at the same time, so the same $\vec{k}$ point set is involved, as the Teichler quantities. A_1 and A_2 are found from the Fermi velocity at the Fermi surface alone. A_1 is equal to 0.28 and A_2 is equal to 0.13, so both are positive. A_2 is also found[28] as positive from experimental data[29]; in that we agree.

This section calculated several superconductivity quantities only. We hope that in the future more experiments will be performed which will answer the validity of our calculated parameters. Perhaps the Nijmegen high magnetic field facility can be used.

1 G.E.Hardy and J.K.Hulm,Phys.Rev.93,1004 (1954)

2 Reviews have been given by L.R.Testardi in *Physical Acoustics*,edited by W.P.Mason and R.N.Thurston (Academic Press,New York,1973)Vol.X; by M.Weger and I.B.Goldberg in *Solid State Physics*,edited by H.Ehrenreich,F.Seitz and D.Turnbull (Academic Press,New York,1973) Vol.28

3 H.Höchst,S.Hufner and A.Goldmann,Solid State Comm.19,899 (1976)

4 H.J.F.Jansen and F.M.Mueller,Phys.Rev.B20,1426 (1979)

5 J.E.Graebner and J.E.Kunzler,J.of Low Temp.Phys.1,443 (1969)

6 A.J.Arko,D.H.Lowndes,F.A.Muller,L.W.Roeland,J.Wolfrat,A.T.van Kessel,H.W.Myron,F.M.Mueller and G.W.Webb,Phys.Rev.Lett.40,1590 (1978),see also page 55

7 S.Berko and M.Weger,Phys.Rev.Lett.24,55 (1970)

8 S.Samoilov and M.Weger,Solid State Comm.24,821 (1977)

9 A.A.Manuel,S.Samoilov,R.Sachot,P.Descouts and M.Peter,Solid State Comm.31,955 (1979)

10 W.S.Farmer,F.Sinclair,S.Berko and G.M.Beardsley,Solid State Comm. 31,481 (1979)

11 G.S.Knapp and S.D.Bader,Phys.Rev.B13,3783 (1976)

12 S.Berko,W.S.Farmer and F.Sinclair in *Superconductivity in d- and f-Band Metals*,edited by H.Suhl and M.B.Maple (Academic Press,New York,1980)

13 M.Weger,Rev.Mod.Phys.36,175 (1964),and M.Weger and I.B.Goldberg in *Solid State Physics*,edited by H.Ehrenreich,F.Seitz and D.Turnbull (Academic Press,New York,1973)Vol.28

14 A.T.van Kessel,H.W.Myron and F.M.Mueller,J.of the Less-Common Metals,62,49 (1978)

15 J.Labbé and J.Friedel,J.Phys.27,153 (1966)

16 R.W.Cohen,G.D.Cody and J.J.Halloran,Phys.Rev.Lett.19,840 (1967)

17 L.F.Mattheiss and L.R.Testardi,Phys.Rev.B17,4640 (1978);Phys.Rev. B20,2196 (1979)

18 R.Meservey and B.B.Schwartz in *Superconductivity*,edited by R.D. Parks (M.Dekker Inc.New York,1969)Vol.I

19 E.L.Wolf,J.Zasadzinski,G.B.Arnold,D.F.Moore,J.M.Rowel and M.R. Beasley,Phys.Rev.B22,1214 (1980)

20 B.M.Klein,D.A.Papaconstatopoulos and L.L.Boyer,in *Superconductivity in d- and f-Band Metals*, edited by H.Suhl and M.B.Maple (Academic Press,New York,1980)

21 T.P.Orlando,E.J.McNiff jr.,S.Foner and M.R. Beasley,Phys.Rev.B19,4545 (1979)

22 I.Tüttö,L.M.Kahn and J.Ruvalds,Phys.Rev.B20,952 (1979)

23 G.B.Arnolds,R.Blaschke,H.Peel and P.Pröch,IEEE Trans.on Magnets Mag 15,27 (1979)

24 R.Blaschke,Adv.in cryogenic engineering 26,425,in press

25 A list of ref.is given by H.Teichler in *Superconductivity in d- and f-Band Metals*, edited by D.H.Douglass (Plenum Press,New York,1976)

26 P.C.Hohenberg and N.R.Werthamer,Phys.Rev.153,493 (1967)

27 H.W.Pohl and H.Teichler,Phys.Stat.Sol.(b)75,205 (1976)

28 K.H.Berthel and B.Pietrass,J.of Low Temp.Phys.33,127 (1978)

29 S.Foner and E.J.McNiff jr.,Phys.Lett.58A,318 (1976)

30 F.C.von der Lage and H.A.Bethe,Phys.Rev.71,612 (1947)

31 M.Gurvitch,A.K.Ghosh,C.L.Snead jr. and M.Strongin,Phys.Rev.Lett.39, 1102 (1977)

In contrast to Nb_3Sn which is discussed in the previous chapter, Nb_3Sb has a low superconducting critical temperature[1] (T_c=0.2°K), although these two A-15 compounds differ by only one additional valence electron per B side atom. Tin has a $5s^2\,5p^2$ configuration and antimony a $5s^2\,5p^3$. The lattice constants of Nb_3Sn and Nb_3Sb are very similar 9.981 and 9.928 atomic units, respectively. Other properties of Nb_3Sb are a small density of states at the Fermi energy[1] ($N(E_F)$=51 States/Ry-cell),small compared to that of Nb_3Sn: the smallest, known electron-phonon enhancement[2] in an A-15 (λ=0.3). Nb_3Sb does not show a phonon-mode softening with decreasing temperature[1]. This softening is a characteristic of the A-15 compounds.

The rigid band (RB) approximation[3], a rough estimate to the electronic structure, can be applied here since the lattice constants of Nb_3Sn and Nb_3Sb differ less than 0.5% and the character of the conduction electrons is the same (*d*-type for both materials). Using the rigid band approximation the Nb_3Sn electronic band structure can be used as a model for that of Nb_3Sb. The Fermi energy of this model Nb_3Sb band structure must be shifted upward from that of Nb_3Sn to accommodate for the additional two electrons, which is equal to one band. Figure 1 on page shows the Nb_3Sn band structure with the estimated Nb_3Sb Fermi energy. The $N(E_F)$ is then estimated to 50 States/Ry-cell (see figure 3.5) and the derived Fermi surface has two electron holes at M and four electron pockets at R. We used this Nb_3Sb Fermi surface estimate for a first comparison with the existing de Haas-van Alphen data.

Arko, Fisk and Mueller[4] proposed from their dHvA frequencies a Fermi surface which is built of a small ellipse and a bigger cylinder both centered at M and a small sphere centered at R. In addition, they assumed that the M cylinders are in contact to each other via an R centered surface (see fig.3 in ref.4). From the model band structure of Nb_3Sb (fig.1 on page 56) we see a small ellipse arising from the M_2 level, a bigger M centered Fermi surface sheet originating from the conduction level M_9 ,two small R centered pockets and finally two bigger

R centered pieces. The interconnection of the big M and R centered sheets along the line T (R to M) is also possible. All the Fermi surfaces pieces of Nb_3Sb proposed by Arko *et al.*[4] are present in our rigid-band model. Aware of this similarity, it is worthwhile to perform an *ab initio* band calculation of Nb_3Sb, in order to produce a Nb_3Sb Fermi surface which can serve as further guide in understanding the new experimental data.

Survey

The electronic band structure of Nb_3Sb is calculated along the same lines as that of Nb_3Sn. This procedure is explained in detail in chapter IIa. The results of these calculations are shown along the high symmetry lines in figure 1 of the hereafter following reprint. As explained above, the calculation of de Haas-van Alphen frequencies needs an accurate and fast interpolation method of the electronic bands at E_F. One of the possible methods is the generalized $\vec{k}.\vec{p}$ method which is discussed in chapter IIb. The band structure shown in figure 4.1 is obtained by the $\vec{k}.\vec{p}$ matrices described in appendix A and the fit of 286 independent $\vec{k}$ points, where the APW spectrum is calculated. Because of the smaller secular matrix (15 vs.300) the $\vec{k}.\vec{p}$ method is about 10,000 times faster than the calculation of the energy bands from the APW secular matrix. We obtain a band structure which is almost identical to the APW bands (fig.1 on page 88). Along some lines (e.g. S one sees the limits of the local fit scheme, as small "wiggles" in the band structure. No "wiggle" is commensurate with a band near E_F.

The $\vec{k}.\vec{p}$ fit is first used for the calculation of the density of states and from this the Fermi energy is derived. The density of states of Nb_3Sb close to E_F ($\pm$ 100 mRy) is shown in figure 4.2. This density of states is obtained through the application of the tetrahedron method (see chapter IIc). Bands below -0.06 Ry and above 0.11 Ry are not included in the $\vec{k}.\vec{p}$ fit set. A comparison between this density of states and the one of Nb_3Sn (figure 3.6) shows many similarities, only for Nb_3Sb E_F falls to the right side of the Nb *d* band manifold instead of within the *d* band complex as for Nb_3Sn. Our calculated value of $N(E_F)$ (39 states/Ry-unit cell) when compared to the value derived from the heat capacity[1] (51 states/Ry-unit cell) yields a value for $1+\lambda$, where λ,

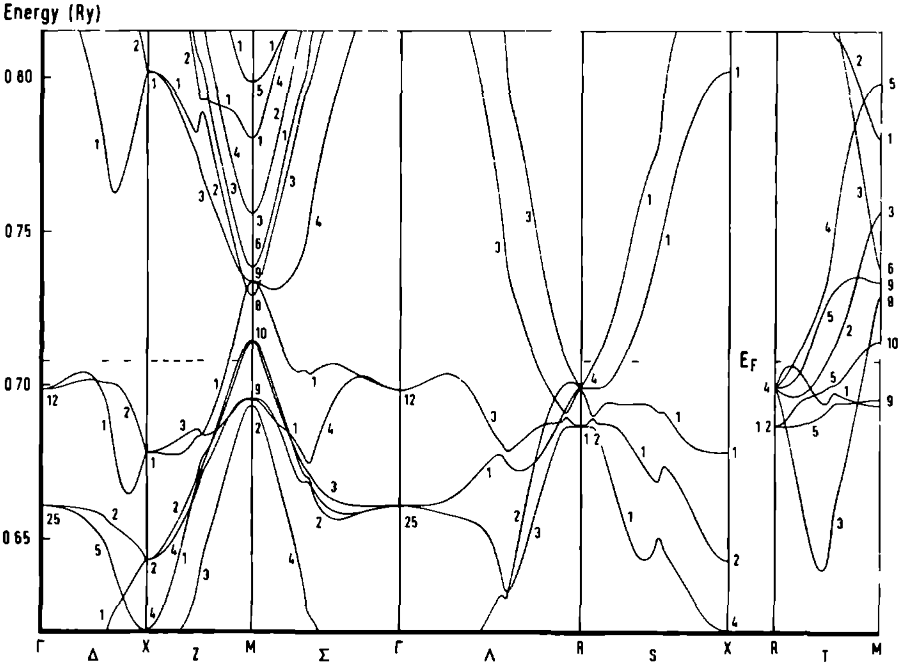

Figure 4.1 The $\vec{k}.\vec{p}$ derived electronic band structure of Nb_3Sb near E_F

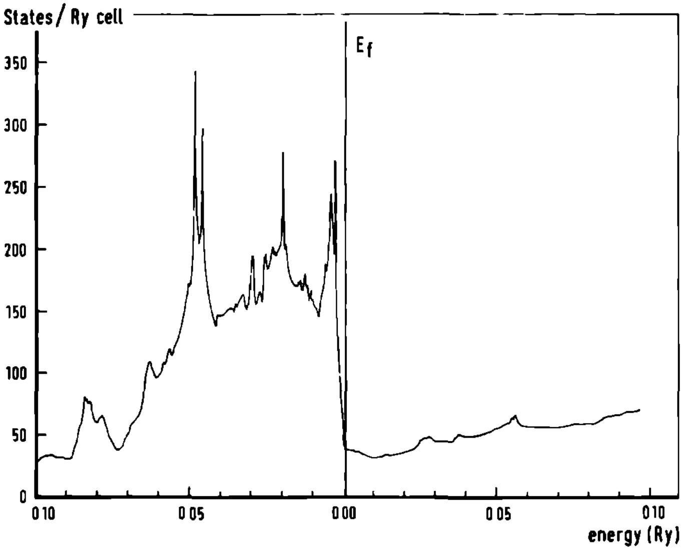

Figure 4.2 The $\vec{k}.\vec{p}$ derived density of states of Nb_3Sb on an energy scale similar to figure 4.1

the electron-phonon enhancement, is the same (λ=0.31) as the value deduced from the McMillan equation from the superconducting critical temperature.

We are now able to generate through our interpolation scheme the de Haas-van Alphen spectrum of Nb_3Sb. The reprint given in this chapter discusses the relation between the renewed dHvA data measured by Arko *et al.*[5] and our proposed spectrum. The hereafter following section gives the calculation details of the Fermi surface and the dHvA spectrum, and the cyclotron masses of the orbits. The derived electron-phonon mass enhancement factor (λ=0.2-0.3) is comparable to the measured value[2]. In addition, the Shubnikov-de Haas data obtained by Sellmyer *et al.*[6] are related to our frequency spectrum.

From a detailed examination of the *ab initio* band structures of Nb_3Sn and Nb_3Sb we can conclude that the rigid band approximation is not valid for the Nb_3Sn/Nb_3Sb system on a fine scale, although an average property like the density of states is only slightly affected. Comparison of the energy levels at the high symmetry points shows that the order is changed for M states. The M_2 lies above E_F in "pseudo" Nb_3Sb and below E_F in the *ab initio* Nb_3Sb. The number of Fermi surface sheets differs at M, we find from the *ab initio* bands three holes instead of the two from the rigid-band approximation. Furthermore the curvature of the R-centered electron pockets is also different (see the T line). Primarily these differences reflect the atomic parentage of the band structures in the two materials. Those levels arising primarily from Nb *d* electrons are more or less the same; those arising primarily from the *s* and *p* orbitals on the B sublattice are, on a scale of a few milliRydbergs, different. The detailed agreement between a microscopic measurement like dHvA spectra and the calculated band structure of Nb_3Sb suggests a high precision. Further measurements beyond Arko *et al.* in Nb_3Sn are strongly indicated.

reprinted from
PHYSICS OF TRANSITION METALS 1980
Inst.Phys.Conf.Ser.No.55 103-106

HIGH PRECISION FERMI SURFACE OF Nb_3Sb

A.T. van Kessel, H.W. Myron and F.M. Mueller
Research Institute for Materials and
High Field Magnet Laboratory
University of Nijmegen
Toernooiveld, Nijmegen, The Netherlands

ABSTRACT

The electronic band structure and Fermi surface of Nb_3Sb have been calculated using an APW method adapted to a general form of potential. A comparison between calculated and measured extremal cross sectional areas showed not only close topological similarity, but also close agreement for all seven Fermi surface sheets. It is concluded that this is the highest precision Fermi surface now known of any A-15 material.

Materials based on the β-wolfram or A-15 crystallographic phase continue to be of interest because of their high superconductivity, phase instabilities, magnetic anomolies and martensitic transformations. Understanding these properties has been slowed somewhat because of intrinsic difficulties; these are multi-atom per unit cell, transition metal compounds, exhibiting complex behavior. Hence it is reasonable to question the extent to which the band approach might be valid or applicable. The Fermi surface has played a dominant rôle in developing understanding in simple, noble and transition metals, so it is natural to consider such experiments in A-15 systems too.

Graebner and Kunzler (1969) have measured the magnetothermal oscillations of V_3Ge; three orbits of very small extremal areas were found. Arko *et al.* (1977) used the de Haas-van Alphen (dHvA) effect and studied Nb_3Sb. Arko *et al.* (1978) observed dHvA oscillations in Nb_3Sn which were interpreted as a series of ellipsiods centered about M following the band structure of van Kessel *et al.* (1978). Positron annihilation has been used to study the Fermi surface of V_3Si by Berko and Weger (1970). More recently two-dimensional experiments have been performed by Manuel *et al.* (1979) and Farmer *et al.* (1979), which have yielded additional information.

Here we present an investigation of the Fermi surface of Nb_3Sb using the APW method. For this A-15 material many of the experimental difficulties are not present. For example, Nb_3Sb crystals are now available with resistivity ratios of 100 to 150 and unlike Nb_3Sn or V_3Si the upper critical field, H_{c2}, is low. In addition new dHvA measurements of Nb_3Sb have been reported by Arko *et al.* (1979).

The band structure was calculated using a general form potential as outlined by van Kessel *et al.* (1978). A large number of $\vec{k}$ points in the vicinity of E_f are required in order to calculate dHvA frequencies. A systematic $\vec{k}.\vec{p}$ interpolation method for the electronic structure has been developed by Jansen *et al.* (1979) and adapted to O_h^3 symmetry.

The electronic structure of Nb_3Sb along the high

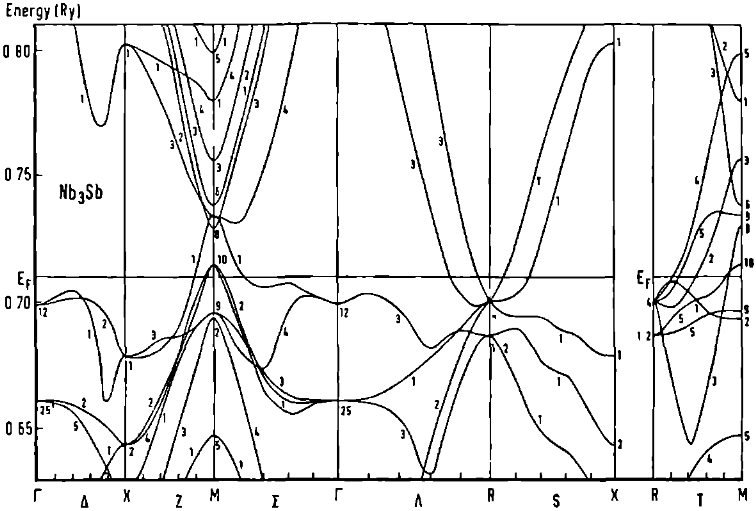

Figure 1. The energy bands of Nb_3Sb

symmetry lines in the vicinity of the Fermi energy is shown in Fig. 1. The Fermi energy falls above the states Γ_{12} and has intersections with the band structure surrounding the M point (holes) and the R point (electrons). The box like Fermi surface sheet surrounding the Γ point previously found by van Kessel *et al.* (1978) for Nb_3Sn is absent in Nb_3Sb. This box like Fermi surface sheet has been confirmed for isoelectronic V_3Si by positron annihilation. One may expect that $Nb_3Sb_{1-x}Sn_x$ forms a rigid band system, however this seems not to be the case, for example the ordering of the states at M from below to above E_f is 9, 10, 2 and 8 for Nb_3Sn and 2, 9, 10 and 8 for Nb_3Sb. The relative shift downward of the M_2 (predominantly Sb p states) with respect to the Nb d band manifold is due to the increasing electronegativity of Sb with respect to Sn.

In Fig. 2 the Fermi surface of Nb_3Sb (intersecting bands 18-24) is shown in the principle symmetry planes. The principle structures are oscullated ellipsoidal holes surrounding the M point and a confluence of electron sheets surrounding the R point. Other calculations on A-15's by Klein *et al.* (1978) and Pickett *et al.* (1979) yield a similar description of the Fermi surface around R, but shifts of approximately 20 mRy are required to obtain small hole pockets about M, using rigid band shifts of their Nb_3X.

In order to provide the best possible description of the Fermi surface of Nb_3Sb, we have utilized the freedom available in our systematic $\vec{k}.\vec{p}$ interpolation scheme to make small adjustments from those parameters derived by fitting the APW bands. For simplicity we restricted our adjustment to shifting the "zeroth" parameters only (i.e. a rigid shift of the entire band). The shifts were all within our estimated error of 3-4 mRy. The high degree of correlation exhibited in Fig. 3 everywhere suggests that the adjusted bands are in error by about 0.3 to 0.4 mRy at most. Some futher dHvA experiments in the (110) plane are in progress as a final check on the validity of our model.

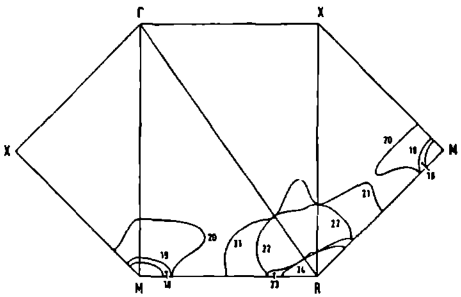

Figure 2. The Fermi surface of Nb_3Sb

While frequency ξ_1 approximately corresponds to the lower branch of band 19, the frequency ξ_2 (open circles), the middle branch of 19, is precisely a second harmonic of α_2. The upper branch of 19 in the (010) plane, according to our calculations, is nearly degenerate with the 24 (β) orbit. This makes positive identification of these orbits difficult. If the magnetic breakdown as reported by Sellmyer *et al.*

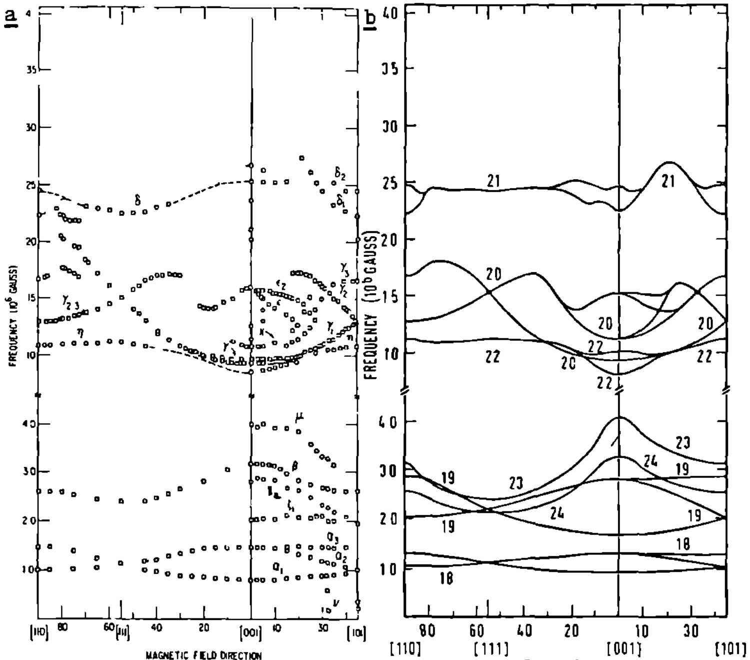

Figure 3. Exp.(a) and calc.(b) dHvA frequencies of Nb_3Sb

(1980) using the Shubnikov de Haas effect, occurs along the [001] direction and gives rise to the ω orbit, we interpret this as a breakdown between the bands 20 and 21 (see Fig. 2). The measured cross sectional area of the breakdown agrees with our interpretation.

We conclude that: 1) the Fermi surface of Nb_3Sb as calculated without any adjustment yields qualitative agreement on a scale of 3-4 mRy with a majority of the dHvA branches, 2) many parts of the dHvA branches denoted as 21(δ), 22(η), 23(μ) and 24(β) were not observed in the initial measurements and were predicted by the band model before additional data was obtained, 3) after remeasuring the frequencies, the dHvA areas were recalculated using adjustments to obtain an optimal fit. We believe this represents the first successful marriage of an *ab initio* calculation to the experimental Fermi surface of any A-15 compound on a scale of less than 1 mRy error.

This work was supported as part of the research program of the Stichting voor Fundamenteel Onderzoek der Materie with financial support from the Nederlandse Organisatie voor Zuiver Wetenschappelijk Onderzoek.

REFERENCES

Arko A J, Fisk Z and Mueller F M (1977) Phys.Rev. B 16,1387

Arko A J, Lowndes D H, Muller F A, Roeland L W, Wolfrat J, Kessel A T van, Myron H W, Mueller F M and Webb G (1978) Phys.Rev.lett. 40,1590

Arko A J, Crabtree G W and Fisk Z (1979) a preliminary report presented on the *Conf.* on *Superconductivity* in *d- and f band Metals*, La Jolla, CA (to be published)

Berko S and Weger M (1970) Phys.Rev.Lett. 24,55

Farmer W S, Sinclair F, Berko S and Beardsley G M (1979) Solid State Commun. 31,481

Graebner J E and Kunzler J E (1969) J.Low Temp.Phys. 1,443

Jansen H J F and Mueller F M (1979) Phys.Rev. B 20, 1426

Kessel A T van, Myron H W and Mueller F M (1978) Phys.Rev. Lett. 41,181

Klein B M, Boyer L L, Papaconstantopoulos D A and Mattheiss L F (1978) Phys.Rev. B 18,6411

Manuel A A, Samoilov S, Sachot R, Descouts P and Peter M (1979) Solid State Commun. 31,955

Pickett W E, Ho K M and Cohen M L (1979) Phys.Rev. B 19,1734

Sellmyer D J, Liekowitz D, Arko A J and Fisk Z (1980) private communication.

Fermi surface properties and effective masses

The previous chapter gives an introduction to A-15 Fermi surfaces. In a metal, the Fermi energy intersects the (three dimensional) band structure at $E_n(\vec{k}) = E_F$, producing a (two dimensional) surface in the momentum space. Empty states exist infinitesimally above E_F, so any microscopic probe produces mobile electrons, whose response can be measured by a variety of techniques. The Fermi surface, shown in fig. 4.3, is obtained from the *ab initio* Nb_3Sb energy bands through a linear interpolation on a fine mesh grid of $\vec{k}$ points on the high symmetry planes. As expected, three M centered and four R centered sheets are found. The labelling of the pieces is according to band number; the lowest valence band is the first band and correspondingly labelled 1. Nb_3Sb has 40 valence electrons per unit cell (5 electrons from each Nb and Sb site); the Fermi level thus falls between band 20 and 21, so the M centered sheets are holes and the R centered pieces are electron pockets. Nb_3Sb is a compensated material, so the total volume of the holes is equal to the total volume of the electron pockets. This constraint is of course fulfilled for our APW Fermi surface. The compensation constraint gives an alternative method to the determination of the Fermi energy.

To describe completely the Fermi surface of Nb_3Sb an interpolation scheme is required. In practice it is not feasible to evaluate the APW secular matrix every time. The generalized $\vec{k}.\vec{p}$ scheme, discussed in chapter IIb, can be applied here. However for the Nb_3Sb Fermi surface the limits imposed by the combining function are not present since all Fermi surface sheets are located in two disjoint $\vec{k}.\vec{p}$ fit domains (the holes in the M fit range and the electron pockets in the R fit range), so that one expansion domain may be used for each. Figure 4.4 shows the Fermi surface obtained from the $\vec{k}.\vec{p}$ fit of the Nb_3Sb APW bands. The similarity of the *ab initio* and fitted Fermi surface is clear, obvious showing that the (local) $\vec{k}.\vec{p}$ fits accurately represent the underlying APW band structure.

The $\vec{k}.\vec{p}$ fit of the bands near E_F which is used to derive the Fermi surface of Nb_3Sb, is used as a generator of the de Haas-van Alphen frequency spectrum and the effective band masses. Before discussing the calculated dHvA frequencies a brief discussion will be given of the

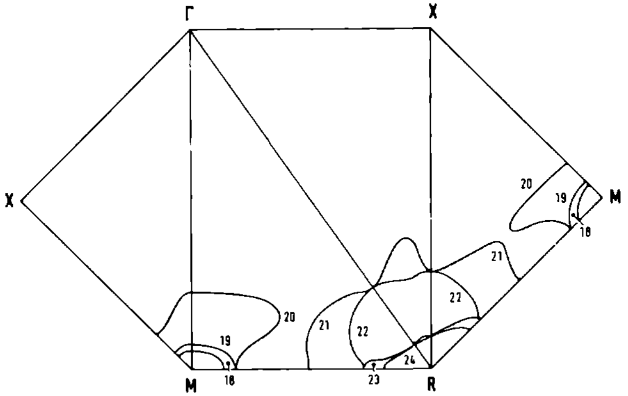

Figure 4.3 The direct from the APW bands derived Fermi surface of Nb_3Sb

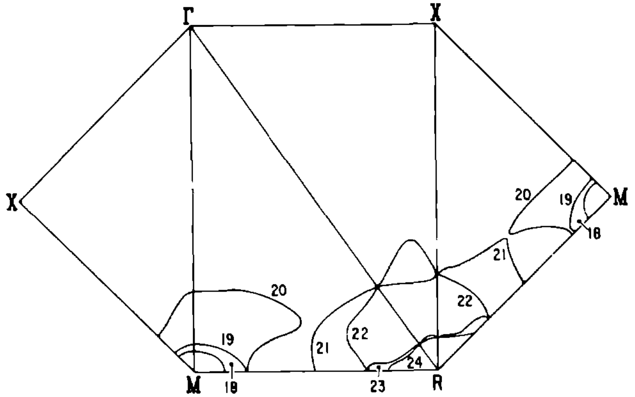

Figure 4.4 The $\vec{k}.\vec{p}$ *derived* Nb_3Sb *Fermi surface at the same Fermi energy as used in figure 4.3.*

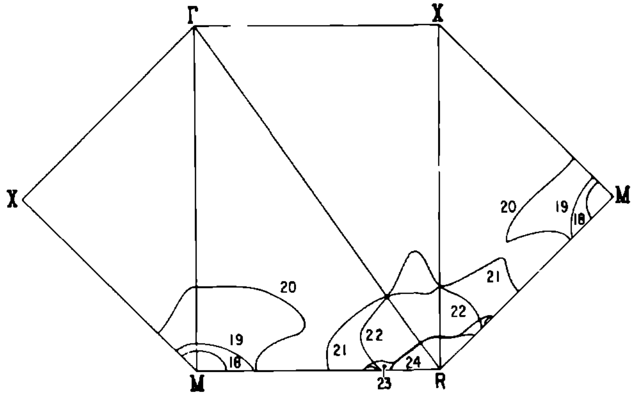

Figure 4.5 The optimized $\vec{k}.\vec{p}$ *derived Fermi surface of* Nb_3Sb.

dHvA effect itself.

The de Haas-van Alphen (dHvA) effect which was first discovered by de Haas and van Alphen in 1930 at Leiden, is the oscillatory component of the magnetic susceptibility ($\chi=\delta M/\delta H$) of a metal found at low temperature and in high magnetic field. The theory of the dHvA effect has been given by Lifshitz and Kosevich[7]. We give here the basic equations and the used formulas; interested readers may for example consult the review article by Sellmyer[8] or the book by Ashcroft[9]. In an uniform magnetic field ($\vec{H}$) the semiclassical equations of electron dynamics are

$$\vec{V}(\vec{k}) = \frac{1}{\hbar} \vec{\nabla} E(\vec{k}) \tag{1}$$

and

$$\hbar \frac{\delta \vec{k}}{\delta t} = -e \, \vec{V}(\vec{k}) \times \vec{H} \tag{2}$$

These equations show that in $\vec{k}$ space electrons move on trajectories which are the intersections of surfaces of constant energy and planes perpendicular to the magnetic field. These cross-sectional areas (A_n) are quantized in so called Landau levels, due to the Sommerfeld quantum condition

$$A_n = (n+\gamma) \; 2\pi \; e \; H/\hbar \tag{3}$$

where n is an integer and γ a phase constant. Since A_n increases with H, as the field is increased the various Landau levels will burst through the Fermi energy causing a fluctuation in the free energy of the system which causes equilibrium properties, such as the magnetisation, to oscillate as the field changes. It is easy to see from equation (3) that the oscillations are periodic in inverse field. Two successive Landau levels crossing an extremal area (A_e) of the Fermi surface have a period in field equal

$$\nabla = \left| \frac{1}{H_{n+1}} - \frac{1}{H_n} \right| = \frac{2 \pi e}{\hbar A_e} \tag{4}$$

This period results in the Onsager relation[10] for the dHvA frequency

$$F = \frac{\hbar}{2\pi e} A_e = 374.1 \quad A_e \qquad (5)$$

if F is given in megaGauss and A_e (area) is in atomic units. The cyclotron mass associated to the motion around this extremal cross-sectional area is defined by

$$m^* = \frac{1}{\pi} \frac{\delta A}{\delta E} \qquad (6)$$

if A is given in atomic units and E in Rydberg. The experimental cyclotron masses are derived from the amplitude of the oscillations. The dHvA frequencies (F) and the effective masses (m^*) can be calculated (equation (5) and (6)) from the geometry of the Fermi surface sheets. It is also possible to obtain Fermi surface radii from dHvA areas through the application of an inversion scheme[11].

Implicit in the above dHvA discussion has been the requirement that the electron relaxation time is slow compared to the period of the orbit ($\tau > \frac{1}{\omega_c}$ or $\tau\omega_c > 1$), so that the amplitude of the effect is not obliterated by scattering. Naturally, this implies that rather pure single crystals must be employed and for intermetallic compounds, residual resistance ratios (RRR) of at least 10 are required. However this requirement is rather arbitrary. Arko *et al.*[4] used a Nb_3Sb single crystal with a RRR equal to 90 or more. The oscillatory structure in 1/H will also be washed out if k_BT is greater than the typical energy separation between adjoining tubes of Landau levels. Arko *et al.*[4] measured the dHvA effect at 0.5^oK using the power of the modulation field technique in fields of 7 Tesla. Another requirement for the measurement of the dHvA effect is that the crystal is not in the superconducting state, since the Meissner effect expells the external magnetic field and causes complex smearing due to magnetic domains. So, the external field has to be higher than the upper critical field (H_{c_2}). For Nb_3Sn, discussed in chapter III, this requirement gives the need of fields in excess of 22 T. No such high fields are necessary for Nb_3Sb which T_c is equal to 0.2^oK.

After this short explanation of dHvA effect we now describe the calculation of the dHvA frequency spectrum. Figure 4.6 shows the dHvA

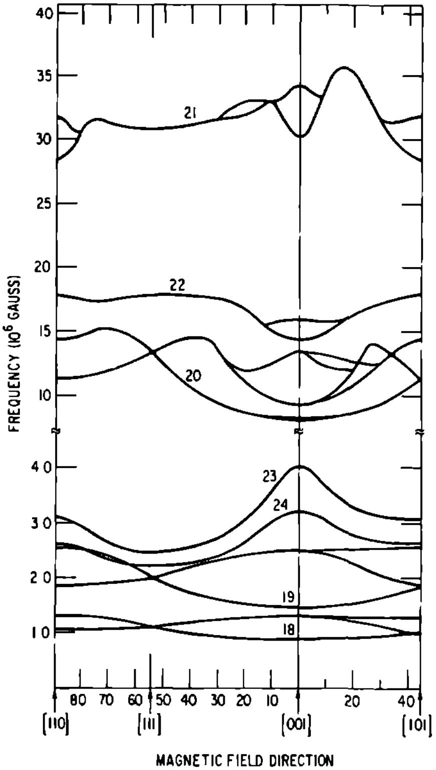

Figure 4.6 The calculated dHvA frequencies of Nb_3Sb derived from the Fermi surface shown in figure 4.4. The dHvA frequencies derived from figure 4.5 are shown in figure 3b page 89.

frequencies calculated from the $\vec{k}.\vec{p}$ fits around M and R. The Fermi energy is optimalized so that band 18 gives the best fit of the experimental[4] ellipse α . The experimental dHvA frequency spectrum can also be found in figure 3a of the reprint in this chapter. The difference between the Fermi level found from the integration of the density of states and the Fermi level which gives an optimal fit of the α frequencies is 3.0 mRy. This shift in E_F to higher energy reduces the band 18 Fermi surface and is comparable to the error intrinsic in our APW bands.

The small Fermi surface sheets, two M centered ellipsoids (18,19) and two R centered pieces (23,24) have only cross-sectional areas which are located in the planes through the high symmetry point, so called central orbits. In contrast, the curvature of the bigger orbits (20,21, 22) leads to non-central orbits. This can be seen from figure 4.4. For example, the central cross-sectional area of the biggest R centered orbit (21) in the [100] direction is smaller than the cross-sectional area parallel to this central orbit and cutting through the peaks in the ΓXR and XMR planes. This two orbits can be found in figure 4.6 in the [001] direction at 30 and 34 MGauss, respectively. The band 19 Fermi surface, the paprika like structure, leads to several non-central extremal cross-sectional areas. Arko *et al.*[4] suggested that their proposed γ Fermi surface yields a non-central orbit γ_1' in the [001] direction (see figure 3a on page 89).

The correspondence between the orbits found by Arko, Fisk and Mueller[4] from the dHvA effect and our calculated frequencies is clear. Some orbits are even in excellent quantitative agreement (band 18 and 24). Other orbits show qualitative agreement, but are shifted in frequency (bands 20,21 and 22). Two of our Fermi surface sheets were not found in the dHvA frequency spectrum measured in 1977[4] (bands 19 and 23).

Our predicted dHvA frequency spectrum stimulated Arko, Crabtree and Fisk[5] to remeasure the dHvA effect in Nb_3Sb. Their new data is at slightly higher field (7.5 T) and lower temperature (0.35°K) than that of their earlier measurements[4]. Aware of our calculated spectrum, it was easier for them to identify frequencies as belonging to a new orbit than as due to higher order harmonic from lower lying frequency.

They also reexamined previous data and found new features. The new analyses were only performed in the (110) plane. Figure 3a on page 89 contains the sum total of the dHvA frequency data obtained in Nb_3Sb.

Meanwhile, we shifted the individual Fermi surface sheets in such a way that they give all quantitative agreement to the experimental cross-sectional areas. Band 18 is unaffected, it was already optimized. Band 19 is shifted down by 0.5 mRy to give optimal fit to the first harmonic of the α frequencies, but is latter found to correspond to the new obtained ζ frequencies. Band 20 is also shifted down by 1.5 mRy, and it corresponds to fits the γ,χ and ε frequencies in figure 3a on page Band 21 is shifted down by 3.5 mRy, and corresponds to the δ frequencies. Band 22 is shifted down by 6.0 mRy, it fits the η frequencies and gives also understanding to some of the frequencies around 10 MGauss in the [001] direction. Bands 23 and 24 are not shifted, and can be found in the experimental dHvA frequencies as μ and β, respectively. Figure 3b on page 89 displays the calculated and optimalized dHvA frequency spectrum. Note that the correspondence is excellent over the entire angular range. The Fermi surface with the individual sheets shifted by the energies listed above is shown in figure 4.5. Except for some detailed differences, e.g. degenerations are lifted (by small spin orbit effects not included in our calculations) the overall curvature is not affected. The optimized theoretical dHvA spectrum also yields a compensated metal, that is to say the sum of the volume of the three M-centered holes is equal to the sum of the volume of the four R-centered electron pockets. The above listed shifts are relative to the Fermi energy obtained for an optimalized agreement between band 18 and the α frequencies. The shifts according to our initial Fermi level, derived from the density of states, are +3.0, +2.5, +1.5, -0.5, -3.0, + 3.0 and + 3.0 mRy for the bands 18 through 24, respectively. All shifts are within our estimated band error of 3.0 mRy.

From our Nb_3Sb band structure (figure 4.1), it is visible that a shift in E_F of the order of 10 mRy can give enormous changes in the Fermi surface structure. Knowing this, it is remarkable that our non self-consistent Nb_3Sb bands can produce such a high level agreement with high precision experiment such as the dHvA effect. The excellent agreement probably lies in the general form of potential included in our APW secular matrix and an optimal choice of the initial starting potential.

The Fermi surface of Nb_3Sb is also used to calculate the effective band masses along the high symmetry directions. Table 4.1 lists our cyclotron masses calculated, equation (6), at the individual optimal Fermi energies. The experimental effective masses listed in table 4.1 are taken from the references 4 and 12. The earlier published table with calculated cyclotron masses[13] was generated at one overall Fermi energy, the optimal band 18 to α fit, and can be used to deduce the sensitivity of the effective masses to energy changes. It follows that the sensitivity of band masses to energy shifts is larger than that of the areas. This behavior was expected, since a first order derivative is more difficult to fit than a zeroth order derivative, the function itself.

Table 4.1 also lists the calculated electron-phonon mass enhancements. They can be obtained from the quotient of experimental and calculated effective masses. This quotient is equal to one plus the enhancement factor. The enhancement factor is introduced because the phonons affect the electron-electron interaction and thus the electronic bands. The phononic influence happens in such a way that the bands become steeper at E_F and the derivative, the effective mass, becomes bigger. The electron-phonon enhancement factor can also be detected experimentally by specific heat on tunneling measurements. Knapp *et al.*[1] derived from specific heat data a λ for Nb_3Sb equal 0.3, which is about the same as our calculated averaged mass enhancement.

As established during the dHvA effect discussion, the free energy of a system shows an oscillatory behavior if the system is brought into an external magnetic field. This in turn causes fluctuations in equilibrium properties, such as the magnetisation (dHvA effect), temperature (magnetothermal oscillations) and conductivity (Shubnikov-de Haas (SdH) effect). Sellmyer *et al.*[6] measured the magnetoresistance and its oscillatory compound (SdH effect) for Nb_3Sb. They derived from their measurements several SdH frequencies. Most SdH frequencies fitted well into the dHvA spectrum of Arko *et al.*[5] Sellmyer *et al.* did found some frequencies of the $\alpha_{1,2}$ branch, the β orbit and the various γ branches. Figure 4 of reference 6 shows this correspondence. Inaddition, the SdH

TABLE 4.1 Effective masses and orbital λ's for Nb_3Sb

Band	Frequency[a)]	Orientation	m*(theory)	m*(exp)	λ
M centered orbits					
18 (z)	α_1	[001]	0.19		
18 (x,y)	$\alpha_{2,3}$	[001]	0.20		
18	α	[111]	0.21	0.26	0.24
18 (x,y)	$\alpha_{2,3}$	[110]	0.20		
18 (z)	α_1	[110]	0.20		
19 (z)	ζ_1	[001]	0.26		
19 (x,y)	ζ_2	[001]	0.48		
19		[111]	0.35		
19 (x,y)		[110]	0.32		
19 (z)		[110]	0.51		
20 (z)	γ_1	[001]	0.59	0.70	0.19
20 (x,y)	χ	[001]	0.98		
20 (x,y)	$\varepsilon_{1,2}$	[001]	0.88	1.34	0.52
20	γ	[111]	0.87	1.10	0.26
20 (x,y)	$\gamma_{2,3}$	[110]	0.70	0.89	0.27
20 (z)	γ_1	[110]	1.02	1.75	0.72
20 (z)	γ_1	A^b	0.67	0.60	-0.10
20 (y)	γ_3	A^b	1.07	1.5	0.4
20 (x)	γ_2	A^b	0.73	1.10	0.51
R centered orbits					
21	δ_1	[001]	1.92		
	δ_2	[001]	1.28		
	δ	[111]	1.40	1.58	0.13
	δ_1	[110]	1.47		
	δ_2	[110]	1.46		
	δ	A^b	1.54	1.7	0.1
22	η_1	[001]	0.98		
	γ'_1	[001]	1.02		
	η	[111]	1.31		
	η	[110]	1.60		
	η	B^c	1.08	1.1	0.0
23	μ	[001]	0.93		
	μ	[111]	0.37		
	μ	[110]	0.58		
24	β	[001]	0.60		
	β	[111]	0.42	0.52	0.24
	β	[110]	0.47	0.64	0.36

Notes: a) The labelling of the experimental frequencies from ref.5
b) Orientation A is 27.5° from [001] to [101]
c) Orientation B is 40.0° from [001] to [101]

frequency spectrum contains a new frequency, denoted in reference 6 as ω, apparently not observed in the dHvA work. This ω frequency is only observed near [001] and the upward curvature of the ω frequency as $\vec{H}$ moves away from [001] appears to be real ($F_\omega[001] \simeq 2.5$mG).

The field dependence of the magnetoresistance was investigated carefully in the vicinity of [001] since a large-amplitude SdH oscillation is present in that direction. The size of this oscillation is quite suggestive of a magnetic breakdown process in which an open orbit is being successively turned on and off as various Landau level sweep through a particular sheet of Fermi surface. Sellmyer *et al.*[6] observed a tendency for the magnetoresistance to saturate. This effect can correspond to a multiply-connected Fermi surface or a loss of compensation due to magnetic breakdown. In conclusion, the observed ω frequency can not be related to the upper branch of band 19, although they have the same frequency, but should be correlated to a breakdown orbit which gives rise to a multiple-connected Fermi surface. One can imagine magnetic breakdown between band 20 (hole) and band 21 (electron) shown in figure 4.7. This leads to an egg-shaped cyclotron orbits whose area corresponds to the ω frequency. Such a breakdown orbit would also increase in frequency as $\vec{H}$ is tipped away from [001], as observed. If this orbit breaks down, an open orbit results which is similar to the jungle-jim topology initially proposed by Arko *et al.* (see figure 3 of ref.4).

The corresponding measurements of dHvA and SdH were performed at 7.5 T and 21.5 T, respectively. The probability of breakdown increases for increasing field and the tunnelling probability from the hole (electron) orbit onto the electron (hole) orbit is given by

$$P = \exp\ (-H_0/H) \qquad (7)$$

where

$$H_0 = \frac{\pi(\Delta E)^2}{4\ \hbar\ e\ v_F^2} \qquad (8)$$

ΔE is the band gap between band 20 and 21, and v_F the Fermi velocity at the edges of the two bands where breakdown is expected. We calculated

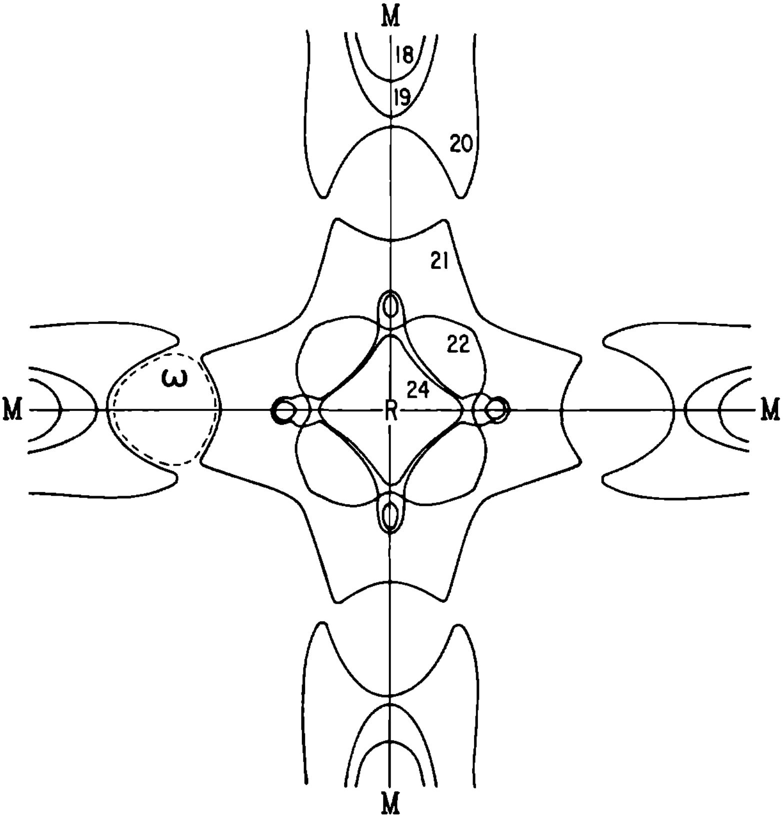

Figure 4.7 The optimized Nb_3Sb *Fermi surface in the* [001] *plane. Also shown is the possible breakdown orbit* ω.

that a field of 20 T has breakdown probability of the order of 40%, which explains why such effects are seen in the SdH experiments and not in dHvA effect. Of course dHvA at 21.5 T should also show breakdown and would be interesting.

In conclusion we should like to reiterate that we believe this research represents the first successful marriage of an *ab initio* calculation to the experimental Fermi surface of any A-15 compound on a scale of less than 1 mRy error.

References

1 G.S.Knapp,S.D.Bader and Z.Fisk,Phys.Rev.B13,3783 (1976)

2 F.Y.Fradin,G.S.Knapp,S.D.Bader,G.Cinader and C.W.Kimball in *Superconductivity in d- and f-Band Metals*,edited by D.H.Douglass (Plenum New York,1976)

3 J.Friedel,Advances in Physics 3,446 (1954)

4 A.J.Arko,Z.Fisk and F.M.Mueller,Phys.Rev.B16,1387 (1977)

5 A.J.Arko,G.W.Crabtree and Z.Fisk in *Superconductivity in d- and f-Band Metals*,edited by H.Suhl and M.B.Maple (Academic Press,New York 1980)

6 D.J.Sellmyer,D.Liebowitz,A.J.Arko and Z.Fisk,J.of Low Temp.Phys.40, 629 (1980)

7 I.M.Lifshitz and A.M.Kosevich,Sov.Phys.JETP 2,636 (1955)

8 D.J.Sellmyer in *Solid State Physics*,edited by H.Ehrenreich,F.Seitz and D.Turnbull (Academic Press,New York,1978)Vol.33

9 N.W.Ashcroft and N.M.Mermin,*Solid State Physics* (Holt,Rinehart and Winston,New York,1976)

10 L.Onsager,Phil.Mag.43,1006 (1952)

11 F.M.Mueller,Phys.Rev.148,636 (1966)

12 A.J.Arko,private communications

13 A.T.van Kessel,H.W.Myron,F.M.Mueller,A.J.Arko,G.Crabtree and Z.Fisk, in *Superconductivity in d- and f-Band Metals*,edited by H.Suhl and M.B.Maple (Academic Press,New York,1980)

14 M.Cohen and L.Falicov,Phys.Rev.Lett.7,231 (1961);E.I.Blount,Phys.Rev. 126,1636 (1962)

CHAPTER V : DISCUSSION

This chapter reviews the various electronic models which have been applied to understand the anomalous properties of the A-15 compounds. The results discussed in this thesis will be related to these electronic models and to A-15 band structures which have been calculated by other groups.

The first attempt to account quantitatively for the strong temperature dependence of the susceptibility, the Knight shift and the nuclear spin lattice relaxation rate of some A-15's was made by Clogston and Jaccarino[1]. They assumed a density of states in which the Fermi level falls at a narrow parabolic peak due to the A site *d* electrons. They found that such a narrow peak was able to explain the temperature dependence of the electronic properties of several A-15 compounds. The basic idea, a sharp peak in the density of states at or close to E_F, has been a consistent feature of all subsequent *ab initio* calculations of A-15 materials.

Later, Cohen *et al*[2]. proposed a step like density of states with E_F close to a step. Their model could also explain the electronic properties of most A-15 compounds. Since their density of states is essential different to the previous discussed model Cohen *et al.* concluded that a sharp variation of the density of states in the close vicinity of E_F is the main reason for the strong temperature dependence of the electronic properties of some A-15's. The exact form of this variation is of secondary importance only. This is in basic agreement with every *ab initio* A-15 band calculation.

The simplest band-like model for the A-15 materials is the linear chain model of Weger[3], Labbé and Friedel[4]. This model neglects all interchain interactions. Their argumentation was since the intrachain atomic distance is about 20% less than the interchain atomic distance intrachain effects would dominate. In the tight-binding approximation with nearest neighbors being considered, the chains become completely decoupled. The band structure has an appoximately one-dimensional character. The Fermi surface is composed of rectangular "boxlike" surfaces. Further simplifications were employed by Labbé and Friedel[4]. In addition, they neglect interband coupling and crystal field effects. Thus the *d* band is decomposed into five independent bands and the density of states show an $E^{-\frac{1}{2}}$ singularity at the band edges. Putting the Fermi level close to a band edge results in strong energy dependence of the density of states in the vicinity of the Fermi level, again giving rise to a strong temperature dependence of the electronic properties. The observed Martensitic transformation is in this model regarded as a Jahn-Teller effect. One family of chains contracts and two expand and electrons flow from the expanding to the contracting chains, causing a lowering of the total energy. The lowering can occur if E_F is close to a square root singularity in the density of states. One third of the peak is shifted to lower energy and two thirds to higher energy. The full three-dimensional structure (figure 2.4) shows little to resemble five disjoint simple cosine bands associated with the one-dimensional Labbé-Friedel model[8]. Nevertheless one feature of our results (and probably the most significant) is one-dimensional: the boxlike Fermi surface surrounding Γ in Nb_3Sn. That such a complicated material should show so simple a feature must be considered remarkable.

The magnitude of the second neighbor *d-d* interactions is similar in the A-15 structure and in the bcc crystal of A atoms[5]. The ratio of number of second neighbors to nearest neighbors is 4 in the A-15 structure, whereas this ratio is 0.75 in the bcc structure. The relative contribution of any shell of neighbors to the A atom *d* band width is approximately proportional to the product of the number of neighbors times the strength of the interaction. This suggests that second neighbor *d-d* interactions could easily be more important in the A-15 compounds than in the bcc metals. To correct the deficiencies in the linear chain model, Weger and Goldberg[6] have extended this model to include limited coupling between the chains. They applied the linear combination of atomic orbitals (LCAO) interpolation method[7] to fit the APW results of Mattheiss[8] on the high symmetry points. Their initial effort has been described as the independent band approximation (IBA). This IBA model includes both intrachain and interchain *d-d* interactions within a given *d* subband. However, it omits all hybridization interactions between the A atom subbands as well as many *p-d* interactions between the B atom *p* and the A atom *d* orbitals. As a result of these approximations, the IBA model produces extremely large peaks in the density of states, resulting from bands that are flat throughout the ΓXM plane of the Brillouin zone. Our A-15 energy bands also have in the ΓXM plane a flat character but only in the vicinity of the Γ point. The IBA model shows on a global scale similarities to the APW structure (fig. 10 of ref. 5).

Goldberg[9] has extended the IBA model to include interband hybridization and *p-d* interactions between the various *d* subbands in the A-15 structure. In principle, this coupled band approximation (CBA) is equivalent to the LCAO model of Mattheiss[5]. The main difference lies in the basis functions,the CBA involves orthogonalized atomic orbitals, whereas the LCAO model treats *s-d* and *p-d* overlap explicitly. The size of the fit parameters involved demonstrates that interband hybridization is substantial in the A-15 compounds, even at symmetry points in the Brillouin zone. Consequently, the two largest peaks in the IBA density of states disappear entirely in the CBA results. A problem for the CBA calculation is the low density of states at E_F for V_3Ga, since a large $N(E_F)$ should be obtained. We found in our density of states curves some huge peaks, up to 400 states/Ry-unit cell, which have their origin in the slowly varying energy bands near Γ. So we conclude that some states are less affected by the interband and interchain interactions. The form of the CBA model is in itself correct, however the parameters used by Goldberg and Weger were derived from the APW results of Mattheiss (at that time the only avialable *ab initio* calculations). These APW results utilized a bare muffin-tin crystal potential (see below) have according to our results an error of about 80 mRy at most. This deviation is larger than the root mean square error in the CBA fit to the Mattheiss bands (46 mRy). The CBA model is a scheme which has been fit to a low precision band calculation, thus the results obtained are in general unreliable.

The above discussed semiempirical models have been used to interpret the anomalous physical properties of the high T_c A-15 materials which involve fine structure in the density of states within a few mRy of the Fermi level. This degree of accuracy also should be obtained in an *ab initio* band calculation in order to be able to derive conclusions about the validity and limitations of various microscopic models that concentrate exclusively on such details in the density of states near E_F. None of the APW results discussed in the next paragraphs have an intrinsic error of less than a few mRy except our bands derived from a general form of potential.

The microscopic theory of the electronic structure was pioneered by Mattheiss[8], who carried out APW calculations on the A-15 compounds V_3X with X = Al, Si, Co, Ga, Ge and As. These non-self-consistent energy bands were obtained from a bare muffin-tin crystal potential and were only converged to 30 mRy. Except for V_3Ga these calculations were only performed on the four symmetry points and in addition, a rough density of states was constructed for V_3Ga. The main features of the simple electronic models can be found in Mattheiss results. The density of states is in qualitative agreement with the schematic model proposed by Clogston and Jaccarino[1]. The Fermi energy of V_3Ga coincides with a peak in the density of states which is primarily due to the A atom *d* bands. Perhaps the main conclusion is that there is no evidence for noticeable one-dimensional features in the electronic structure.

Subsequent calculations by Mattheiss[5] for V_3Si, V_3Ge, Nb_3Al and Nb_3Sn (all high T_c materials) has an order of magnitude better convergence. In these, the so called warping terms which correct for the non-constant behavior of the crystal potential in the interstitial region have been included. The application of the LCAO method to the APW results at the four high symmetry points was used as an interpolation scheme. The improved accuracy and the use of an interpolation method gave Mattheiss the possibility of constructing a Fermi surface. Figure 13 of ref.5 shows the Fermi surface of V_3Si and V_3Ge. As discussed before, the Fermi surface of V_3Si which is iso-electronic to Nb_3Sn, can be used as a first estimate of the Nb_3Sn Fermi surface. Mattheiss APW bands show the similarity between V_3Si and Nb_3Sn (fig.6 of ref.5), but only a few features of the V_3Si Fermi surface of Mattheiss can be found in our Nb_3Sn Fermi surface (fig.3 on page 57). Some M centered hole ellipsoids and an electron sea around X are common, but the boxlike sheets centered at Γ are not present in Mattheiss V_3Si

Fermi surface. Again Mattheiss did not find any evidence for a one dimensional character in the electronic structure of the system V_3Si / Nb_3Sn.

Self-consistent APW calculations were performed by Klein, Papaconstantopoulos, Boyer and Mattheiss[10-12]. Their obtained band structures are self-consistent, with warping terms for the interstitial potential corrections, with relativistic effects (neglecting spin-orbit coupling) and in addition during iterations a soft core approximation was used. For every iteration cycle the energy bands were calculated at only 10 points in 1/48th of the Brillouin zone, but the final bands were calculated at a finer mesh of 35 points. The potential inside the muffin-tins is approximated by a spherical average. Klein *et al.* ignored the deviations from the average which have there origin in the chain structure of the A atoms. Figures 2.2 and 2.3 show this potential behavior. The first A-15 compound calculated along these lines by Klein *et al.*[10] is V_3Si. The energy bands of V_3Si are even on a microscopic scale similar to our Nb_3Sn bands. As we found for Nb_3Sn, the Fermi level of V_3Si falls just on a huge peak (260 states / Ry-unit cell) primarily from the Γ_{12} state (Vanadium *d* like character). The next A-15 material calculated by Klein *et al.*[11] is V_3Ga. Again and true for the following calculations of ten A-15's by Klein *et al.*[12] their mesh in $\vec{k}$ space is too large to obtain a reliable Fermi surface. The $\pi/4a_0$ $\vec{k}$ mesh used makes a comparison with experimental Fermi surface data difficult and can not give detailed information about the band structure. Klein *et al.*[13] used their calculations for $\vec{k}$ space averaged properties such as density of states, plasma energy and other transport and superconductivity quantities. Mattheiss and Testardi[14] also calculated some transport quantities from Mattheiss APW bands and from the pseudopotential results (discussed below). The resulting quantities of Klein *et al.* and Mattheiss *et al.* are discussed above in chapter III.

Recently Klein *et al.*[15] applied the same self-consistent procedure to Nb_3Sb. The Nb_3Sb Fermi surface although not presented can be derived from their bands. This would consist of three R centered holes (also found by experiments, see chapter IV) and some M centered pieces. Muffin-tin corrections to the potential could change this Fermi surface (as we have found to be the case). However, the global structure R and

M centered Fermi surface sheets will remain. Their Nb_3Sn bands[12] could probably give a Fermi surface (also not presented) with high-mass Γ electron pockets and M and R centered holes. If a general potential inside the muffin-tin spheres had been considered, then shifts in the bands around M and R (see fig.2.5) would lead to significant variations in the Fermi surface. The Γ_{12} level will probably be unaffected by this addition. The band structures performed by Klein *et al.* are not reliable for determining Fermi surfaces but are useful for the calculation of space averaged quantities.

Jarlborg and Arbman[16,17] have done linear muffin-tin orbital(LMTO) band structure calculations for a large number of A-15 materials. Nb_3Sn and Nb_3Sb are among their set of compounds. Inherent to the LMTO method is the atomic sphere approximation (ASA). The ASA is a further simplification of the muffin-tin potential. The crystal potential is now represented as spherically symmetric in the overlapping Wigner-Seitz spheres. The overlapping Wigner-Seitz spheres, larger than the touching muffin-tin spheres, have the same total volume as that of the unit cell. This additional approximation to the crystal potential yields computational benefits. The LMTO method, in essence a tight-binding method is applied to this potential representation. The resulting band structures are equivalent to all other *ab initio* band structures. The obtained density of states curves for Nb_3Sn and Nb_3Sb[17] show the same structure as found in our curves. The LMTO density of states are 160 and 30 states /Ry-unit cell, respectively, comparable to our results. One should note that Jarlborg[17] calculated a charge transfer to the B side atoms of less than 0.15 electron per atom for both compounds. Jarlborg and Arbman did not calculate any $\vec{k}$ dependent electronic properties. An examination of their energy bands[16] gives the indication that the electronic properties are probably not comparable to experimental data. This lack mainly due to the potential approximations inherent to their methods.

The self-consistent pseudo-potential method has also been applied to the A-15 crystal structure. Using this method Pickett *et al.*[18] calculated the energy bands of the A-15 compounds Nb_3Ge and Nb_3Al and of the artificial A-15's Nb_3Nb and Nb_3* (chains only). The important simplification in the pseudo-potential method is the replacement of the nuclei and core electrons by an effective potential which gives the same valence electron solutions outside the core region. The behavior of the valence and conduction electrons is described porperly and from this the bonding and the charge distributions[18] can be evaluated. Pickett, Ho and Cohen[18,19] obtained for Nb_3Ge which is iso-electronic to Nb_3Sn a Fermi surface which consists of two M centered hole ellipsiods, some small R centered sheets, one Γ centered large surface ($r \approx 0.5\ \pi/a_0$) and an open surface from the Γ_{12} level. All the Fermi surface sheets of Nb_3Ge can more or less be related to experimental data and to our results. This is not surprising since Pickett *et al.*[18] also used a potential of completely general form. Pickett *et al.* find little evidence for rigid-band behavior in the $Nb_3Al_xGe_{1-x}$ system. This is relatable to our statement that $Nb_3Sn_xSb_{1-x}$ is also not ascribable by the rigid-band approximation. The charge distributions calculated from the pseudo-potential results show that no charge transfer occurs from the cubic sites to the Nb chains, and that there is some covalent like bonding between Nb chain atoms. Since a general form of potential is considered in the self-consistent pseudo-potential calculations, the resulting band structures and derived quantities are comparable to experimental data and to our APW bands also calculated from a general form of potential.

Now we have related our Nb_3Sn and Nb_3Sb results to experimental data (chapters III and IV) and to other A-15 band calculations (this chapter) we can make some final statements about the validity of our results. The principal source of error in any band calculation lies in the crystal potential. Hopefully, these errors would be minimized if the potential was calculated self-consistently, though, errors would persist because of the approximate treatment of exchange and correlation effect. Both types of errors occur in the present calculations which are not performed self-consistently. However, all the discussed band techniques contain these errors, even the self-consistent methods. Important is the way the band method uses the crystal potential. Is it transformed into a bare muffin-tin potential or even with the atomic sphere approximation? Is it treated as a corrected muffin-tin potential and are these corrections only considered in the interstitial region or also inside the muffin-tin spheres? The resulting effects of these corrections are of the order of 30 mRy which are for the small A-15 *d* band manifold significant. Our crystal potential is general and shows similarities to the V_3Si charge density distribution derived from x-ray data (Staudenmann *et al.*[20]). The crystal potential contour maps (figures 2.2 and 2.3) demonstrate the influence of the inside muffin-tin correction. The crystal potential has a chain structure along the Nb chains but the corresponding bare muffin-tin potential eliminates this potential chain. This difference can be found in the experimental confirmed boxlike Fermi surface sheets which are related to the presence of some one-dimensional character[3]. This general form of potential, also treated by Pickett *et al.*[18] is the origin for the excellent agreement of our results to a host of experimental data.

The charge transfer in A-15 compounds which is considered in self-consistent calculations[12,17,19] is of minor effect. Values less than two tenths of an electron are found. Considering the excellent agreement to experimental data, we conclude that self-consistency in A-15 energy band structures is less important than the use of the full crystal potential.

1 A.M.Clogston and V.Jaccarino, Phys.Rev. 121, 1357 (1961)

2 R.W.Cohen,G.D.Cody and J.J.Halloran, Phys.Rev.Lett.19, 840, (1967)

3 M.Weger, Rev.Mod.Phys.36, 175 (1964)

4 J.Labbé and J.Friedel, J.Phys. (Paris) 27, 153 and 303 (1966)

5 L.F.Mattheiss, Phys.Rev.B 12, 2161 (1975)

6 M.Weger and I.B.Goldberg in *Solid State Physics*, edited by H. Ehrenreich,F.Seitz and D.Turnbull (Academic Press,New York,1973) Vol.28

7 J.C.Slater and G.F.Koster, Phys.Rev.94, 1498 (1954)

8 L.F.Mattheiss, Phys.Rev.138, A112 (1965)

9 I.B.Goldberg, J.Phys.C 8, 1159 (1975)

10 B.M.Klein,D.A.Papaconstantopoulos and L.L.Boyer,Ferroelectrics 16, 299 (1977)

11 B.M.Klein,L.L.Boyer and D.A.Papaconstantopoulos, J.Phys.F 8, 617 (1978)

12 B.M.Klein,L.L.Boyer,D.A.Papaconstantopoulos and L.F.Mattheiss, Phys.Rev.B 18, 6411 (1978)

13 B.M.Klein,L.L.Boyer and D.A.Papaconstantopoulos, Phys.Rev.Lett.42, 530 (1979)

14 L.F.Mattheiss and L.R.Testardi, Phys.Rev.B 20, 2196 (1979)

15 B.M.Klein,D.A.Papaconstantopoulos and L.L.Boyer in *Superconductivity in d- and f-Band Metals*, edited by H.Suhl and M.B.Maple (Academic Press,New York,1980)

16 T.Jarlborg and G.Arbman, J.Phys.F 6, 189 (1976); 7, 1635 (1977)

17 T.Jarlborg, Ph.D.Thesis (Chalmers University of Technology, Göteborg,Sweden) *unpublished*

18 W.E.Pickett,K.M.Ho and M.L.Cohen, Phys.Rev.B 19, 1734 (1979)

19 K.M.Ho,W.E.Pickett and M.L.Cohen, Phys.Rev.B 19, 1751 (1979)

20 J.L.Staudenmann,P.Coppens and J.Muller, Solid state Comm.19,29(1976)

This Appendix focusses on the used method for constructing the four model Hamiltonians[7].

The space group symmetry of A-15 type materials is O_h^3 (Pm3n). O_h^3 distinguishes itselfs from O_h^1 by having the mixed space group operation $\{t_{\frac{1}{2}} \mid C_4[\bar{1}00]\}$ instead of the usual C_4 $[\bar{1}00]$. This group operation, also known as a glide plane, is a combination of the translation vector (a/2, a/2, a/2) and a rotation of $\pi/2$ about the $[\bar{1}00]$ axes. The same is true for the $[0\bar{1}0]$ and $[00\bar{1}]$ axes.

Independently Mattheiss[1] and Gorskowski[2] generated the O_h^3 irreducible representations and operandset. There is some inconsistency in their labeling[3]. We follow the notation of BSW[4]. The O_h^3 high symmetry point representations are named Γ, X, M and R; the necessary O_h^1 representations Γ,X and M.

Multiplying two O_h^3 irreducible reps gives a representation which can be reduced into O_h^1 irreducible reps. Even if we do not know the basis functions of the O_h^3 irreducible reps, we are able to construct the model Hamiltonians; their matrix elements are integrals of products of O_h^3 basis functions.

The matrices are constructed through the following steps:

- generating by computer all the matrices of the irreducible reps at the four $\vec{k}$ points, by using reference 2;
- determine the Hamiltonian dimensions by looking at the APW band structure;
- calculating Clebsch-Gordon coefficients, using the method of van den Broek[5];
- determine the phase factors of the Clebsch-Gordon coefficients;
- estimate the number of parameters involved, by generating low order independent basis functions for every O_h^1 irreducible reps.

Every appearance of an O_h^1 irreducible reps in the formed O_h^3 multiplication blocks is independent of their other appearances. So every O_h^1 irreducible reps has an attached adjustable parameter. For convenience we fixed the zeroth order ones; by this we already deleted 10 parameters in the M set.

The Hamiltonian should be Hermitian; this is also true for the four model Hamiltonians as well. This constraint gives one the capability of determining the Clebsch-Gordon phase factors. If only imaginary parameters appear in the highest order polynomial terms, deleting these terms will not raise the accuracy of the fit to a large extend, but will result in a real Hamiltonian with all the benefits of it. We finally obtain a real symmetric matrix in which diagonalisation proceeds faster. Examples are the deleted Γ_2 term in the $\Gamma_{12}\times\Gamma_{12}$ block and the deleted $\Gamma_{15'}$ in the $\Gamma_{25'}\times\Gamma_{25'}$ block. In the end we have to work with two real (Γ and M) and two complex (X and R) matrices.

TABLE A.1 Number of used symmetry independent parameters distributed on order for the high symmetry points

Order	Γ	X	M	R
total used	49	48	90	64
0	2	3	10	2
1	0	4	14	4
2	6	12	40	9
3	0	14	36	14
4	13	18		21
5	0			16 (only diagonal blocks)
6	12 ($\Gamma_{12}\times\Gamma_{12}$ $\Gamma_{12}\times\Gamma_{25'}$)			
8	8 ($\Gamma_{12}\times\Gamma_{12}$)			
10	10 ($\Gamma_{12}\times\Gamma_{12}$)			

Note: the zeroth order parameters are frozen for all high symmetry points to the APW energies

Table A.1 gives the list of the number of adjustable parameters as a function of order. The ratio between number of parameters and order grows on from Γ through X and R to M. There are two reasons for this, first the dimension of the Hamiltonian is equal to the number of bands fitted and second the local group symmetries of the high symmetry points are of different dimensions.

The Γ(0,0,0) model Hamiltonian

Table A.2 lists the matrix elements of the considered bands $\Gamma_{25'}$ and Γ_{12}. Table A.3 shows the used basis functions for the participating Γ representations. The imaginary polynomials are deleted from this model Hamiltonian (Γ_2, $\Gamma_{15'}$ in the diagonal blocks). This makes the matrix real symmetric. The polynomials of the different blocks go to different order: $\Gamma_{12}\times\Gamma_{12}$ tenth order, $\Gamma_{12}\times\Gamma_{25'}$ sixth order and $\Gamma_{25'}\times\Gamma_{25'}$ fourth order.

From the APW derived Fermi surface we find a flat piece perpendicular to the [100] directions (fig.2 of chapter III). For fitting this Fermi surface section one needs very high order polynomials in Γ, we went up to the tenth order in Γ_{12} block.

TABLE A.2 Product representation of Γ(0,0,0)

	Γ_{12}		$\Gamma_{25'}$		
Γ_{12}	$\Gamma_1 + \Gamma^2_{12}$				
	$\Gamma^1_{12}+i\Gamma_2$	$\Gamma_1-\Gamma^2_{12}$			
$\Gamma_{25'}$	$2\Gamma^3_{15'}$	$2\Gamma^1_{25'}$	$\Gamma_1 + 2\Gamma^2_{12}$		
	$\sqrt{3}\,\Gamma^2_{25'}-\Gamma^1_{15'}$	$-\Gamma^2_{25'}-\sqrt{3}\Gamma^1_{15'}$	$\Gamma^3_{25'}-i\Gamma^2_{15'}$	$\Gamma_1-\Gamma^2_{12}+\sqrt{3}\Gamma^1_{12}$	
	$-\sqrt{3}\,\Gamma^3_{25'}-\Gamma^2_{15'}$	$-\Gamma^3_{25'}+\sqrt{3}\Gamma^2_{15'}$	$\Gamma^2_{25'}+i\Gamma^1_{15'}$	$\Gamma^1_{25'}-i\Gamma^3_{15'}$	$\Gamma_1-\Gamma^2_{12}-\sqrt{3}\Gamma^1_{12}$

TABLE A.3 Used symmetry adapted polynomials at $\Gamma(0,0,0)$

Γ_1 : 1 ; R^2 ; R^4 ; $x^4+y^4+z^4$

Γ^1_{12} : $\sqrt{3}(x^2-y^2)$; $\sqrt{3}\,R^2(x^2-y^2)$; $\sqrt{3}(x^4-y^4)$

Γ^2_{12} : $(2z^2-x^2-y^2)$; $R^2(2z^2-x^2-y^2)$; $(2z^4-x^4-y^4)$

$\Gamma^1_{15'}$: $yz(y^2-z^2)$; $yzR^2(y^2-z^2)$; $yzx^2(y^2-z^2)$

$\Gamma^2_{15'}$ and $\Gamma^3_{15'}$ cyclic permutations of $\Gamma^1_{15'}$

$\Gamma^1_{25'}$: xy ; xyR^2 ; xyz^2 ; xyR^4 ; xyz^4, xyz^2R^2 ; $xy\,(x^4+y^4+z^4)$

$\Gamma^2_{25'}$ and $\Gamma^3_{25'}$ cyclic permutations of $\Gamma^1_{25'}$

Γ_1 (Γ_{12} diagonal block) : $i = 0,2,4,6,8,10$; $i+n \leq 10$

R^i ; $R^i(x^4+y^4+z^4)$; $R^i(x^2y^2z^2)$

$R^i(x^8+y^8+z^8)$

Γ_{12} (Γ_{12} diagonal block) : $i,j=2,4,6,8,10$; $i+j\leq 10$

Γ^1_{12} $\sqrt{3}(x^i-y^i)$; $R^j\sqrt{3}(x^i-y^i)$

Γ^2_{12} : $(2z^i-x^i-y^i)$; $R^j(2z^i-x^i-y^i)$

The $X(\pi/a,0,0)$ model Hamiltonian

Table A.4 lists the entire group multiplication of $X(O^3_h)$. The group of X consists of four doublets, labelled x_1,x_2,x_3 and x_4. The constructed Hamiltonian contains the levels x_1,x_2 and x_4. The final matrix is Hermitian; complex polynomials already appear in first order. Table A.5 shows the basis functions of $X(O^3_h)$ which are to be substituted in table A.4.

TABLE A.4 Product representations of $X(\pi/a,0,0)$

	x_1		x_2		x_3		x_4	
x_1	$X_1+X_{4'}$							
	$X_2-iX_{3'}$	$X_1-X_{4'}$						
x_2	$X_3+X_{2'}$	$X_4+iX_{1'}$	$X_1+X_{4'}$					
	$X_4-iX_{1'}$	$X_3-X_{2'}$	$X_2-iX_{3'}$	$X_1-X_{4'}$				
x_3	$C_5+C_{5'}$	$-C_5^*+C_{5'}^*$	$C_5^*+C_{5'}^*$	$C_5-C_{5'}$	$X_1+X_{1'}$			
	$C_5^*+C_{5'}^*$	$-C_5+C_{5'}$	$-C_5-C_{5'}$	$-C_5^*+C_{5'}^*$	$X_2-iX_{2'}$	$X_1-X_{1'}$		
x_4	$C_5^*+C_{5'}^*$	$C_5-C_{5'}$	$C_5+C_{5'}$	$-C_5^*+C_{5'}^*$	$X_3+X_{3'}$	$X_4+iX_{4'}$	$X_1+X_{1'}$	
	$-C_5-C_{5'}$	$-C_5^*+C_{5'}^*$	$C_5^*+C_{5'}^*$	$-C_5+C_{5'}$	$X_4-iX_{4'}$	$X_3-X_{3'}$	$X_2-iX_{2'}$	$X_1-X_{1'}$

Notes:
$C_5 = X_5^1+iX_5^2$
$C_5^* = X_5^1-iX_5^2$
$C_{5'} = X_{5'}^1+iX_{5'}^2$
$C_{5'}^* = X_{5'}^1-iX_{5'}^2$

TABLE A.5 Used $X(\pi/a,0,0)$ centered symmetry adapted polynomials

X_1 :	$1;x^2;y^2+z^2;x^4;y^2z^2$ $x^2(y^2+z^2);y^4+z^4$	$X_{1'}$:	-
X_2 :	$y^2-z^2;x(y^2-z^2);y^4-z^4$	$X_{2'}$:	xyz
X_3 :	yz	$X_{3'}$:	$x(y^2-z^2)$
X_4 :	-	$X_{4'}$:	$x;x^3;x\ (y^2+z^2)$
X_5^1 :	xy	$X_{5'}^1$:	$y;y^3;yx^2;yz^2$
X_5^2 :	xz	$X_{5'}^2$:	$z;z^3;zx^2;zy^2$

The M (π/a,π/a,0) model Hamiltonian

Table A.6 lists the entire group multiplication of $M(O_h^3)$. Most levels are used in the model Hamiltonian (see table 2.2). Table A.7 gives, as usual, the polynomials which are basisfunctions of $M(O_h^1)$ that should be substituted in the Hamiltonian.

The R (π/a,π/a,π/a) model Hamiltonian

Table A.8 represents the constructed R centered model Hamiltonian. This matrix is Hermitian, imaginary parts are present already to first order (Γ_{15}) and hence not deleted as for the case of Γ and M. Table A.9 gives a list of the polynomials needed in the effective Hamiltonian. Note that in the $R_4 \times R_4$ block the more dimensional representations of Γ appear two times each. These twin appearances are independent, except the $\Gamma_{25'}$ polynomials, they are dependent because of the Hermitian demands of the Hamiltonian[6,7].

TABLE A.7 Used symmetry adapted polynomials M(π/a,π/a,0) centered

M_1 :	$1;z^2;x^2+y^2$	$M_{1'}$:	-
M_2 :	x^2-y^2	$M_{2'}$:	xyz
M_3 :	xy	$M_{3'}$:	$z(x^2-y^2)$
M_4 :	-	$M_{4'}$:	$z;z^3;z(x^2+y^2)$
M_5^1 :	xz	$M_{5'}^1$:	$x;xz^2;x(x^2+y^2)$
M_5^2 :	yz	$M_{5'}^2$:	$y;yz^2;y(x^2+y^2)$

TABLE A.6 Product representations of M

	m_1	m_2	m_3	m_4	m_5	m_6	m_7	m_8	m_9		m_{10}	
m_1	M_1											
m_2	M_3	M_1										
m_3	M_4'	M_2'	M_1									
m_4	M_2	M_4	M_3	M_1								
m_5	M_2	M_4	M_3'	M_1'	M_1							
m_6	M_4	M_2	M_1'	M_3'	M_3	M_1						
m_7	M_3'	M_1'	M_2	M_4	M_4'	M_2'	M_1					
m_8	M_1'	M_3'	M_4	M_2	M_2'	M_4'	M_3	M_1				
m_9	$M_5^1{}'$	$M_5^2{}'$	M_5^1	M_5^2	$M_5^1{}'$	$M_5^2{}'$	M_5^1	M_5^3	M_1+M_2			
	$M_5^2{}'$	$M_5^1{}'$	M_5^2	M_5^1	$-M_5^2{}'$	$-M_5^1{}'$	$-M_5^2$	$-M_5^1$	M_3-iM_4	M_1+M_2		
m_{10}	M_5^1	M_5^2	$M_5^1{}'$	$M_5^2{}'$	M_5^1	M_5^2	$M_5^1{}'$	$M_5^2{}'$	$M_4'+M_3'$	$M_2'-iM_1'$	M_1+M_2	
	M_5^2	M_5^1	$M_5^2{}'$	$M_5^1{}'$	$-M_5^2$	$-M_5^1$	$-M_5^2{}'$	$-M_5^1{}'$	$M_2'+iM_1'$	$M_4'-M_3'$	M_3-iM_4	M_1-M_2

TABLE A.8 Product representations of R(π/a,π/a,π/a)

	R_1		R_2	
R_1	$\Gamma_1+\Gamma_2$			
	$f^*\Gamma^1_{12'}-if^*\Gamma^2_{12'}$	$\Gamma_1-\Gamma_2$		
R_2	$if^*\Gamma^1_{12}+f^*\Gamma^2_{12}$	$\Gamma_{1'}-\Gamma_{2'}$	$\Gamma_1+\Gamma_2$	
	$\Gamma_{1'}+\Gamma_{2'}$	$if\Gamma^1_{12}+f\Gamma^2_{12}$	$f\Gamma^1_{12}-if\Gamma^2_{12'}$	$\Gamma_1-\Gamma_2$
R_4	$\Gamma^1_{15}+\Gamma^2_{25}$	$\Gamma^1_{15'}-\Gamma^2_{25'}$	$\Gamma^1_{15}+\Gamma^2_{25}$	$\Gamma^1_{15'}-\Gamma^2_{25'}$
	$\Gamma^1_{15'}+\Gamma^2_{25'}$	$\Gamma^1_{15}-\Gamma^2_{25}$	$\Gamma^1_{15'}+\Gamma^2_{25'}$	$\Gamma^1_{15}-\Gamma^2_{25}$
	$f^*\Gamma^2_{15}+f^*\Gamma^3_{25}$	$f\Gamma^2_{15'}-f\Gamma^3_{25'}$	$f\Gamma^2_{15}+f\Gamma^3_{25}$	$f^*\Gamma^2_{15'}-f^*\Gamma^3_{25'}$
	$f^*\Gamma^2_{15'}+f^*\Gamma^3_{25'}$	$f\Gamma^2_{15}-f\Gamma^3_{25}$	$f\Gamma^2_{15'}+f\Gamma^3_{25'}$	$f^*\Gamma^2_{15}-f^*\Gamma^3_{25}$
	$f\Gamma^3_{15}+f\Gamma^1_{25}$	$f^*\Gamma^3_{15'}-f^*\Gamma^1_{25'}$	$f^*\Gamma^3_{15}+f^*\Gamma^1_{25}$	$f\Gamma^3_{15'}-f\Gamma^1_{25'}$
	$f\Gamma^3_{15'}+f\Gamma^1_{25'}$	$f^*\Gamma^3_{15}-f^*\Gamma^1_{25}$	$f^*\Gamma^3_{15'}+f^*\Gamma^1_{25'}$	$f\Gamma^3_{15}-f\Gamma^1_{25}$

$\boxed{R_4 \times R_4}$

$\Gamma_1+\Gamma^1_{12}+a\Gamma^2_{12}$					
$i\Gamma_{2'}$	$\Gamma_1-C^1_{12}-aC^4_{12}$				
$\Gamma^3_{15'}+\Gamma^1_{25'}$	$ib\Gamma^3_{15}+c\Gamma^1_{25}$	$\Gamma_1-C^2_{12}+aC^3_{12}$			
$i\Gamma^3_{15}+\Gamma^1_{25}$	$-\Gamma^3_{15'}+\Gamma^1_{25'}$	$i\Gamma_{2'}$	$\Gamma_1-\Gamma^1_{12}+a\Gamma^2_{12}$		
$\Gamma^2_{15'}+\Gamma^3_{25'}$	$-i\Gamma^2_{15}+\Gamma^3_{25}$	$\Gamma^1_{15'}+\Gamma^2_{25'}$	$ib\Gamma^1_{15}+c\Gamma^2_{25}$	$\Gamma_1-C^1_{12}-aC^4_{12}$	
$ib\Gamma^2_{15}+c\Gamma^3_{25}$	$-\Gamma^2_{15'}+\Gamma^3_{25'}$	$i\Gamma^1_{15}+\Gamma^2_{25}$	$-\Gamma^1_{15'}+\Gamma^2_{25'}$	$i\Gamma_{2'}$	$\Gamma_1+C^2_{12}+aC^3_{12}$

Notes: $f = -\tfrac{1}{2} - \tfrac{1}{2}i\sqrt{3}$

$C^1_{12} = \tfrac{1}{2}\,\Gamma^1_{12} - \tfrac{1}{2}\sqrt{3}\Gamma^2_{12}$

$C^2_{12} = \tfrac{1}{2}\,\Gamma^1_{12} + \tfrac{1}{2}\sqrt{3}\Gamma^2_{12}$

$C^3_{12} = \tfrac{1}{2}\sqrt{3}\Gamma^1_{12} - \tfrac{1}{2}\,\Gamma^2_{12}$

$C^4_{12} = \tfrac{1}{2}\sqrt{3}\Gamma^1_{12} + \tfrac{1}{2}\,\Gamma^2_{12}$

a, b and c are independent variables

The reduces Γ representations are shown up to fourth order.

TABLE A.9 Used $R(\pi/a,\pi/a,\pi/a)$ centered symmetry adapted polynomials

$\Gamma_1: 1; R^2, R^4, x^4+y^4+z^4$	$\Gamma_1':-$
$\Gamma_2:-$	$\Gamma_2': xyz, R^2xyz$
$\Gamma^1_{12}: \sqrt{3}(x^2-y^2); \sqrt{3}(x^4-y^4); \sqrt{3}R^2(x^2-y^2)$	$\Gamma^1_{12'}: xyz\sqrt{3}(x^2-y^2)$
$\Gamma^2_{12}: 2z^2-x^2-y^2; 2z^4-x^4-y^4; R^2(2z^2-x^2-y^2)$	$\Gamma^2_{12'}: xyz(2z^2-x^2-y^2)$
$\Gamma^1_{15}: x; x^3; xR^2; x^5;\ xR^4; x^3R^2; x(x^4+y^4+z^4)$	$\Gamma^1_{15'}: xy(x^2-y^2)$
$\Gamma^1_{25}: z(x^2-y^2); zR^2(x^2-y^2); z^3(x^2-y^2)$	$\Gamma^1_{25'}: xy; xyz^2; xyR^2$

Note: The other basis functions can be obtained by cyclic permutations

References

1 L.F.Mattheiss,Solid State and Molecular Theory Group,M.I.T., Quaterly Progress Report No.51,p.54,1964 (unpublished)

2 W.Gorzkowski,Phys.Stat.Sol.3,910 (1963)

3 L.F.Mattheiss,Phys.Rev.138,A112 (1965)

4 L.P.Bouckaert,R.Smoluchowski,E.Wigner,Phys.Rev.50,58 (1936)

5 P.M.van den Broek,Phys.Stat.Sol(b) 90,211 (1978)

6 T-K.Lee,J.L.Birman,S.J.Williamson,Phys.Rev.Lett.39,839 (1977)

7 A.T.van Kessel,H.W.Myron,F.M.Mueller,BSB Internal Report (unpublished). Copies of our FORTRAN codes and parameterlist are available on request

APPENDIX B : TIMING AND THE AP120B ARRAY PROCESSOR

Timing

The running APW code is a CPU-time consuming program. A basis of 300 APW functions is needed to get a convergence of eigenvalues to 2 mRy. This APW matrix of rank 300 has to be diagonalized in order to obtain the resulting lowest eigenvalues. The application of Löwdin perturbation to this matrix is inapplicable because the non-diagonal elements are not small enough compared to the diagonal elements. This is due to the fact that the energy bands are close to each other, so their mutual interaction is large. Thus the full matrix has to be diagonalized. This is done by the EISPACK routines TRED3 and TQL1. The first reduces the matrix to a tridiagonal matrix; the second routine calculates the eigenvalues from the tridiagonal matrix. TRED3 consumes the most CPU-time (see table B.1).

TABLE B.1 Execution time (in seconds) of the three main steps in an APW run on different computers

dimension	step	CY73	CY176	CY750	IBM370	VAX-11	AP120B
99	setup			2.5	9	11.7	
	TRED3			1.5	5.5	9.8	4
	TQL1			0.1	1.5	1.8	
249	setup			13	43	102	
	TRED3			21	84	182	60
	TQL1			1	5	11	
305	setup	126	41	18	63	183	
	TRED3	310	85	38	152		
	TQL1	14	5	2	6		
speed ratio's		1	3	7	2	1.5	3 (20)

The first three computers listed in table B.1 are CDC's with a 60 bit word length and have a round off. The CYBER73 and 176 have been recently taken out of operation. On the IBM 370/158 computer the APW code runs in single precision. Since the 370 computer series work with hexadecimal numbers, as well as all IBM equipment and do not round off, the APW eigenvalues determined from these different computers differ in the third digit for a matrix of 300x300. The VAX-11/780 computer in contrast to the other computers is a midi. On the VAX the APW program runs in single precision but numbers are rounded. There resulting eigenvalues are equal to the first 7 digits of the CDC results. The APW program is adapted to the VAX because the AP120B array processor is attached to this machine.

AP120B array processor

The term array processor (AP) is not immediately clear, because there exist two types of AP's. The first type is a pipelined. This type is called an AP because it is designed for array processing. To this type belongs the AP120B, produced by Floating Point Systems. The second type is the matrix AP. This type is built of an one- or two-dimensional array of processor units. Nowadays there exists matrix AP's of size up to 128x128.

The schematics of the pipelined AP AP120B is shown in figure B.1. The floating point adder is a two stage adder and the multiplier a three stage multiplier, both with rounding. An example: one wants to calculate the dot product of a N-dimensional vector of single precision real numbers (28 bit mantissa). Then at a rate of one machine cycle equal to 167 nsec.each of the vector components are included in the final dot product. This rate is achieved by the pipelined structure of the arithmetic units and the independence of the different system buses.

The work done on the AP120B implements the EISPACK routine TRED3. The FPS mathematical library already contains a TRED routine but at that time there were some program errors in the object code of the library. The FORTRAN source code was compiled with the AP FORTRAN cross-compiler. The object code produced by this compiler was far from optimal: bad use of the bus independency (no loop folding) and all variables, even the

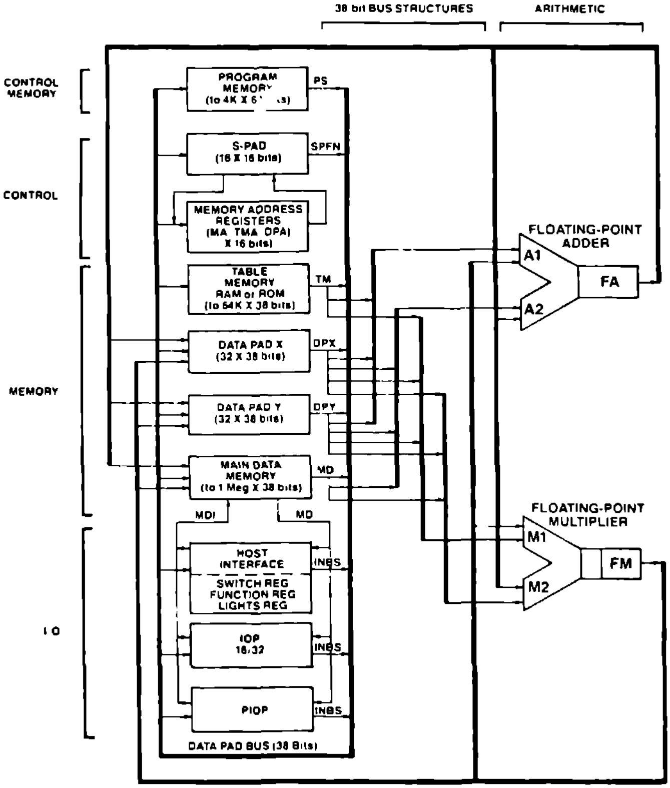

Figure B.1: AP120B arithmetic paths

loop variables, were stored in the main data memory. The execution times obtained from this non-optimal TRED3 routine are listed in the last column of table B.1. The 305 dimension could not be performed because of 16 bits integer limitations. To do a 305 run one needs to cut the matrix in different array's.

By comparing the APASSEMBLER listing of the TRED2 routine from the library and the object listing of TRED3 produced by the APFORTRAN compiler we deduced a factor 7 in the execution times between the two programs. Thus under the speed ratio's in table B.1 a factor 20 is listed.

In conclusion the AP 120B will be a factor 3 fasther in diagonalisation than the luxurious and substantially more expensive CYBER750 from CDC.

Acknowledgement

I wish to thank Prof.Dr.C.H.A.Koster for giving me access to the VAX-11/AP120B system of the Informatica group. I thank Maik Stahl for helpful discussions during the program development on the VAX machine.

References

EISPACK : B.S.Garbow and J.J.Dongarra,EISPACK Library,ARGONNE NATIONAL LABORATORY (1974);

AP120B : Floating Point Systems, AP120B Programmer reference manual; A.T.van Kessel,BSB internal report on the AP120B experiences (unpublished).

SUMMARY

In this thesis we have described a theoretical investigation on the electronic structure of the two A-15 compounds Nb_3Sn and Nb_3Sb. The interpenetrating linear chains of A atoms represent the single most important and significant feature of the A-15 crystal structure. For the calculation of the energy bands the Augmented Plane Wave (APW) method was extended and adapted to the A-15 structure. In general the APW method utilizes the muffin-tin approximation to the full crystal potential: a completely spherically symmetric potential within spheres of the largest possible radius centered on the nuclei and a constant potential in the interstitial region. Because of the closeness of the Nb atoms along a chain, the muffin-tin approximation would be poor for any A-15 material. Two additional corrections to the muffin-tin form of the potential were systematically included in the APW secular matrix elements in this work.

Our non self-consistent band structures were used, first fitted to the generalized $\vec{k}.\vec{p}$ matrices, to calculate density of states, Fermi surface and superconductivity parameters.

The results obtained for Nb_3Sn, a superconductor with a high critical temperature (T_c=18°K), lead to the following picture. The calculated density of states which shows similarities to the measured XPS spectrum has a large density of states at the Fermi level and shows a steep drop just above the Fermi energy. The high density of states at E_F is common among other A-15 compounds with a high T_c. This characteristic, valid for all transition metals and transition metal compounds, can according to BCS theory lead to high T_c's. The anomalous temperature dependence of the magnetic susceptibility can directly be related to the rapid drop of the density of states at E_F. The validity of the calculated Fermi surface can be deduced from several experiments, namely, the de Haas-van Alphen effect and positron annihilation. Results from the dHvA effect fit the calculated frequency spectrum of the M centered ellipsoids. Positron annihilation data represents reasonably well the Γ centered boxlike Fermi surface sheets. The calculations of the average Fermi

velocity and of other transport quantities show that even the mean derivative of the energy bands gives good agreement with experimental values. The averaged Fermi velocity forms the basis for the theory of the upper critical field anisotropy of a superconductor. The obtained anisotropy parameters can be compared to global experimental results. The *ab initio* Nb_3Sn energy bands show that linear character is present in the electronic structure.

In contrast to Nb_3Sn, Nb_3Sb is not a high T_c superconductor. Although these two A-15 compounds differ by only one valence electron per B side atom, Nb_3Sb does not show the anomalous properties of Nb_3Sn. The density of states of Nb_3Sb on a global scale is equivalent to that of Nb_3Sn, except now the Fermi level falls above the niobium *d* band manifold resulting in a small density of states at E_F. Hence, high-massed boxlike Fermi surface sheets have disappeared in Nb_3Sb. The M centered hole ellipsoids and R centered electron pockets form the basis for which the de Haas-van Alphen and the Shubnikov-de Haas measurements were completely explained. The previously unobserved magnetic breakdown orbit can be derived from our Fermi surface.

In their papers both Mattheiss[1] and Weger[2] have stressed the importance and difficulty of high precision A-15 band structures. Based on the excellent agreement we have found with a host of experimental data, we believe that the results presented in this thesis can be reliably applied as a basis to understanding the interesting and anomalous properties of A-15 materials.

---

[1] L.F. Mattheiss, Phys.Rev.B 12, 2161 (1975)

[2] M. Weger and I.B. Goldberg in *Solid State Physics*, edited by H. Ehrenreich, F. Seitz and D. Turnbull (Academic Press, New York, 1973) Vol.28

SAMENVATTING

In dit proefschrift wordt een theoretisch onderzoek naar de elektronenstruktuur van de A-15 verbindingen Nb_3Sn en Nb_3Sb beschreven. Inherent aan de A-15 kristalstruktuur zijn de lineaire ketens van de A atomen, in genoemde verbindingen niobium. Om inzicht te krijgen in het gedrag van de elektronen in deze verbindingen is de Augmented Plane Wave (APW) methode uitgebreid en aangepast aan de A-15 struktuur. De standaard APW methode past de muffin-tin benadering toe op de kristalpotentiaal: een geheel sferisch symmetrische potentiaal in liefst maximale bollen rond de atoomposities en een konstante potentiaal in de tussenruimten. De aanwezigheid van de A atoom ketens in A-15 verbindingen maakt opheffing van de muffin-tin benadering noodzakelijk. Hiertoe worden in onze berekeningen systematisch twee extra termen aan de APW-matrixelementen toegevoegd.

De aldus verkregen niet zelf-consistente bandenstrukturen zijn gebruikt, via de toepassing van een gegeneraliseerde $\vec{k}.\vec{p}$ interpolatiemethode, om toestandsdichtheden, Fermi oppervlakken en supergeleidingsparameters te berekenen.

Voor Nb_3Sn, een supergeleider met een hoge kritische temperatuur ($T_c=18^oK$), is het navolgende beeld verkregen. De berekende toestandsdichtheid vertoont overeenkomst met het gemeten XPS-spectrum. Karakteristiek zijn de grote waarde aan het Fermi nivo en een groot verval iets boven het Fermi nivo. De grote toestandsdichtheid voor de Fermi energie is kenmerkend voor de A-15 verbindingen met een hoge T_c. Deze eigenschap geldt voor alle overgangsmetalen en overgangsmetaal verbindingen en kan juist volgens de BCS-theorie een hoge T_c opleveren. De gemeten grote temperatuurafhankelijkheid van de magnetische susceptibiliteit staat in verband met het grote verval in de toestandsdichtheid aan het Fermi nivo. De nauwkeurigheid van het berekende Fermi oppervlak kan worden bepaald uit een vergelijk met positron annihilatie meetresultaten en met metingen van het de Haas-van Alphen effect. De positron annihilatie resultaten geven de doosachtige Γ-gecentreerde delen van het Fermi oppervlak weer.

De resultaten van het dHvA effect komen overeen met het berekende frequentiespectrum van de M-gecentreerde ellipsen. De berekening van de gemiddelde snelheid aan het Fermi oppervlak en van andere transportgrootheden laat zien dat zelfs de gemiddelde afgeleide van de energiebanden goede overeenkomst vertoont met de gemeten waarde. De gemiddelde Fermi snelheid vormt de basis voor de berekening van de anisotropie in het tweede kritische magneetveld van een supergeleider. De verkregen anisotropieparameters zijn te vergelijken met experimentele resultaten. Helaas zijn slechts globale metingen bekend. De *ab initio* berekening van de Nb_3Sn energiebanden laat zien dat er stellig lineair karakter in de elektronenstruktuur aanwezig is.

Nb_3Sb heeft in tegenstelling tot Nb_3Sn geen hoge T_c en mist ook de andere fascinerende fysische eigenschappen van Nb_3Sn. Toch is het verschil tussen Nb_3Sn en Nb_3Sb slechts één valentie elektron per B atoom. De toestandsdichtheid van Nb_3Sb is globaal gelijk aan die van Nb_3Sn, maar het Fermi nivo valt nu iets boven de niobium sub-*d*-band. Daardoor is de toestandsdichtheid aan het Fermi nivo klein. Het Fermi oppervlak mist nu de doosachtige strukturen, maar de M-gecentreerde ellipsen zijn gebleven. Samen met de R-gecentreerde elektron delen vormen ze het uitgangspunt om de de Haas-van Alphen en de Shubnikov-de Haas metingen te verklaren. Zelfs de onlangs waargenomen magnetische breakdown kan worden afgeleid uit ons Fermi oppervlak.

Mattheiss[1] en Weger[2] hebben beiden in hun publicaties het belang en de moeilijkheid van nauwkeurige A-15 bandenstrukturen benadrukt. Uitgaand van de voortreffelijke overeenkomsten met een veelvoud van experimentele gegevens, geloven we dat de in dit proefschrift beschreven resultaten als uitgangspunt kunnen worden gebruikt om de interessante en onregelmatige eigenschappen van de A-15 verbindingen te doorgronden.

---

[1] L.F. Mattheiss, Phys.Rev.B 12, 2161 (1975)

[2] M. Weger and I.B. Goldberg in *Solid State Physics*, edited by H. Ehrenreich, F. Seitz and D. Turnbull (Academic Press, New York, 1973) Vol.28

CURRICULUM VITAE

van Augustinus Thomas van Kessel
geboren op 22 september 1952 te Amsterdam

september 1965 - juni 1970 - HBS-b, Puis X College, Beverwijk

september 1970 - augustus 1976 - Subfakulteit Scheikunde van de Vrije Universiteit, Amsterdam

. april 1973 Kandidaatsexamen Scheikunde 3, cum laude

. oktober 1974 De Unilever Chemieprijs voor de VU toegekend gekregen

. augustus 1976 Doctoraalexamen
Hoofdvak : Theoretische Chemie
Bijvakken : Fysische Chemie
Electronica

september 1976 - april 1981 - Fakulteit der Wiskunde en Natuurwetenschappen van de Katholieke Universiteit Nijmegen. Werkzaam op de afdeling Banden Struktuur Berekeningen in ZWO/FOM-dienstverband.

STELLINGEN

I

Door alleen een R_4 bijdrage tot het Fermi oppervlak aan te nemen en door geheel het fenomeen van hybridisatie te verwaarlozen, zullen Lee *et al.* nooit een geloofwaardige elektronische beschrijving van de A-15 verbindingen kunnen geven.

T-K.Lee,J.L.Birman and S.J.Williamson,Phys.Rev.Lett.39,839(1977)

II

Artikel 23 van de promotieregeling der Stichting Katholieke Universiteit Nijmegen dient te worden geschrapt, daar promovendi dit Artikel weten te omzeilen.

Proefschrift M.den Nijs, dit proefschrift

III

De veronderstelling dat er een relatie bestaat tussen de geïnvesteerde uren computertijd en de kwaliteit van de resultaten is fout.

IV

De Nobelprijs wordt steeds minder aan Nederlanders toegekend, omdat wij de moed niet hebben om origineel te willen zijn.

V

Door zowel de vergaande miniturisering van grote rekentuigen als de capaciteitvergrotingen van één-chip systemen, dienen termen als micro-macro en macro-micro te worden ingevoerd (hierbij zijn gradaties als mini en midi nog buiten beschouwing gelaten).

VI

Een personeelsadvertentie voor politiemannen en -vrouwen, die alleen van mannen een minimale lichaamslengte vereist, is rijp voor behandeling door een staatsecretaris van evrouwcipatie zaken.

Microgids KRO

VII

De gehele gang van zaken rond de Ringspoorbaan en het Amsterdamse gedeelte van de Schiphollijn in ogenschouw genomen, kan men beter spreken van de Schipbreuklijn.

VIII

Het getuigt van weinig verkeersinzicht om een waarschuwingsbord "gevaarlijke bocht naar rechts" te plaatsen voor een bocht naar links.

Ravensteinseweg Wijchen

IX

Het klakkeloos gehoorgeven aan de oproepen van de Bloedtransfusiedienst maakt het geven van bloed bloedlink.

X

Mensen zijn als rook, waar ze komen betrekt de lucht.

Uit de lucht opgepikt

9 april 1981 Guus van Kessel